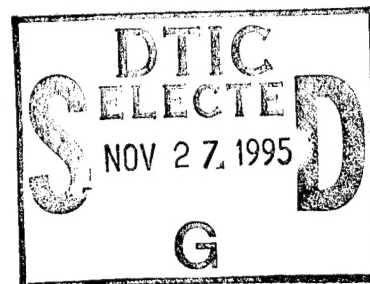PL-TR-95-2095

MODELING AND POST MISSION DATA ANALYSIS

V. A. Davis
B. M. Gardner

Maxwell Laboratories, Inc.
S-Cubed Division
P. O. Box 1620
La Jolla, California 92038-1620

DTIC
ELECTE
NOV 2 7 1995
G

29 June 1995

Scientific Report No. 2

19951120 091

DTIC QUALITY INSPECTED 8

This technical report has been reviewed and is approved for publication.

DONALD A. GUIDICE
Contract Manager

DAVID A. HARDY
Branch Chief

RITA C. SAGALYN
Division Director

This report has been reviewed by the ESC Public Affairs Office (PA) and is releasable to the National Technical Information Service (NTIS).

Qualified requestors may obtain additional copies from the Defense Technical Information Center (DTIC). All others should apply to the National Technical Information Service (NTIS).

If you address has changed, or if you wish to be removed from the mailing list, or if the addressee is no longer employed by your organization, please notify PL/IM, 29 Randolph Road, Hanscom AFB, MA 01731-3010. This will assist us in maintaining a current mailing list.

Do not return copies of this report unless contractual obligations or notices on a specific document requires that it be returned.

REPORT DOCUMENTATION PAGE

Public reporting burden for this collection of information is estimated to average 1 hour per response, including the time for reviewing instructions, searching existing data sources, gathering and maintaining the data needed, and completing and reviewing the collection of information. Send comments regarding this burden estimate or any other aspect of this collection of information, including suggestions for reducing this burden to Washington Headquarters Services, Directorate for Information Operations and Reports, 1215 Jefferson Davis Highway, Suite 1204, Arlington, VA 22202-4302, and to the Office of Management and Budget, Paperwork Reduction Project (0704-0188), Washington, DC 20503

1. AGENCY USE ONLY (Leave blank)	2. REPORT DATE 29 JUN 1995	3. REPORT TYPE AND DATES COVERED Scientific #2

4. TITLE AND SUBTITLE

Modeling and Post Mission Data Analysis

5. FUNDING NUMBERS

PE 63410F
PR 2822 TA GO WU SC

Contract F19628-93-C-0050

6. AUTHOR(S)

V. A. Davis
B. M. Gardner

7. PERFORMING ORGANIZATION NAME(S) AND ADDRESS(ES)

Maxwell Laboratories, Inc.
S-Cubed Division
PO Box 1620
La Jolla, CA 92038-1620

8. PERFORMING ORGANIZATION REPORT NUMBER

9. SPONSORING / MONITORING AGENCY NAME(S) AND ADDRESS(ES)

Phillips Laboratory
29 Randolph Road
Hanscom AFB, MA 01731-3010

Contract Manager: Donald Guidice/GPSG

10. SPONSORING / MONITORING AGENCY REPORT NUMBER

PL-TR-95-2095

11. SUPPLEMENTARY NOTES

12a. DISTRIBUTION / AVAILABILITY STATEMENT

Approved for public release; distribution unlimited

12b. DISTRIBUTION CODE

13. ABSTRACT (Maximum 200 words)

This report describes work performed during the second year of a contract do do analysis in support of three Phillips Laboratory flight experiments.

The PASP Plus effort is an examination of the interactions of the PASP Plus spacecraft and test solar cells with the low-energy plasma environment. This report describes work to develop an analytical model of parasitic current and a preliminary examination of some of the flight data.

The SPREE effort is the use of comparison with flight data to examine, improve, and validate sheath and electron collection models and to examine some of the interactions that determine the spectrum of the incident ions.

The CHAWS effort is the development and validation of models of the spacecraft wake, including the currents to the various detectors of the CHAWS wake-side sensor on the Wake Shield Facility.

14. SUBJECT TERMS Photovoltaic Array Space Power Plus Diagnostics (PASP Plus), Shuttle Potential and Return Electron Experiment (SPREE), Charging Hazards and Wake Studies (CHAWS), solar array parasitic current collection, Tethered Satellite System (TSS-1), electrodynamic tether, spacecraft charging, Wake Shield Facility (WSF), spacecraft wakes

15. NUMBER OF PAGES 110

16. PRICE CODE

17. SECURITY CLASSIFICATION OF REPORT	18. SECURITY CLASSIFICATION OF THIS PAGE	19. SECURITY CLASSIFICATION OF ABSTRACT	20. LIMITATION OF ABSTRACT
Unclassified	Unclassified	Unclassified	SAR

TABLE OF CONTENTS

TABLE OF CONTENTS (cont.)

TABLE OF CONTENTS (cont.)

1. INTRODUCTION

This contract involves research in support of three Phillips Laboratory flight experiments, PASP Plus, SPREE, and CHAWS.

PASP PLUS

The objective of the PASP Plus analysis portion of this contract is to examine the interactions of the PASP Plus spacecraft and test solar cells with the low-energy plasma environment. Using calculational and experimental data, we are developing validated models of the parasitic current collection by the test arrays. Using calculations and experimental data, we will analyze the strengths and weaknesses of solar array arcing models.

The primary contributors to this portion of the contract were Dr. Victoria A. Davis and Ms. Barbara Gardner.

Using the Gilbert code, we examined in detail the current collection properties of a single interconnect or solar-cell gap. We developed a formula for all of the solar array geometries flown that gives the current collected as a function of the plasma and electrical parameters. A discussion of this work is in Chapter 2.

We modeled the experiment panels of PASP Plus to look for any interference of sheaths and the range of plasma and electrical parameters at which interference might affect the experiment results. A discussion of this work is in Chapter 3.

We modified the solar array module of the EPSAT computer code for use by this project. The current to a solar array is now computed by adding together the current to all the interconnects, gaps, and edges of the solar cells. Information on the environment is used by the formula the computes the current to each interconnect, gap, or edge. Updated documentation is included in Chapter 12.

We examined flight data. We confined ourselves primarily to data collected with the emitter off (so that density measurements are available) and with the solar arrays facing the ram. We compared the Langmuir probe measurements with models. We examined current collection as a function of bias and plasma density, variation within a measurement, and APEX current collection characteristics and floating potential. We compared the measurements with calculations, explored some possible reasons for the scatter in the data, and examined current collection under negative bias, and collection by the APSA array. These investigations are discussed in Chapters 4 through 12.

We presented a paper "Parasitic Current Collection in LEO" at the SPRAT conference at NASA/LeRC in Cleveland OH. (Davis and Gardner, *Proceedings of the XII Space Photovoltaic Research and Technology Conference, NASA CP 3278*, p. 227)

We presented a paper "Parasitic Current Collection by Solar Arrays in LEO" at the Aerospace Sciences Meeting and Exhibit in Reno, NV. (Davis and Gardner, AIAA 95-0594)

1.2   SPREE

The objective of the SPREE analysis portion of this contract is to use comparisons with flight data to examine, improve, and validate sheath and electron collection models and to examine some of the interactions that determine the spectrum of the incident ions.

The primary contributors to this portion of the contract were Dr. Gary A. Jongeward and Dr. Ira Katz.

We used an EPSAT model that we developed during the first year of this contract to compare the computed spectrum with SPREE measurements for a period during which the FPEG beam was perpendicular to the Earth's magnetic field. This is the event described in Hardy et al (Observations of Electron Beam Propagation Perpendicular to the Earth's Magnetic Field during the TSS 1 Mission). A discussion of the calculation is in Chapter 14 and documentation for the model is in Chapter 15.

We explored other possible avenues of research.

The paper "Observations of Ionosphere Heating in the TSS-1 Subsatellite Presheath" was published in the May 1, 1994 issue of *Journal of Geophysical Research*. (Katz, et al, *JGR, 99*, p. 8961).

We presented a paper "Observations of Ionosphere Heating in the TSS-1 Subsatellite Presheath" at the 4th International Conference on Tethers in Space in Washington, DC.

1.3   CHAWS

The objective of the CHAWS analysis portion of this contract is to develop and validate models of the spacecraft wake, including the currents to the various detectors of the CHAWS wake side sensor on the Wake Shield Facility.

The primary contributors to this portion of the contract were Dr. Victoria A. Davis and Dr. Myron M. Mandell.

We examined data collected during the flight. We wrote some simple computer programs to assist us in the data analysis.

The EPSAT model of WSF and the shuttle was modified to obtain better values of the floating potential. Hidden surfaces of the engine bells that cannot collect current were defined to be insulating so that they do not collect ram current. The WSF carrier was added to the EPSAT model.

We improved the wake studies model of ion currents in the wake included in EPSAT. The revised documentation is in Chapter 15.

We did rough calculations of the fraction of phase space of the ram ions incident on WSF that reach the center of the wake side of the disk.

We presented a paper "CHAWS Wake Side Current Measurements: Comparison with Preflight Predictions" at the 33rd Aerospace Sciences Meeting in Reno, NV. (Mandell et al, AIAA 95-0489).

2. PARASITIC ELECTRON CURRENT DENSITY TO A SOLAR CELL SIDE

The parasitic electron current to a solar array is attracted by the positive bias on the exposed sides of the solar cells and the exposed interconnects. To compute this current we first compute the current per unit length of solar-cell side or interconnect as a function of geometry and plasma conditions. We are using the results to compute the current collected for the solar cells tested in space and comparing the results with the space results.

In order to compute the current to a solar cell side and interconnect, we use the Gilbert computer code. Gilbert is a general-purpose, two-dimensional, plasma analysis code. It can be used to solve for the electrostatic potential about an object, with flexible boundary conditions on the object and with space charge computed either fully by particles, fully analytically, or in a hybrid manner. For this study Gilbert is used to first compute the electrostatic potentials in the space around the solar cells and then to compute the electron trajectories in the previously computed potentials. The space charge was computed using an analytic formulation.

In cross section, the gap between solar cells looks as shown in Figure 1. The interconnect and solar cell side are at a known positive bias. The other surfaces are insulating. They all adjust so that the net current to each location vanishes.
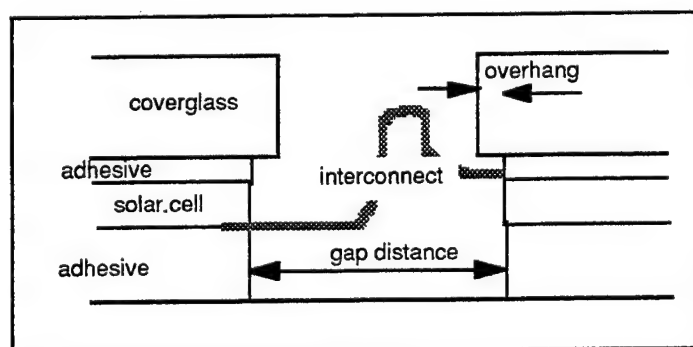

Figure 1. Solar Cell gap region.

Far away from any elevated potentials, an insulating surface has a negative potential a few times the plasma temperature, such that the attenuated electron thermal current balances the ion thermal current. When the ions have directed motion (ram ions), the

insulating surface has a smaller, but still negative potential that depends on the orientation with respect to the ion motion. Therefore, far away from the solar cell gap region, the coverglass potential is taken to be a few times the plasma temperature. The dependency of the collected current on the coverglass potential was explored.

If the potential of an insulating surface is above the first crossover energy of its secondary electron yield curve, then each plasma electron attracted to the surface generates more than one secondary electron. If a nearby surface is at a still higher potential, the secondary electrons are attracted to the higher potential surface. A high potential can be maintained through the current balance between the incident plasma electrons, the incident secondary electrons from other surfaces, and the escaping secondary electrons. This phenomenon is referred to as "snapover".

Gilbert has a boundary condition for surfaces that can snap over. The coverglass surface, the exposed adhesive, and the bottom of the gap (all the insulating surfaces) are all defined to have this boundary condition. The algorithm requires two parameters, the potential of the surface when it is not snapped over and the first crossover energy. For all the insulating surfaces, the non-snapped-over potential is taken to be the coverglass potential. All of the insulating surfaces are taken to have the same first crossover energy. In actuality, the first crossover is different for each material. The dependency of the collected current on the first crossover energy was explored.

We model current collected by specifying a potential value which defines the sheath contour from which particles are emitted, the charge and mass of the particles, the energy of the particles, and the number of particles emitted per grid segment. The trajectories of these particles in the potential field calculated by Gilbert are tracked for a maximum number of steps until the particle is either collected by (hits) a conducting surface, lost to the system (hits the sides of the grid), or the maximum number of steps is reached. The current collected by each conducting surface is recorded.

In the following sections we address several issues relevant to our choices in modeling the potential contours and current collected. These issues are: parameter limits and relationship for the grid we have chosen, modeling of contour levels near surfaces, sheath emission near surfaces, value of the potential used to define the sheath contour, number of particles to track and number of steps for each particle to ensure acceptable relative and absolute errors, and an examination of the predicted results under

conditions of orbit-limited and space-charge-limited current collection. We also study the effects of surface snapover, noting under which conditions snapover occurs, and its effect on current collection, surface current densities and potential contours near the snapped over surfaces.

2.1 Physical Dimensions of Solar Array Cells

For our preliminary calculations, we use a grid which models the conventional solar-cell gap, as shown in Figure 1. One-fifth of the total grid is shown in Figure 2a and a close-up of the gap region in Figure 2b. The grid is 0.25 m by 0.5 m in order to simplify the process of determining the functional dependence of the current collected on the first crossover of the secondary yield. This grid has the disadvantage that it corresponds to solar cells that are about 1000 times as wide as they are thick. A more reasonable ratio is about 100.
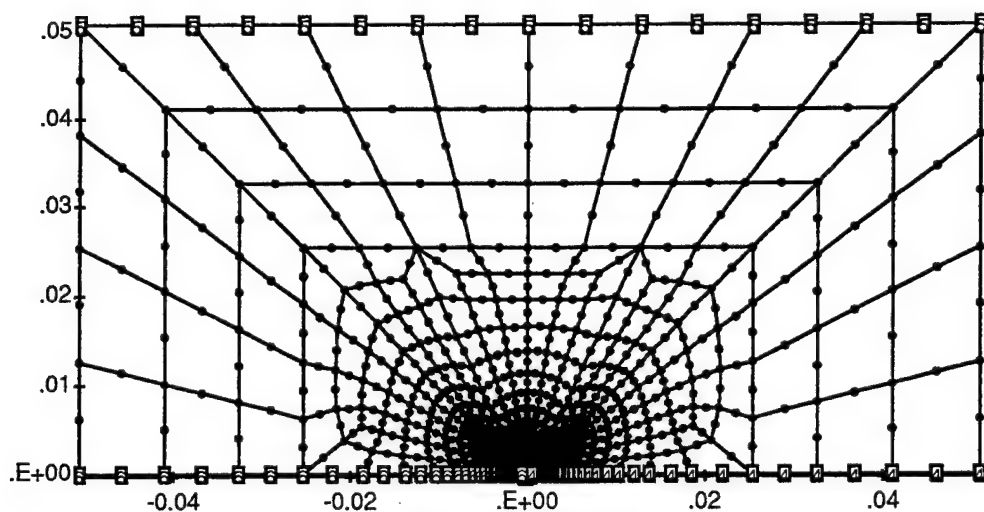
Figure 2a. Grid used for potential and particle tracking calculations.
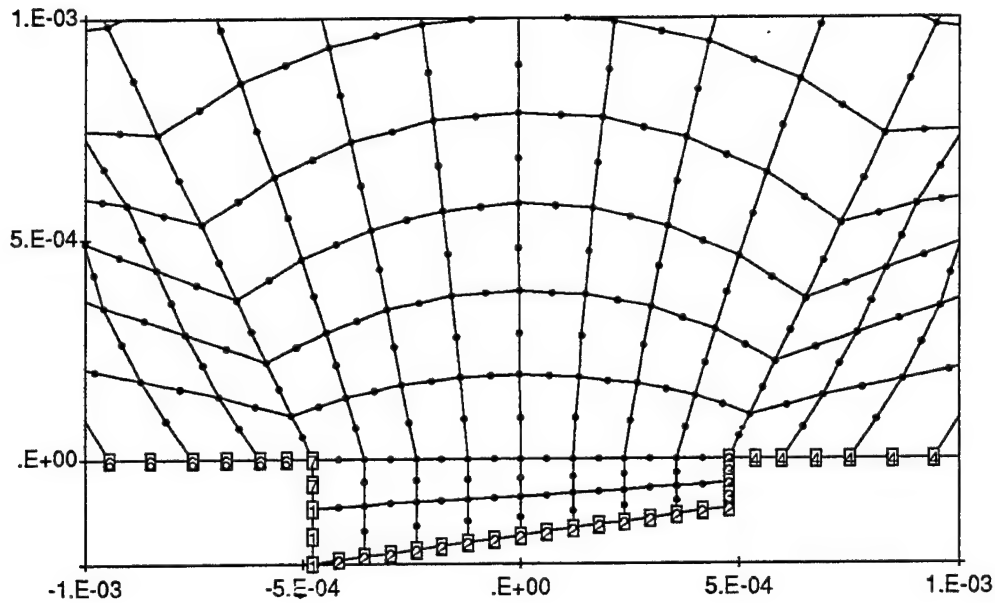
Figure 2b. Close-up of grid near solar cell gap region.

The gridded-up area represents the space above the solar cells, while the blank area at the bottom and below the fixed potential boundary condition surfaces #2, #4, and #6 represents the solar array. Note the following features of the grid, as shown in Figure 2b: there is no overhang, and the interconnect in the gap region (surface #2), has been modeled as a diagonal surface from the bottom of one cell side to the top of the other. The coverglass and adhesive thicknesses have been combined (surfaces #3 and #7), the solar cell side is represented by surface #1, and the coverglass by surfaces #4 and #6.

The physical dimensions of this grid are:

Coverglass + adhesive thickness = .875 × cell thickness
Gap distance = 6.875 × cell thickness

The cell thickness sets the length scale. For our calculations, we will take the cell thickness to be 5 mil or 1.27×10^{-4} meters.

The upper boundary of the grid (#5 in Figure 2a) is fixed at 0 volts. This is valid only so long as the sheath fits within the grid boundaries.

2.2 Typical Potential Solution

Figure 3a shows potential contours for the full grid for the limiting case of plasma density (n_o) equal to 10^{11} m^{-3}, and a plasma temperature (θ) of 0.2 eV. The solar cell potential is 150 volts with a first crossover energy for the coverglass surfaces of 50 volts, which allows a portion of that surface to snapover. The "F" and "G" contours are those of the 0.45θ and 0.7θ potential levels, respectively.

Figure 3b shows a close up of the solar cell gap region. Notice that the coverglass surface is at a positive potential for about $\pm 7 \times 10^{-4}$ meters on either side of the gap region. The surface area capable of collecting current is thereby enhanced in the case of snapped-over surfaces. Here the "G" contour is at 10 volts.

One of the issues we address is the appropriate boundary condition along the coverglass surface, specifically in those regions where the coverglass surface is shadowed by the sheath. The coverglass surface potential is generally one to two times negative the plasma temperature. The test of this modeling of the surface potential near the gap is whether the electron density near that surface is adequate to set up the current equilibrium necessary for the zero net current boundary condition on the surface. See the section on snapover and surface current density for a detailed discussion of this issue.
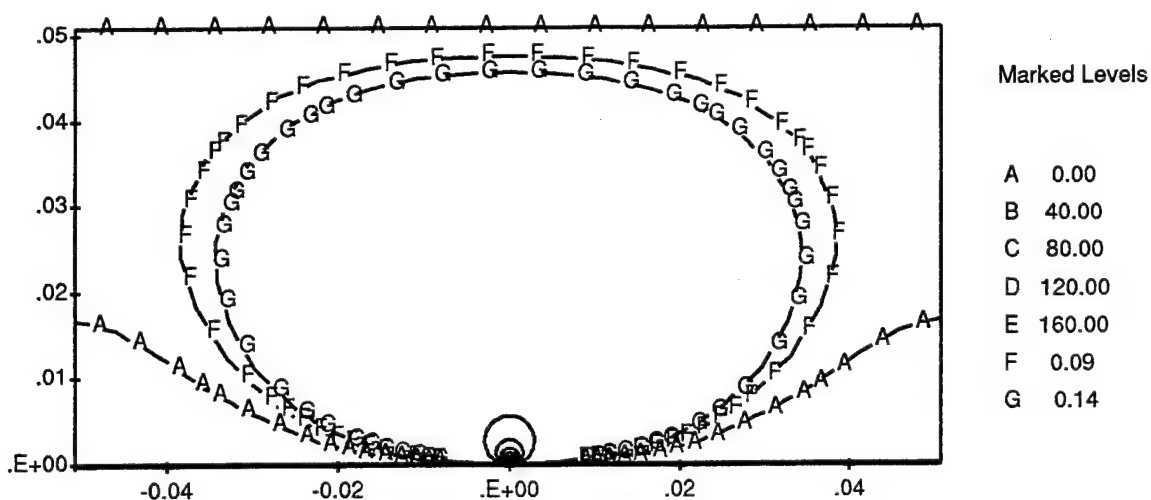

Marked Levels	
A	0.00
B	40.00
C	80.00
D	120.00
E	160.00
F	0.09
G	0.14

Figure 3a. Potential contours showing the beginnings of grid limiting.

Marked Levels

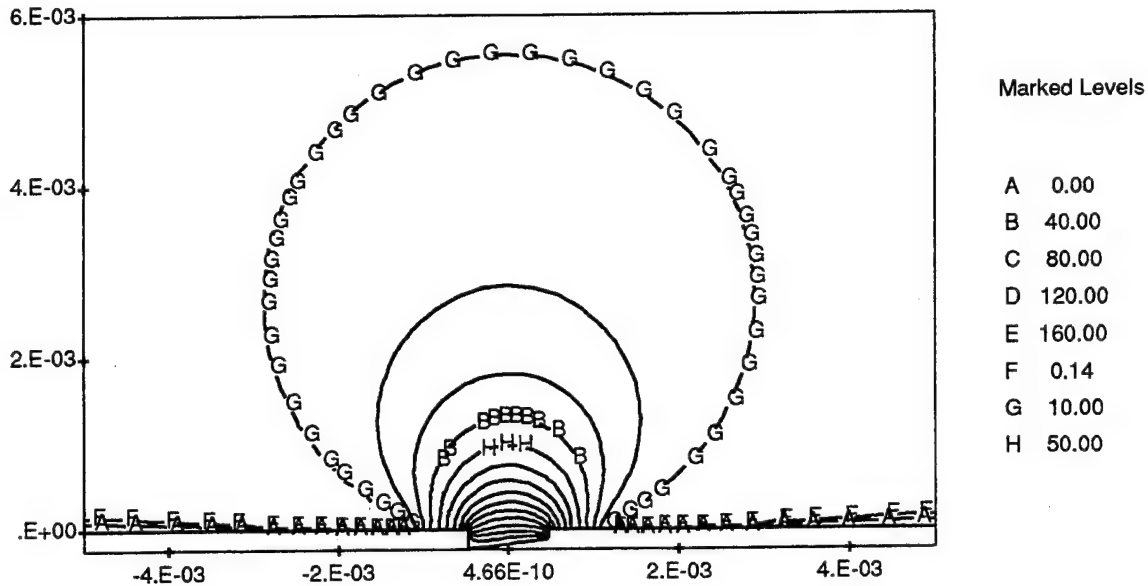|	
A	0.00
B	40.00
C	80.00
D	120.00
E	160.00
F	0.14
G	10.00
H	50.00

Figure 3b. Contours near gap region showing some coverglass surface snapover.

2.3   Sheath Emission/Particle Tracking

Current collection is modeled using a particle tracking program and the potential fields calculated by Gilbert. Variables to the particle tracking program include particle charge and mass, total energy, the potential level from which the particles are emitted, the number of particles emitted per sheath element, the maximum number of tracking steps, and an emission window. Charge and mass values are those of an electron, while the total energy used is θ/π. The sheath surface is taken to be the contour level at 0.7θ. We look at the effect of the choice of the number of particles per sheath segment and the maximum number of steps. We define the emission window to disallow spurious emission from those parts of the sheath very close to surfaces.

2.4   Maximum Number of Steps for Particle Tracking

We limit the maximum number of steps for particle tracking to 10^3. Smaller values ($\sim 10^2$) result in too many particles exceeding the maximum before being collected or lost. Larger values (10^4) result in too much "bouncing around" of particles which leads to numerical error ("accidental" collection of particles), and a significant increase in time of calculation.

2..5   Sheath Emission Near Surfaces

With the maximum number of tracking steps at 10^3, particles with angular momentum such that they cannot be collected, do not in fact get collected. Therefore, we need not limit sheath emission except in those regions of the sheath very near the gap region. We know that no real particles are coming from this region. If particles are allowed to be produced by this segment of the sheath which is in an area of extremely high electric field, a few of these particles get collected. Hence we set the emission window such that no particles within 5×10^{-5} meters of the surface are created. This value removes the spurious particles without affecting true current collected values, even for very small sheaths.

2.6   Multiple Particle Emission from Sheath Segments

We examine the effects of multiple particle emission from the sheath segments on current collected using typical parameter values, e.g., plasma density = 10^{12} m^{-3}, temperature = 0.1 eV, cell potential = 150 volts, surface potential = -0.2 volts, first crossover energy = 50 volts. As expected, the increase in number of particles tracked does not increase the accuracy of the calculation. The variation indicates that the overall percent error in calculated current collected is on the order of 10%.

2.7   Snapover and Surface Current Density

If some amount of the coverglass surface is snapped-over to a positive voltage due to secondary electron emission, that part of the surface will collect current in addition to the cell and interconnect surfaces. As a result of this increased current collecting area, the emission sheath radius is larger, allowing for a greater area from which to collect current. Snapover also affects angular momentum limiting of current collection, which we will discuss in detail in Section 5.

For $n_0 = 10^{12}$ meter^{-3} and $\theta = 0.1$ eV, giving a Debye length of 2.3×10^{-3} meter, we examine the effects of the following variables on coverglass surface snapover and current collection:

cell/interconnect potential = 10 to 4000 $\times \theta$
coverglass potential = 0 to $-5 \times \theta$

snapover potential = 0.1 to 4 × cell/interconnect potential

This gives us cell potentials ranging from 1 to 400 volts, coverglass potentials from 0 to -0.5 volts and snapover potentials from 0.33 to 450 volts.

An examination of the results reveals that a first crossover energy of less than about 1/3 the cell potential results in at least 2% of the coverglass surface being snapped over, while a value greater than 1/2 the cell potential results in little or no surface snapover. If all other variables are held constant, varying the first crossover energy from 0.1 time to 1.0 times the cell potential results in a change in the current collected by a factor of three.

Figures 4a and 4b show details of potential contours and particle trajectories near the coverglass surface and close to the cell gap for a case where there is no snapover, while Figures 5a and 5b show potential contours and particle trajectories for a case where the surface is partially snapped-over.
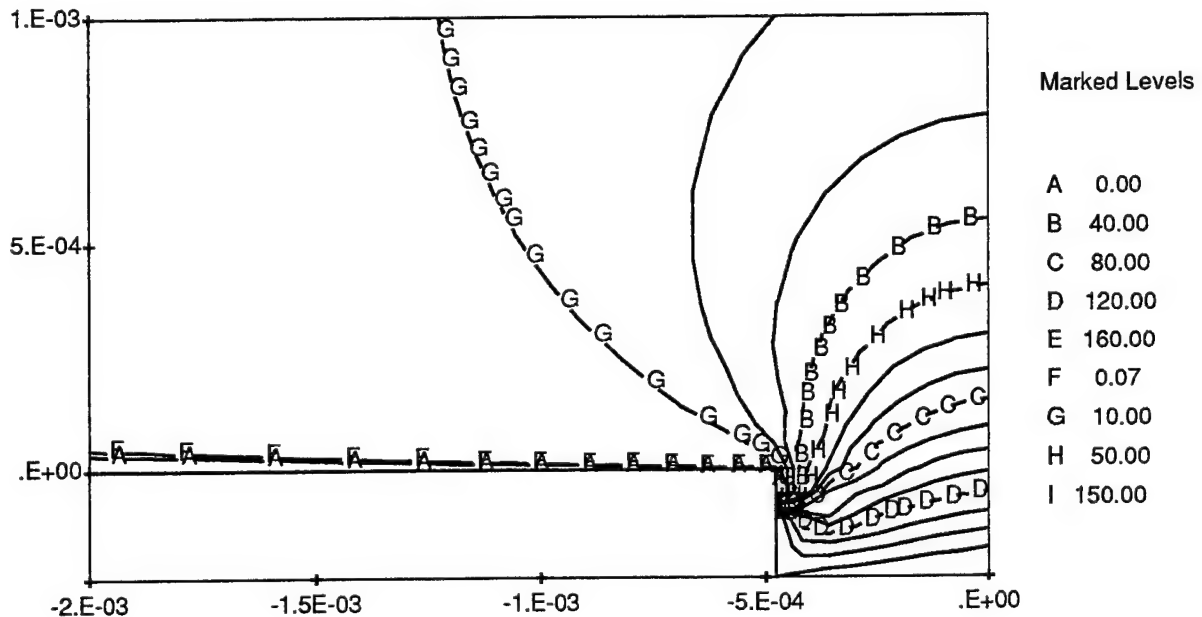

Figure 4a. Potential contours at gap edge with no surface snapover.
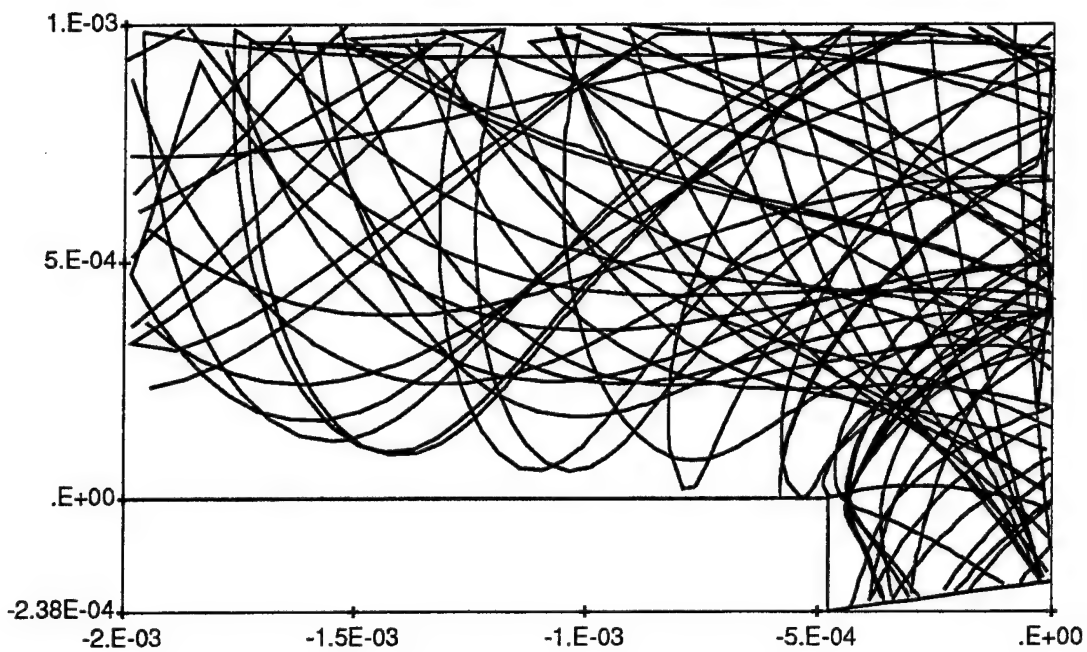
Figure 4b. Particle tracks at gap edge with no surface snapover.

Marked Levels

A 0.00
B 40.00
C 80.00
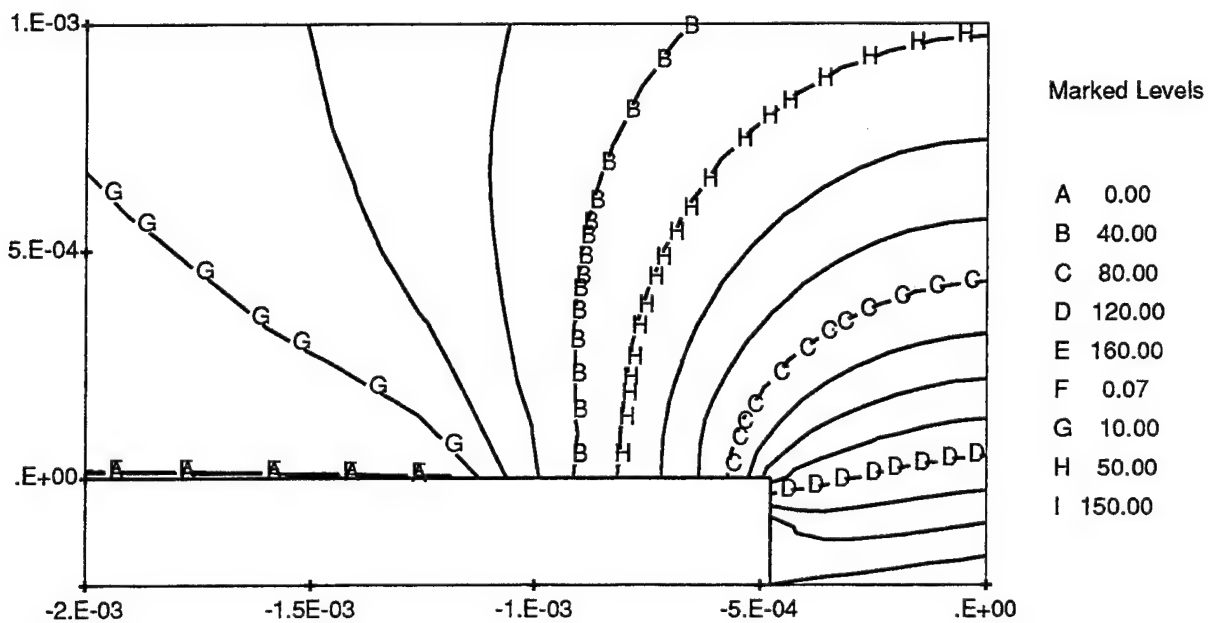D 120.00
E 160.00
F 0.07
G 10.00
H 50.00
I 150.00

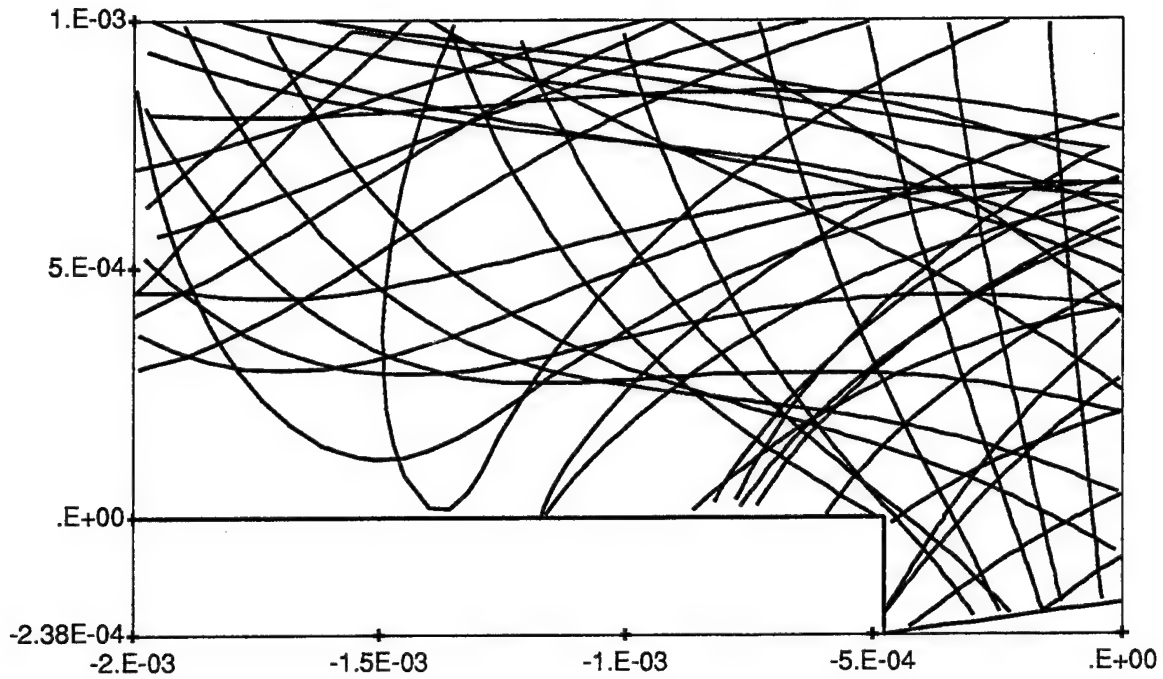Figure 5a. Potential contours at gap edge with some coverglass snapover.

Figure 5b. Particle tracks at gap edge with some coverglass surface snapover.

An important feature to notice in Figure 4b is that electrons approach the coverglass surface all along the surface. The electrons are repelled by the negative surface potential. If the surface was not at a negative potential, electrons would impact the surface until it became negative enough to repel all but the more energetic tail of the electron distribution (since it only takes the energetic tail to balance the smaller ion current.)

2.8   Angular Momentum Limiting of Current Collection

For space-charge-limited current collection, the current collected by the cell and interconnect through a sheath is given by:

$$I_{sh} = J_{th} \times A_{sh} \tag{1}$$

Where A_{sh} is the sheath area, and J_{th} is the thermal current.

When the extent of the space charge limited sheath in the direction parallel to the surfaces is larger than the orbit limited radius, angular momentum limits the current collection. Figures 6a and 6b illustrate this phenomenon. Figure 6a shows those particles emitted by the sheath with angular momentum about the center point of the gap region

13

low enough to be collected. All of these particles originate within a maximum horizontal distance from the center of the gap. That maximum distance is the orbit-limited radius. Figure 6b shows those particles with angular momentum too great to be collected. These particles are lost to the system.
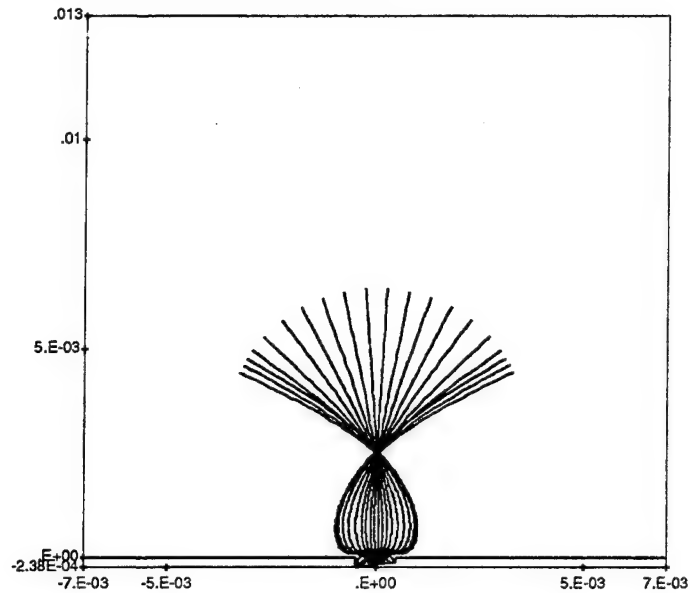

Figure 6a. All particles emitted within an arc segment of the sheath are collected by the solar cell.
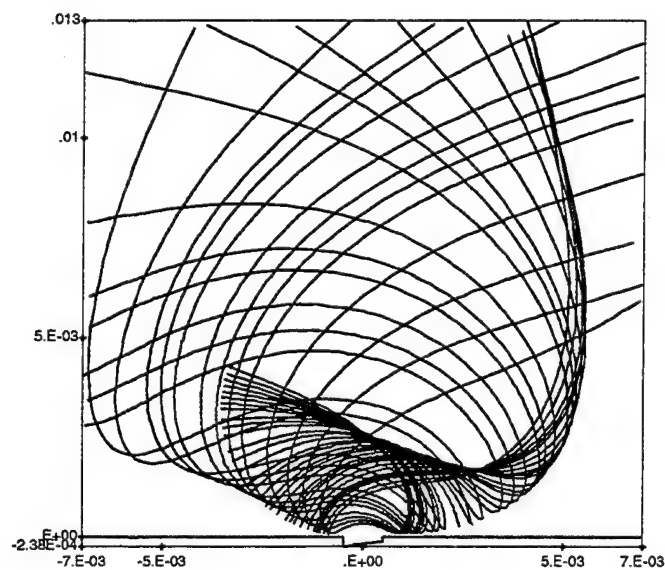

Figure 6b. All particles emitted not within the momentum limiting arc segment are lost to the system.

14

The orbit-limited radius is:

$$R_{ol} = \sqrt{\frac{\theta/\pi + \text{cell potential}}{\theta/\pi + 0.7\theta}} \; R_t, \qquad\qquad (2)$$

where R_t is the target radius.

We can calculate an upper limit on the target radius. If there is no snapover of the coverglass surface, the target radius is one-half the gap distance. When some fraction of the coverglass surface is snapped-over, the target radius and hence the orbit limited radius, increases. An upper limit on R_t in this case is half the total of the gap distance plus that amount of the coverglass surface which shows a positive potential.

For the orbit limited case, the current collected is:

$$I_{coll} = 2 \, R_{ol} \, J_{th} \qquad\qquad (3)$$

Figure 7 shows the sheath radius and orbit-limited radius (R_{ol}) against cell potential for $n_o = 10^{10}$ to 10^{12} m^{-3} and $\theta = 0.1$ and 0.5 eV. The orbit-limited radius, which is represented by the heavy lines, depends on cell potential and θ, while the sheath radius, represented by the thin lines, depends on n_o as well. We expect to see orbit-limited current collection at lower densities and temperatures, and at higher densities and temperatures for large values of cell potential. In all cases, the first crossover energy was large enough that coverglass surface snapover did not occur. When snapover occurs, the effective "target radius" is larger, as is the sheath radius.

15

Cell Potential (V)
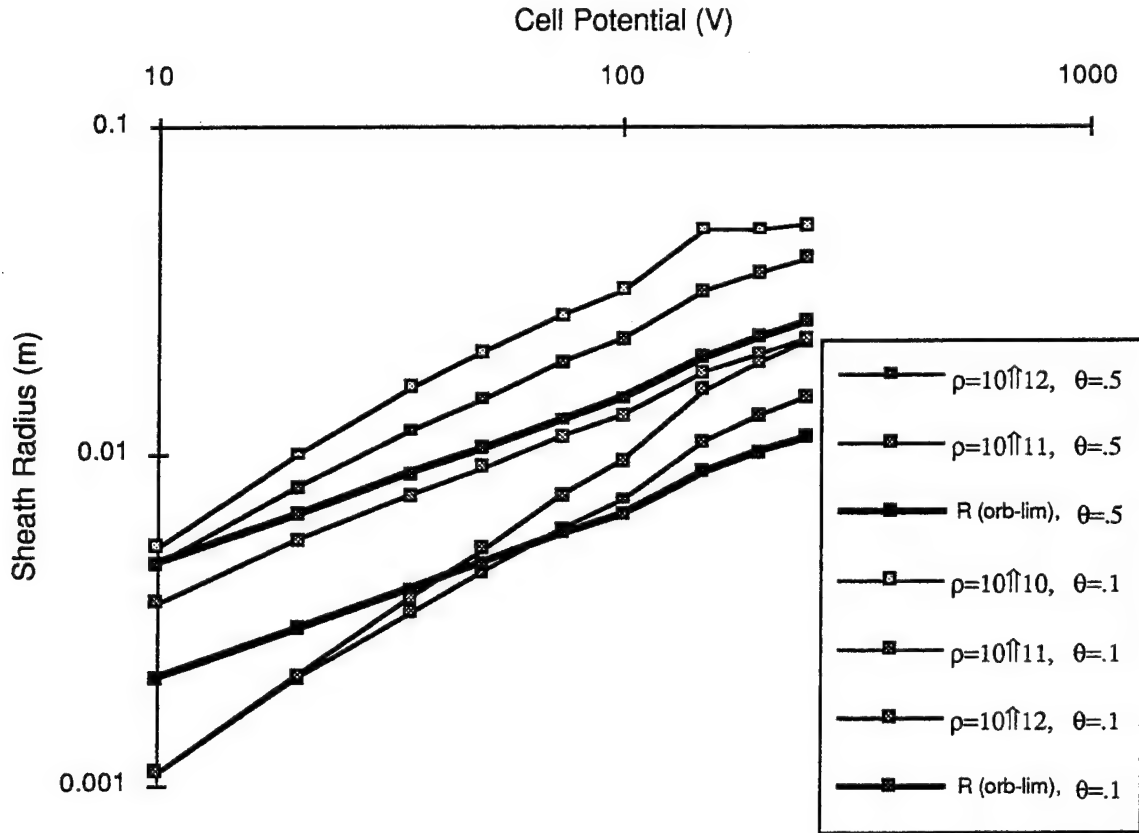
Figure 7. Sheath radius decreases for increasing plasma density and temperature.

2.9 Limits on Validity of Approach

The approach we are taking for the bulk of our calculations is not appropriate for all circumstances. A different approach would be needed for the following circumstances:

a. If we have a case of orbit-limited current collection and the orbit-limited radius is larger than the horizontal grid dimension.

b. If we have a case of space-charge-limited current collection and the sheath contour does not fit within the grid, including the vertical direction. For example, if the first crossover energy is ~0.1 times the cell potential, a large fraction of the coverglass is snapped over and the sheath contour is outside the grid limits for many values of the cell potential.

c.   If the cell potential is small enough (~20 volts) and the coverglass potential is also low (~-10 volts), there is a potential barrier over the cell-to-cell gap. This is particularly important for modeling SSF, Module 3.

2.10   General Character of Results

We did calculations for three base cases, Interconnect, No Interconnect, and Edge. The names reflect the basic geometry. The cell thickness, gap width, and cover glass thickness are the same in all three. For each case, collected current versus cell potential curves at four different densities were computed for five different values of the cell potential to first crossover potential ratio. The quantity calculated was the sheath length. The sheath length is the current collected divided by the plasma thermal current. In some sense, this is the length of the "sheath segment emitting current." The temperature used was 0.1 eV. To get results for another temperature, all of the other variables must be scaled appropriately. For example, a 0.1 eV, 3.2×10^{11} plasma, 200 V cell potential, 0.5 V surface potential, 50 V first cross over case is equivalent to a 0.2 eV, 6.4×10^{11} plasma, 400 V cell potential, 1 V surface potential, 100 V first cross over case. Calculations were done with surface potentials of –0.5 V and 0 V on the cover glass where it is not snapped over. The negative value is appropriate for a thermal plasma.

The collected current increases as a power law with voltage. Lower densities provide less screening. With less screening, the sheath and therefore the current is larger. At the lowest potentials, the debye length is larger than the sheath size, and the current is independent of the density. At low densities, the computed current is sometimes depressed because macroparticles are emitted from only part of the sheath. The physical and computational reasons for the suppression of current are discussed below.

2.11   Thermal Distribution of Macroparticles

To compute the current, macroparticles are created at a sheath edge and tracked in the electric fields created by the potentials on the interconnect, solar-cell sides, and coverglass.

In many of the cases of interest, the applied voltage is high enough that the thermal distribution in direction and speed of the collected electrons at the sheath edge does not effect the current collected. However, when angular momentum conservation

17

dominates the current collection process, the small initial velocities can become important.

The current computed using the thermal distribution is either the same or lower than the zero-temperature case. When the screening is high, the difference is small. When a large fraction of the surface is snapped over, the temperature effect is also small. The importance of this effect does not appear to vary with the ratio of the biased area to the coverglass area.

2.12 Macroparticles Originating Near Grid Boundaries

Macroparticles that originate within two debye lengths of a grid boundary require a closer examination.

Macroparticles originating near object surfaces are fictitious. Real electrons originate within the plasma. In general, for our calculations, these macroparticles have too much angular momentum to be collected. However, sometimes they are collected. And just as important, the grid is such that large numbers of these fictitious particles are generated and tracked. Eliminating these macroparticles leads to a several fold increase in speed of calculation.

Macroparticles are tracked backwards from their initial location for two debye lengths. If the path of a macroparticle intersects an object surface, the macroparticle is rejected as fictitious.

Macroparticles that originate within two debye lengths of the free-space edges of the grid are real, but the potential contours in these locations may be distorted by the grid boundary. We rejected all calculations in which any macroparticle, when tracked backwards for two debye lengths, came from outside the grid.

2.13 Macroparticles Originating in a High Field Region (Barriers)

Generally, the sheath edge is taken to be the location of the potential contour at 0.7 times the electron temperature. However, sometimes this contour level lies in a high field region. For the solar-cell interconnect/solar-cell side parasitic current collection problem, this occurs when electrons would have to pass through a region of negative potential to reach the "sheath edge." Negative potential regions larger than about one-third the temperature are barriers to electrons.
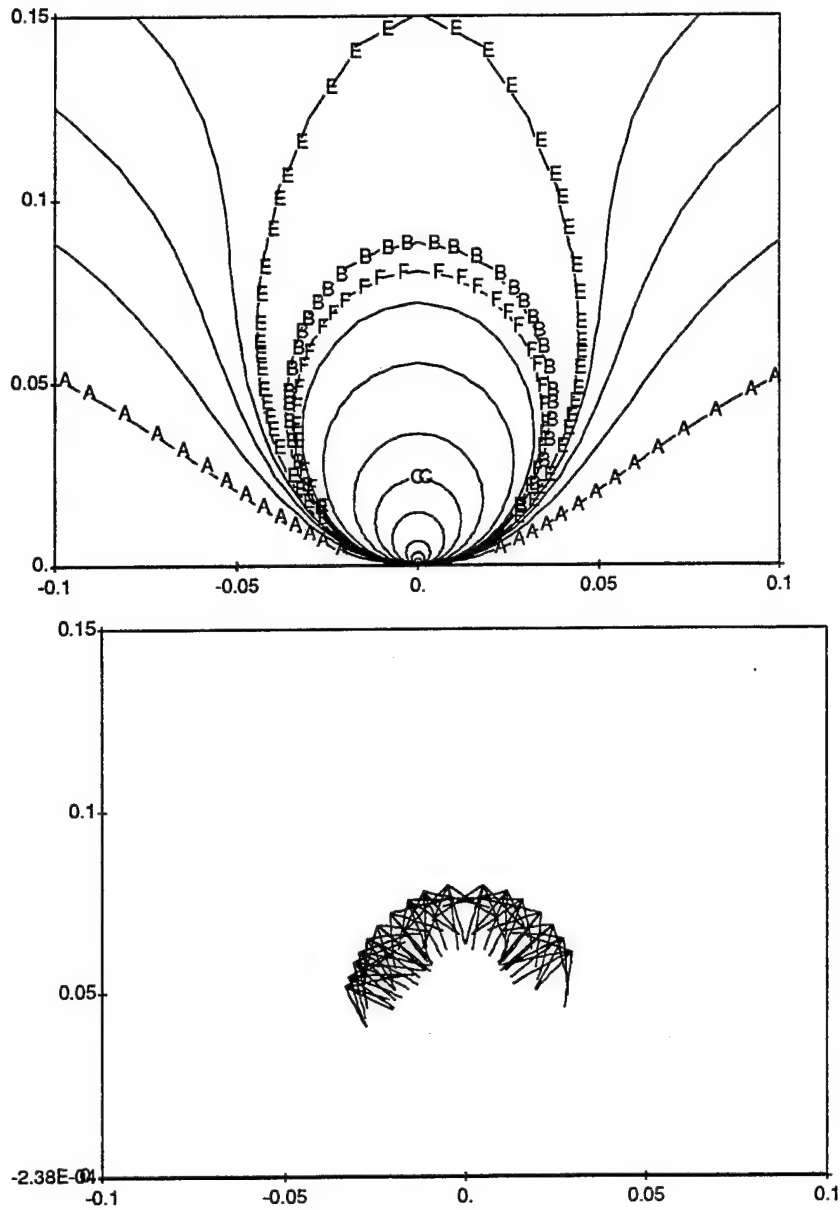
Figure 8. (a) Potential contours for a 3.2×10^9, 0.1 eV plasma, 150 V cell potential, –0.5 V surface potential, 60 V first cross over potential. Macroparticles start at the 0.07 V contour level, which is marked with the character F. The 0 V contour level is marked with the character E. The other contour levels are –0.2 (A), –0.1, –0.05, –0.02, 0.05 (B), 0.1, 0.2, 0.5, 1 (C) , 2, 5, 10, and 20 (D). (b) Initial trajectories of macroparticles in the contours of part (a). The portions of the 0.07 contour level that do not emit macroparticles have high electric fields. Few electrons from infinity reach these segments of the contour level due to the negative potential regions.

19

Presently, we reject macroparticles created in high field regions.

At lower densities, less screening occurs. In general, as the density decreases the sheath gets larger. However, the coverglass potential is also screened less at lower densities. Therefore, a large segment of the sheath may be inaccessible to electrons. The growth of the sheath length as the density drops is curtailed. Sometimes, the sheath length goes to zero.

2.14   More Accurate Snapover Model

We tried an enhanced method to compute surface potentials for snapped over insulating surfaces. We found that the new method of calculation does not significantly change the value of the computed current collected. Primarily because this alternative method has several more free parameters, we are not using it for our calculations. (unless otherwise specified.)

In the simple approach, a special boundary condition is defined for surfaces that can snap over. Potentials are computed with a zero component of the electric field normal to the insulating surface. If the surface potential is above the first crossover of the secondary yield for electrons, no change is made. If the surface potential is below the first cross over of the secondary yield, the surface potential is set to a small negative potential. The process is iterated until a convergent solution is reached.

In the alternative approach, rather than requiring the electric field to have a zero normal component, charge is deposited on the surface nodes so that the electric field has a small positive component. The amount of charge deposited is proportional to the square root of the secondary yield of the insulating surface. The secondary yield as a function of incident electron energy is given by a six parameter function. (The incident electron energy is approximated by the surface potential.)
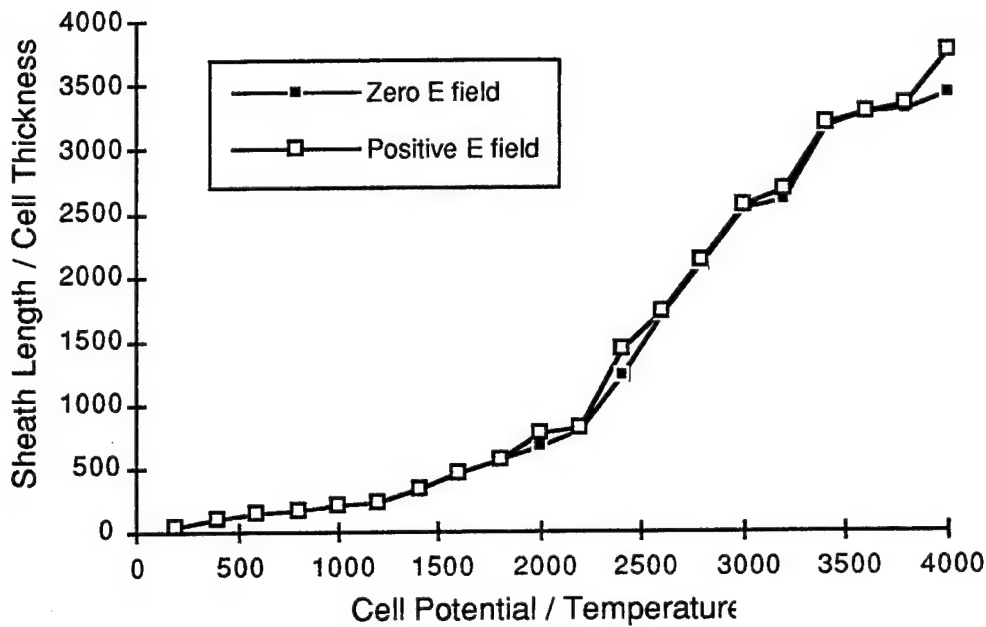
Figure 9. Collected current versus cell potential for 3.2×10^{11}, 0.1 eV plasma, –0.5 V surface potential, 50 V first crossover potential. The two curves are computed with a model in which the snapped over portion of the surface has a normal electric field component of zero and in which the snapped over portion of the surface has a small positive component. The secondary yield parameters used are the following: peak secondary yield for normally incident electrons, 2.1, energy at which the secondary yield peaks for normally incident electrons, 225 eV, and four biexponential range parameters, 71.5, 0.6, 312, 1.77.

2.15   Impact of Cover Glass Area

Most of the calculations were done with a grid in which the coverglass is 0.25 m wide, rather than the realistic width of 2 to 4 cm. In order to estimate the impact of this decision, special grids were constructed. In these special grids, nodes that are further than 2 cm from the center of the gap were set to 0 V and not allowed to snap over.

In general, the results with the special grids are the same as the results with the standard grids. As there is less negative potential surface, the current reductions due to barrier formation are expected to be less, and this is seen. In the high snapover cases, the

21

region snapped over is constrained to be no more than 2 cm. This effect is seen in the 0.1 snap, low-density cases as the sheath is smaller when less snapover can occur.

2.16   Impact of Cover Glass Surface Potential

For a ram-facing insulating surface in low earth orbit, the surface potential is about –0.5 V. At other orientations and in the slower moving portion of the APEX orbit, the cover glass surface potential may be on the order of –0.2. When there is a large amount of snapover the coverglass surface potential has little impact. When the sheath is small enough (or the density low enough) that screening is not significant and there is almost no snapover; halving the surface potential is equivalent to doubling the cell potential. The range of parameters for which this occurs is small.

The most significant impact of the coverglass surface potential is in determining the average surface potential. In general, the results with a surface potential of –0.2 V are the same as those obtained with a surface potential of –0.5 V. As the average surface potential is smaller, the current reductions due to barrier formation are less.

2.17   Analytic Fit

For a given geometry, cover glass potential, cell potential, first crossover potential, plasma density, and temperature, Gilbert was used to compute the sheath length (collected current) as previously defined. All calculations were done for a plasma temperature of 0.1 eV, as the results depend only on the ratios of the potentials to the temperature and the ratio of the temperature to the density.

We surveyed the effect of the geometry by doing calculations for a variety of different geometries with a coverglass potential of 0 V. The coverglass thickness was varied from 0 to 1.75 times the cell thickness. The gap distance was varied from 3.4375 to 13.75 times the cell thickness. The thickness of the adhesive between the cell and the circuit board was varied from 0 to 1.5 times the cell thickness. The overhang was varied from 0 to 0.4 times the cell thickness.

The extent of the snapped over region provides an intermediate variable that assisted us in fitting the results. We conjectured that:

$$\frac{\text{Sheath Length}}{\text{Snapover Extent}} \propto \left(\frac{\text{Cell Potential/Plasma Temperature}}{\text{Snapover Extent/Cell Thickness}} \right)^{N} f\left(\frac{\text{Debye Length}}{\text{Cell Thickness}} \right) \qquad (4)$$

where N, f, and the proportionality constant are independent of geometry. We found that $N = 0.35$ and the function

$$f(\lambda) = \exp\left(-3/\lambda^{0.7}\right) \qquad (5)$$

where λ is the debye length over the cell thickness, provided a good fit to the calculated points. The quality of the fit is consistent with the precision of the calculations. The form of the function f was chosen because it fit the calculational results significantly better than a power law in the debye length. Figure 10 shows the quality of the fit.
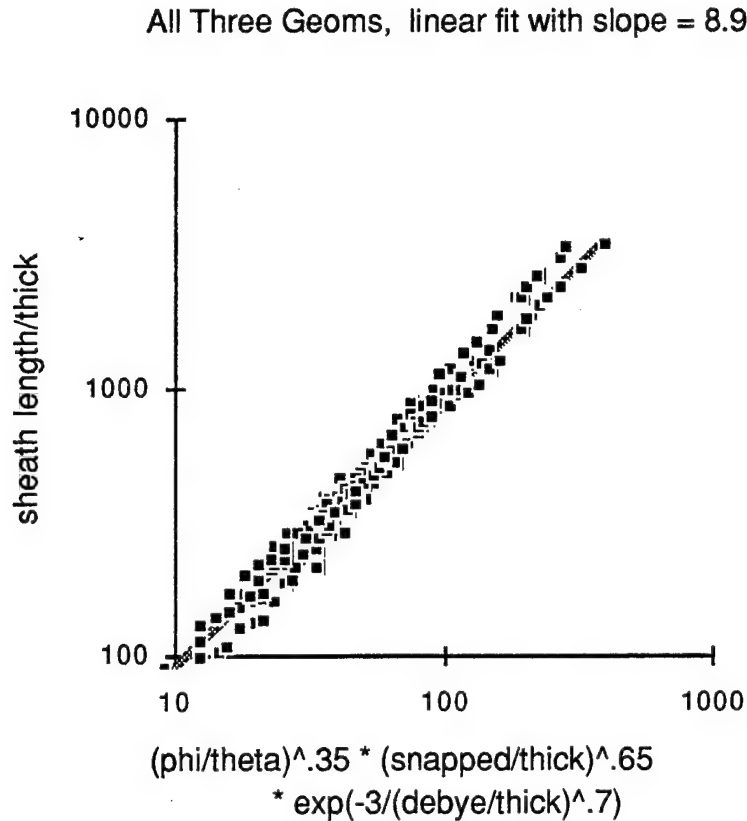

Figure 10. Quality of fit of the sheath length as a function of the extent of the snapped over region.

Developing a formula to fit the extent of the snapped over region as a function of the cell potential, debye length, and snapover potential was more difficult. Because, in the calculations, the snapover extent is an integer number of grid points, it was necessary to use a large number of calculations to smooth out the grid effects. Over five thousand calculations of the snapover extent for values of η (defined below) of 0.15 to 0.6 and the full range of cell potentials and plasma densities were done for each of the three baseline geometries.

$$\eta = \min\left(1, \frac{\text{1st crossover potential}}{\text{cell potential}}\right) \tag{6}$$

The following observations helped guide the choice of functional form. The snapover extent increases with increasing cell potential, increasing debye length, and decreasing snap. The dependence on potential and debye length is not strong. The dependence on η, is exponential. The snap extent grows faster with debye length at smaller values of snap. At larger values of cell potential and debye length, the dependence of the snap extent on these quantities appears to approach a limiting value. Fits were made to several different functional forms. The following form provides a reasonable fit.

$$\text{Snap Extent} = \frac{1}{\eta} \exp\left(\frac{a}{\lambda^{0.7}} + \frac{1}{\eta}\left(0.75 + \frac{-10.8}{\phi} + \frac{-1.7}{\lambda^{0.7}}\right)\right) \tag{7}$$

where

$\eta = \min(1, \text{1st crossover potential/cell potential})$

$\phi = \text{cell potential/plasma temperature}$

$\lambda = \text{debye length/cell thickness}$

The value of "a" varies from –1.5 to –5, depending on the gap region geometry being fit. The quantity ϕ is the cell potential divided by the plasma temperature. The quantity λ is the debye length divided by the cell thickness.

This form also provides a reasonable fit for η values from 0.6 to 1.0 for the edge and the interconnect geometries. However, there is a sharp change in sheath extent at an η value

24

of 0.6 for the no interconnect geometry. At an η value near 0.6, the entire interconnect region goes from little snap over to fully snapped over with a cell potential change of under 1 V.

We looked at the role of geometry. For various pairs of geometries, we examined the ratio of the sheath lengths for each value of ϕ, λ, and η. We found no significant dependence of the ratio on any of these quantities for any of the geometry variations. We found that the following formula provides a reasonable scaling between the geometries.

$$A(\text{geometry}) = \begin{cases} \text{cell} + \text{gap} - 1.5 \times (\text{c.g.} + 2 \times \text{o.h.}) & \text{interconnect geometry} \\ 2 \times \text{cell} + 0.4 \times (\text{gap} + 2 \times \text{glue}) - 1.5 \times (\text{c.g.} + 2 \times \text{o.h.}) & \text{no interconnect geometry} \\ 1.5 \times \text{cell} + 0.4 \times \text{glue} - 0.5 \times (\text{c.g.} + 2 \times \text{o.h.}) & \text{edge geometry} \end{cases}$$
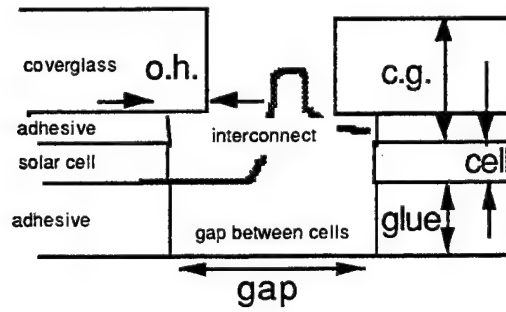

Figure 11. Cell gap region.

An alternative expression uses the variables shown in Figure 12.

$$A(\text{geometry}) = \begin{cases} L + 0.4 \times M - 1.5 \times N & \text{(no) interconnect geometry} \\ 1.5 \times L + 0.4 \times M - 0.5 \times N & \text{edge geometry} \end{cases} \tag{8}$$

where L is the exposed high potential surface, M is the bottom of the gap, and N is the set back.
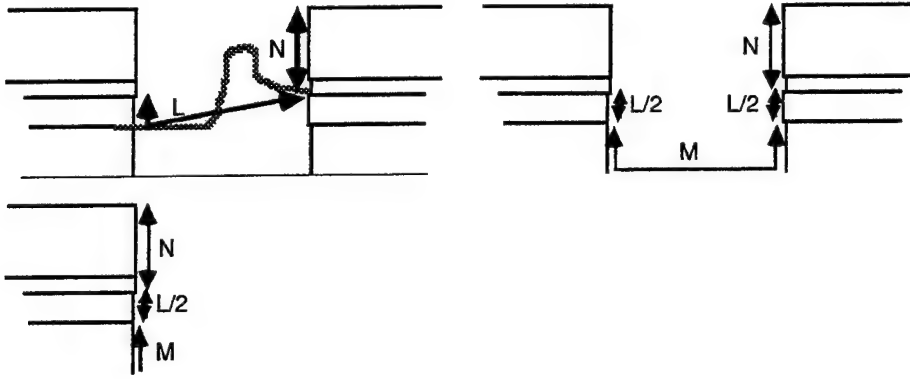
Figure 12. Underlying variables of geometry dependence coefficient.

All of the above were used to determine a functional form of the sheath length as a function of geometry, cell potential, 1st crossover potential, and debye length for the cover glass at 0 V cases. The numeric values in the exponent and the overall coefficient were adjusted to fit the over 2300 calculations with zero surface potential. The final formula is

$$S.\,L. = 1.1\,A\,(geom.)\,B\,(\eta)\,\frac{\phi^{0.35}}{\max{(0.1,\,\eta)}^{0.65}}\exp\left(\frac{0.63}{\lambda^{0.7}} + \frac{1}{\max{(0.1,\,\eta)}}\left(0.44 - \frac{7}{\phi} - \frac{1.13}{\lambda^{0.7}}\right)\right) \quad (9)$$

where the function B is

$$B(\eta) = \begin{cases} 1/3 & \text{no interconnect geometry and } \eta > 0.6 \\ 1 & \text{otherwise.} \end{cases}$$

The basic character of the current voltage curves computed from this formula is similar to those from the calculations. Figure 13 shows the quality of the fit.
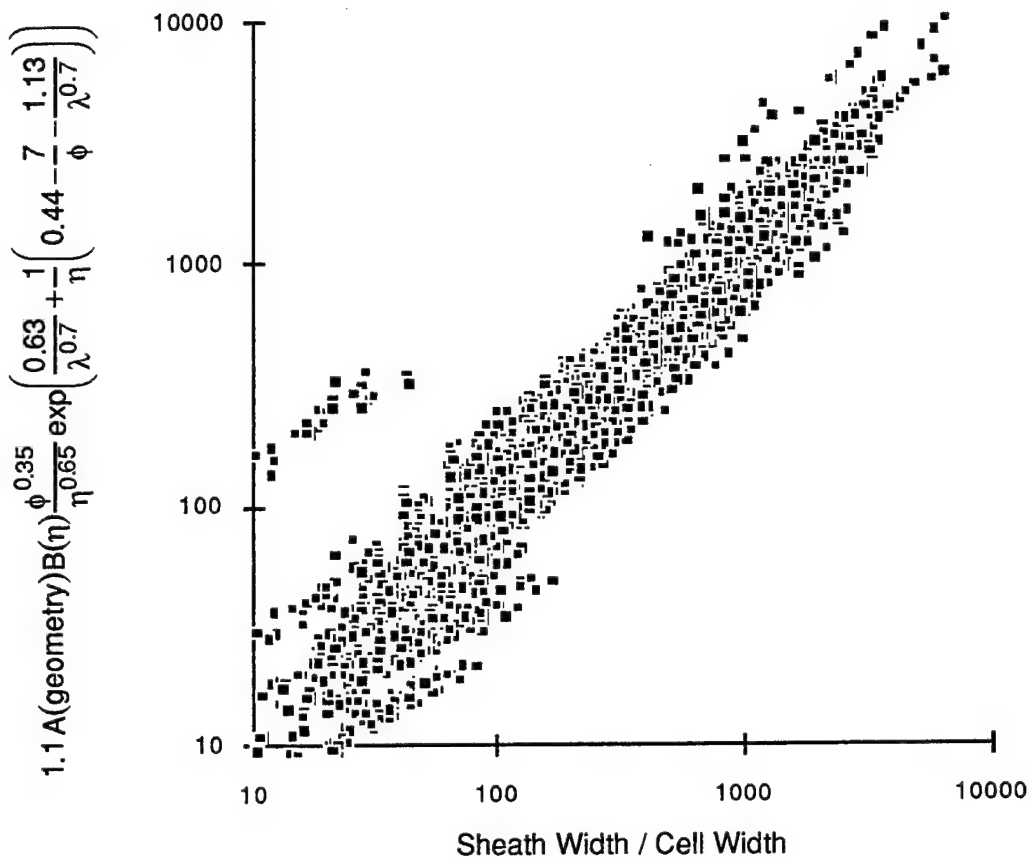
Figure 13. Quality of fit of the formula to the cover glass at 0 V cases.

This formula should not be applied to scaled potential values greater than 500/0.05. This form has appropriate values in all of the limits. At a debye length of zero, the sheath length is zero. As the debye length gets arbitrarily large, the sheath length becomes independent of debye length. At a potential of zero, the sheath length is zero. The function η never gets larger than 1, and the sheath length is strictly independent of η for η values smaller than 0.1.

3.   SHEATH INTERFERENCE

One of the goals of the PASP Plus program is to measure the parasitic current collected by solar arrays at high voltages. Comparison of the flight measurements, laboratory measurements, and calculations will be used to develop rules of thumb, formulas, and computer tools that can be used by future spacecraft designers to quantify and minimize the impact of parasitic current collection on spacecraft operations. Various geometric effects complicate the extension of the PASP Plus measurements to power solar array designs. The PASP Plus arrays consist of a few cells further from each other than typically placed mounted on an insulating plate surrounded by a grounded conducting frame or on top of a grounded conducting base. The array frames are mounted on a panel with an insulating paint on the top and the underlying conductor exposed along the sides. The surroundings can dramatically effect the current collected by the cells. Operational solar arrays consist of a large number of solar cells placed as close as practical and often separated from the rest of the spacecraft. The only effect of the rest of the spacecraft on solar array operations is to determine the solar array ground potential and the load.

The conducting frame or base surrounding each of the solar arrays has two effects on the parasitic current collected: (1) Snapover spreads over the insulating surface around the solar cells, but not onto the surrounding grounded conductor; (2) When spacecraft ground is negative with respect to the plasma, the conducting area reduces the current collected, by as much as several orders of magnitude under some conditions. When spacecraft ground is positive with respect to the plasma, the conducting area usually reduces the current collected by the solar cells, although not as much as for negative bias.

The NASCAP/LEO computer code is being used to quantify the effect of the spacecraft ground on the collected current. Figures 14a and 14b show the model of the hexagonal top of the spacecraft. Figures 15a and 15b show the model of the deployed experiment panel. The extents of the grounded conducting areas are over estimated to make sure that their effect is overestimated rather than underestimated.
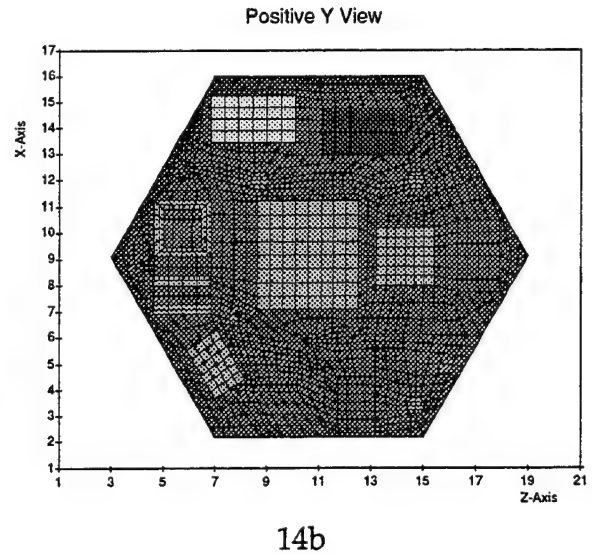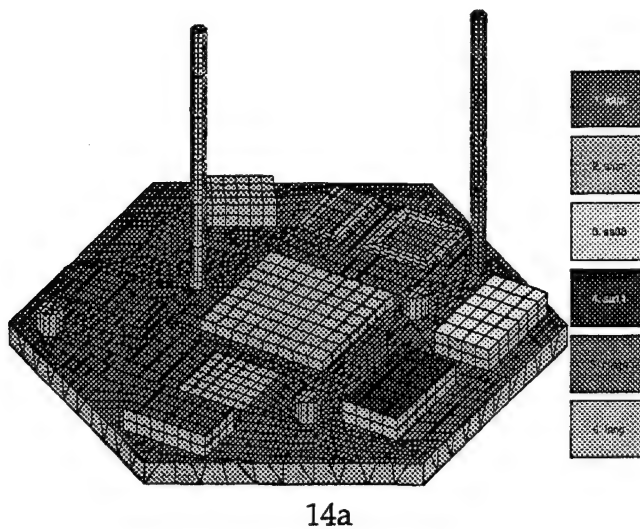
28

14a

14b

Figure 14. CAD/CAM model of the hexagonal top of PASP Plus. The magnetometer and Langmuir probe booms are assumed to be insulating.
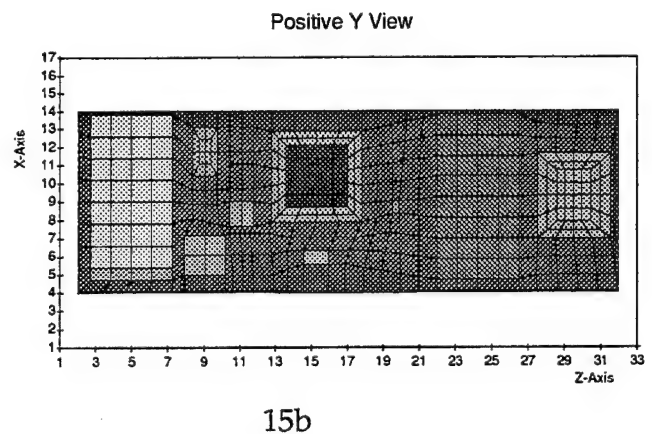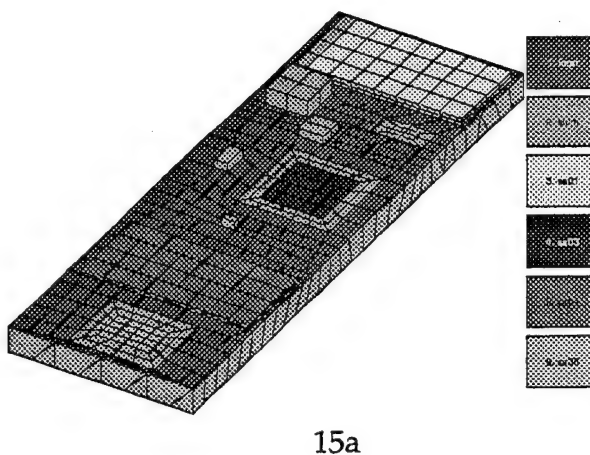

15a

15b

Figure 15. CAD/CAM model of the deployed panel of PASP Plus.

A large number of calculations have been done. A couple of examples illustrate the type of behavior seen, along with some of the complications.

Consider the case of a 10^{11} m^{-3}, 0.1 eV plasma, with the top panel oriented toward the direction of motion. Under these circumstances, insulating surfaces typically have a potential on the order of –0.2 eV. Take the surface of solar arrays 0, 1, and 2 to have an average potential of +10 V. This would be appropriate for the case in which solar array 2 is biased to a potential somewhere between +100 V and +200 V depending on the

29

details of the spread of snapover. Figures 16 a and b show the potential contours in a plane passing through the center of solar arrays 0, 1, and 2 when the ground potential is at 0 V with respect to the plasma. The solar array surface collects 410 µA. This is about four times the plasma thermal current to a surface of this area. Figures 17 a and b show the same case when the ground potential is at –20 V with respect to the plasma. The solar array surface collects 130 µA. Figures 18 a and b show the same case when the ground potential is at +20 V with respect to the plasma. The solar array surface collects 200 µA.

16a   16b

Figure 16. Potential contours in a plane passing through the center of solar arrays 0, 1, and 2 when the ground potential is at 0 V with respect to the plasma. The sheath edge is indicated by the labels.

17a

17b

Figure 17. Potential contours in a plane passing through the center of solar arrays 0, 1, and 2 when the ground potential is at –20 V with respect to the plasma. The sheath edge is indicated by the labels.
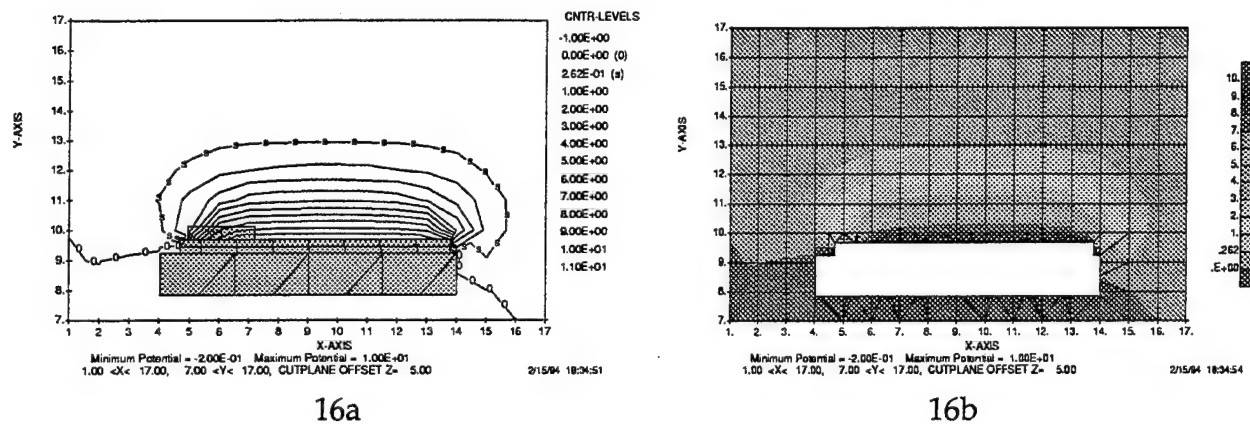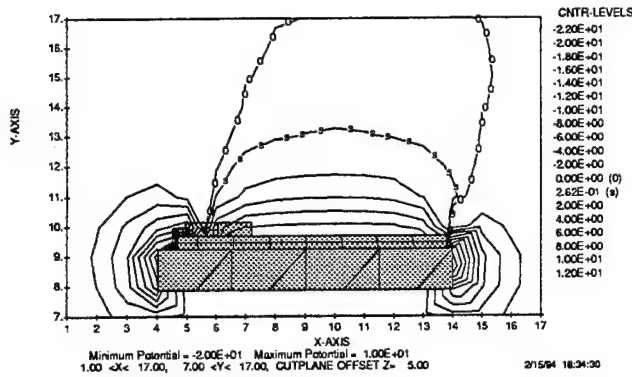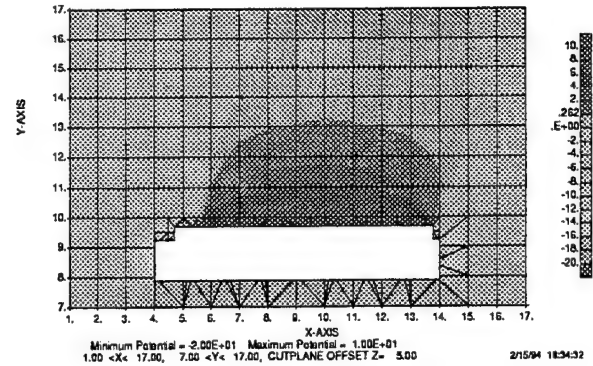

18a

18b

Figure 18. Potential contours in a plane passing through the center of solar arrays 0, 1, and 2 when the ground potential is at +20 V with respect to the plasma. The sheath edge is indicated by the labels.
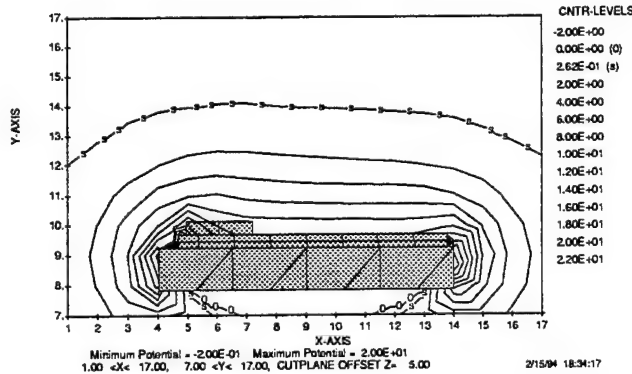
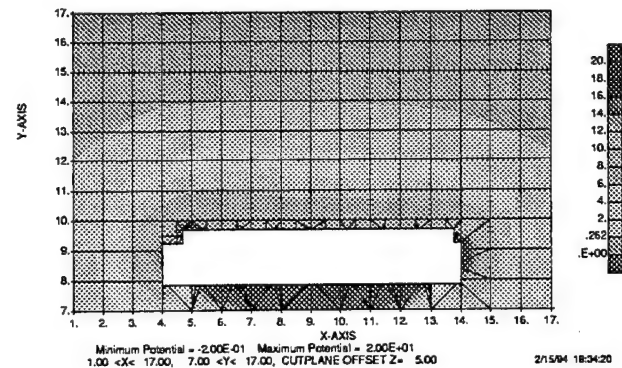When the spacecraft ground is at 0 V with respect to the plasma, the sheath is about 0.2 m thick and is rounded along the sides. The current enhancement due to the sheath is four times. At –20 V, the sides of the sheath are squared off. The sheath provides only a 30% enhancement. At +20 V, the sheath is 0.25 m thick and surrounds the full width of the top panel. However, the portion of the sheath above the solar array surface is flat and current from the rounded sides of the sheath is attracted to the conducting surfaces at the higher potential. The current enhancement is a factor of two. Even for this case, in which the potential applied to the solar array is much higher than the spacecraft ground potential, the results are significantly affected by the spacecraft ground potential.

31

The current to each of the solar array "average surfaces" has been computed for average solar array surface potentials from 2 V to 30 V, spacecraft ground potentials from 0 V to –30 V, and plasma densities from 10^{10} to 10^{12} m^{-3}.

There is another effect that occurs at negative ground potentials that reduces the collected current. Consider the same case discussed above, except examine array 36. Figures 19 a and b show the potential contours in a plane passing through the center of solar array 36 when the ground potential is at 0 V with respect to the plasma. The solar array surface collects 68 μA. This is about five times the plasma thermal current to a surface of this area. Figures 20 a and b show the same case when the ground potential is at –20 V with respect to the plasma. Tracking macroparticles from the sheath gives a current of 3.5 μA, about 25% of the plasma thermal current to a surface of this area. However, not even this much current is collected. An electron at infinity would need to overcome a –1 V potential barrier to reach the "sheath." A barrier of this size attenuates the current by orders of magnitude.
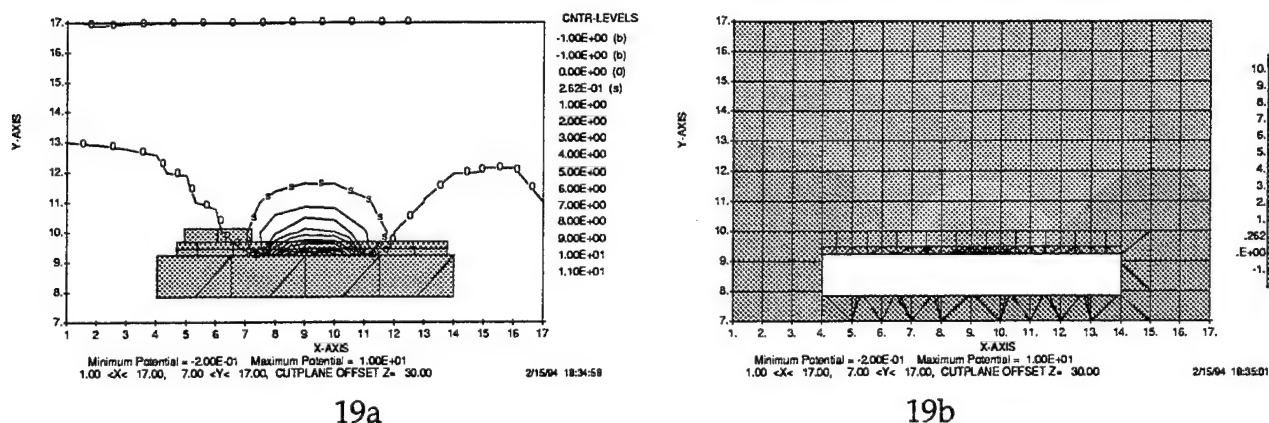

19a

19b

Figure 19. Potential contours in a plane passing through the center of solar array 36 when the ground potential is at 0 V with respect to the plasma. The sheath edge is indicated by the labels.
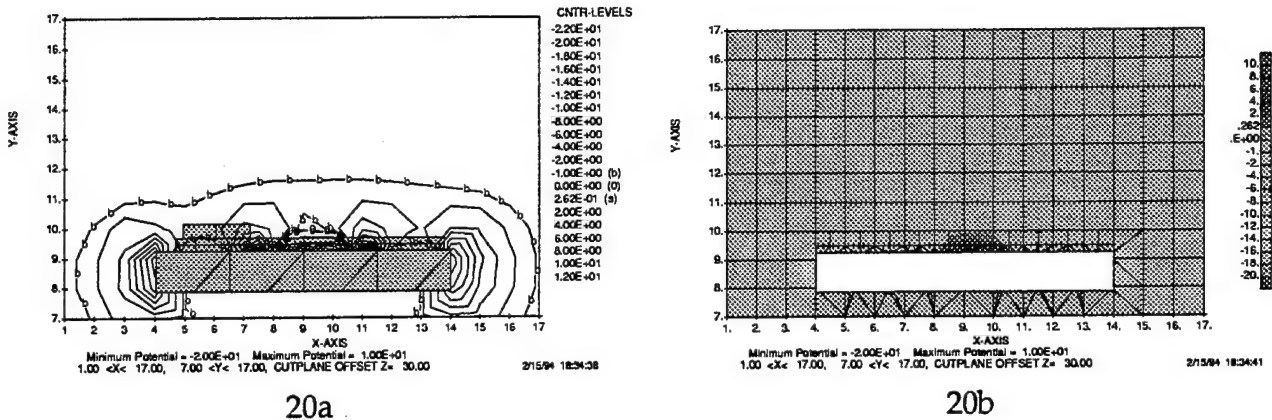
20a

20b

Figure 20. Potential contours in a plane passing through the center of solar array 36 when the ground potential is at –20 V with respect to the plasma. The "sheath" edge is indicated by the labels. The –1 V contour level is indicated by the label b.

3.1   Survey of Parameter Space

Calculations were done for three different plasma densities for the six planar array sets that will be biased. (Solar arrays 1 and 2 are combined and solar arrays 4 and 6 are combined.) All the calculations were done using the NASCAP/LEO computer code. The code computed potentials in space due to the given surface potentials. Then macroparticles were tracked from the sheath edge to determine the current to the solar array.

Figure 21 shows the current collected divided by the current collected at 0 V. Figure 22 shows the same data divided by the plasma thermal current and the solar array area. The solar array area includes the entire insulating and biased conductor area.

Figures 21 and 22 only partially include the reductions in current due to barrier formation. NASCAP/LEO does not create sheath particles in regions of high electric field. For most of these cases, this criterion is adequate to insure that macroparticles are not created at sections of the sheath boundary that cannot be reached by thermal electrons from infinity. Contour plots were examined for a selection of cases with negative potential. The result of the survey is that when a kT barrier exists, NASCAP/LEO computed a current collected value of less than 0.25 the plasma thermal current times the solar array area. However, in most of the cases in which NASCAP/LEO computed currents under 0.25 of the plasma thermal current times the solar array area, some fraction of the sheath was accessible to thermal electrons.

Figures 21 and 22 may be used to estimate the effect of the APEX ground potential on the current collected by the PASP Plus test solar arrays. When the fraction of area collecting is below 0.25, the figures may overestimate the collected current.

That much of the surface of test solar array 36 is covered with a semi-conducting material is not included in these calculations.

Figure 21a. Current collected as a function of ground potential normalized by current collected at 0 V for various arrays for array surface potentials of 2 V, 5 V, 10 V, 20 V, and 30 V, and three plasma densities.
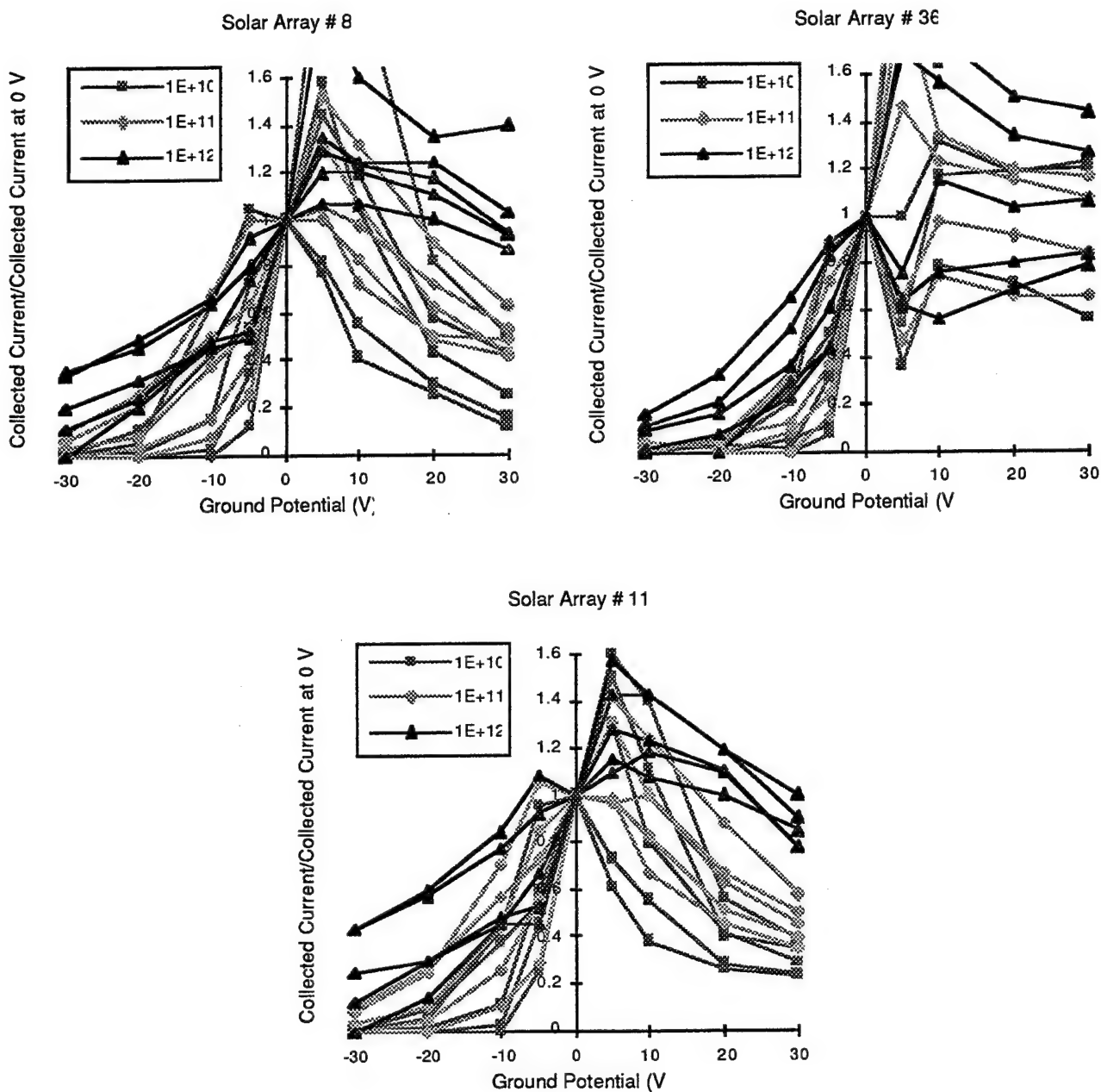
Figure 21b. Current collected as a function of ground potential normalized by current collected at 0 V for various arrays for array surface potentials of 2 V, 5 V, 10 V, 20 V, and 30 V, and three plasma densities.

Solar Array # 1

Solar Array # 4

Solar Array # 3

Figure 22a. Current collected as a function of ground potential normalized by array area for various arrays for array surface potentials of 2 V, 5 V, 10 V, 20 V, and 30 V, and three plasma densities.
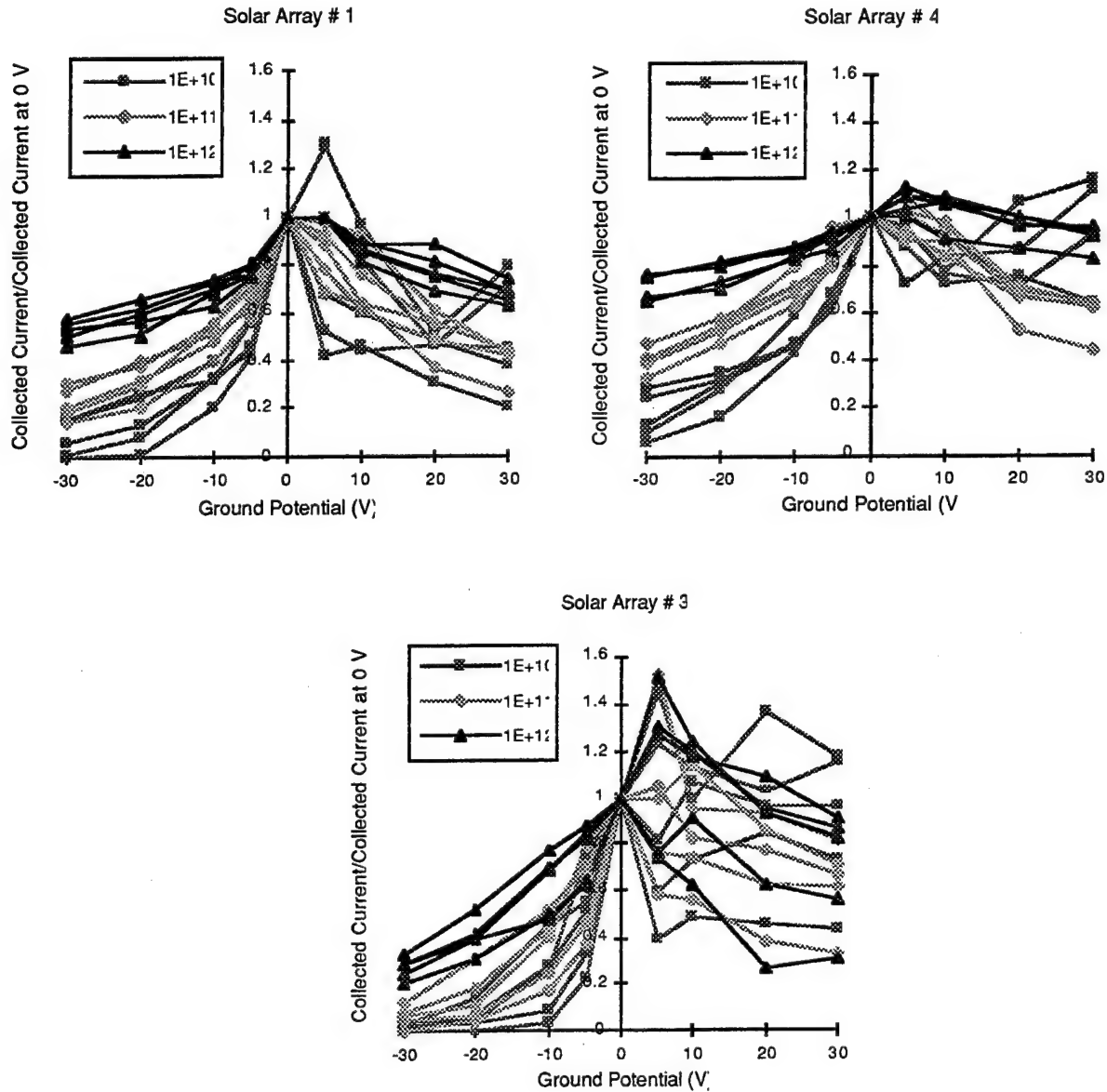
36

Figure 22b. Current collected as a function of ground potential normalized by array area for various arrays for array surface potentials of 2 V, 5 V, 10 V, 20 V, and 30 V, and three plasma densities.

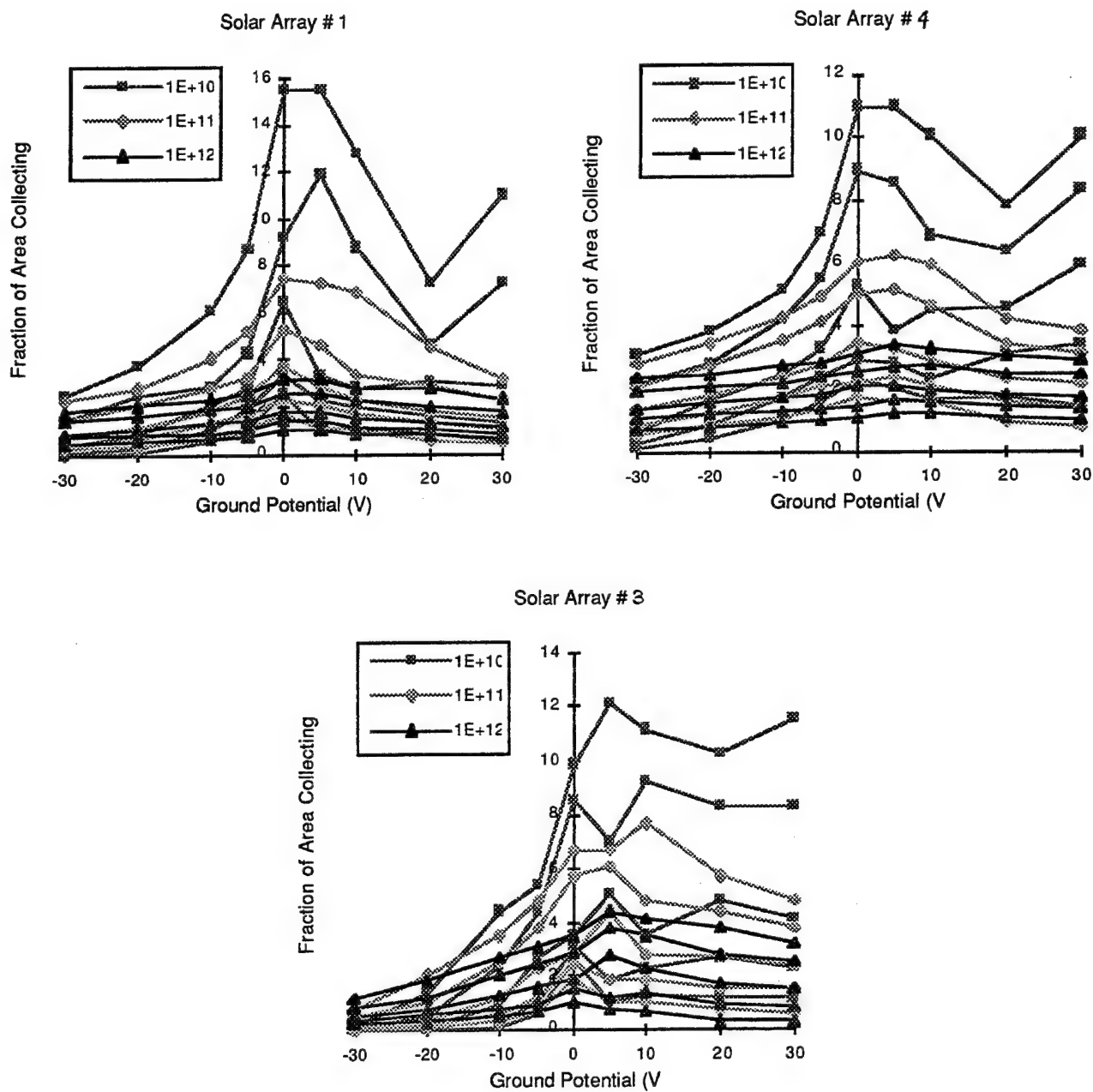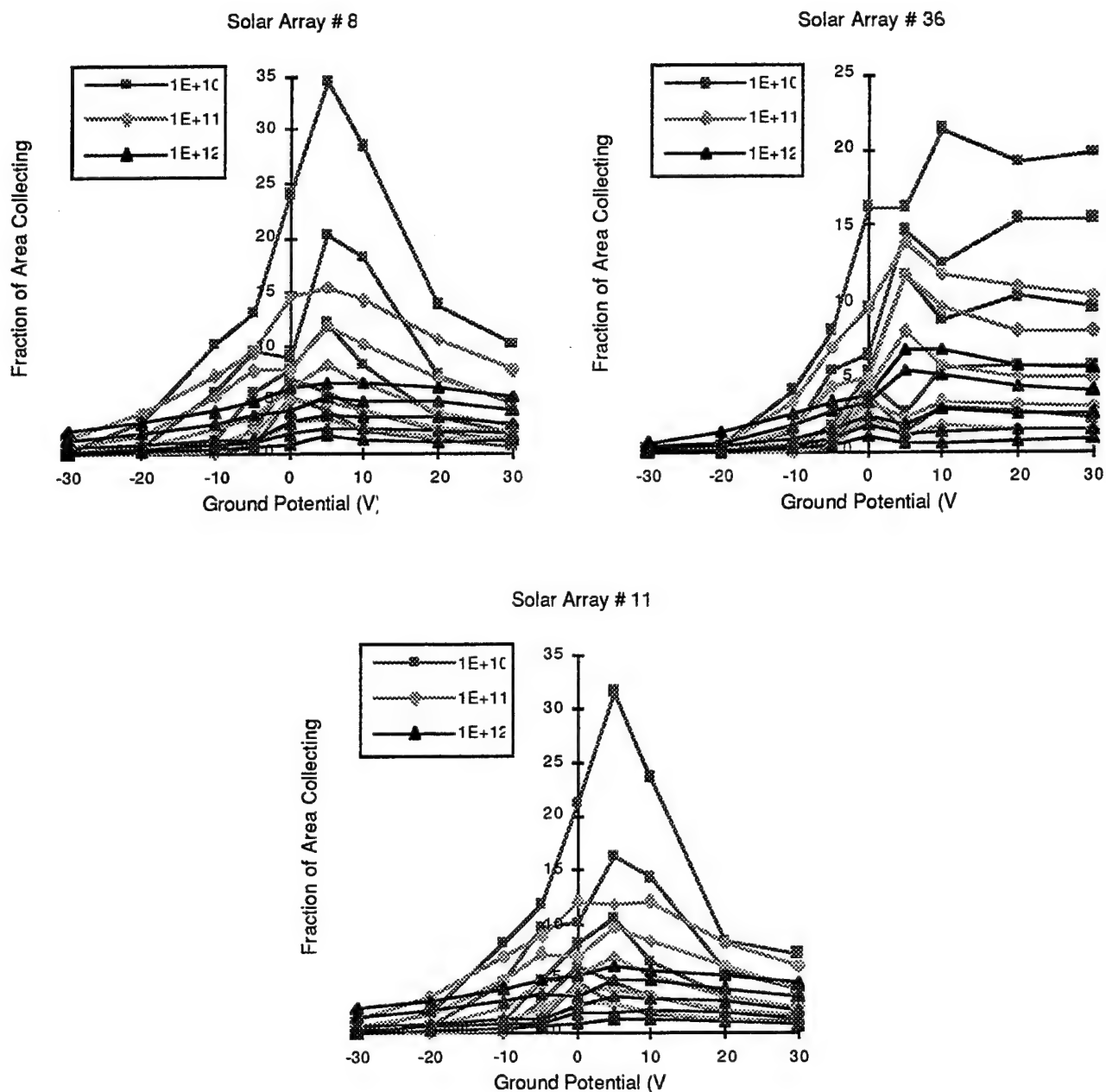# 4.   LANGMUIR PROBE MEASUREMENTS AND MODELS

Insight into the limitations of models and measurements can be gained by comparing them with each other. For this reason, we compared the various Langmuir probe measurements with models we have at our disposal. We looked at two times.

The first time we looked at was the first five and one-half hours of August 8, 1994 GMT (day 94220). We used the orbit parameters for APEX from August 7, 1994. Figure 23 shows the altitude as computed by EPSAT, which uses the orbit generator ORB and as output by the PASP Plus software. The agreement suggests that we are modeling the orbit reasonably closely.

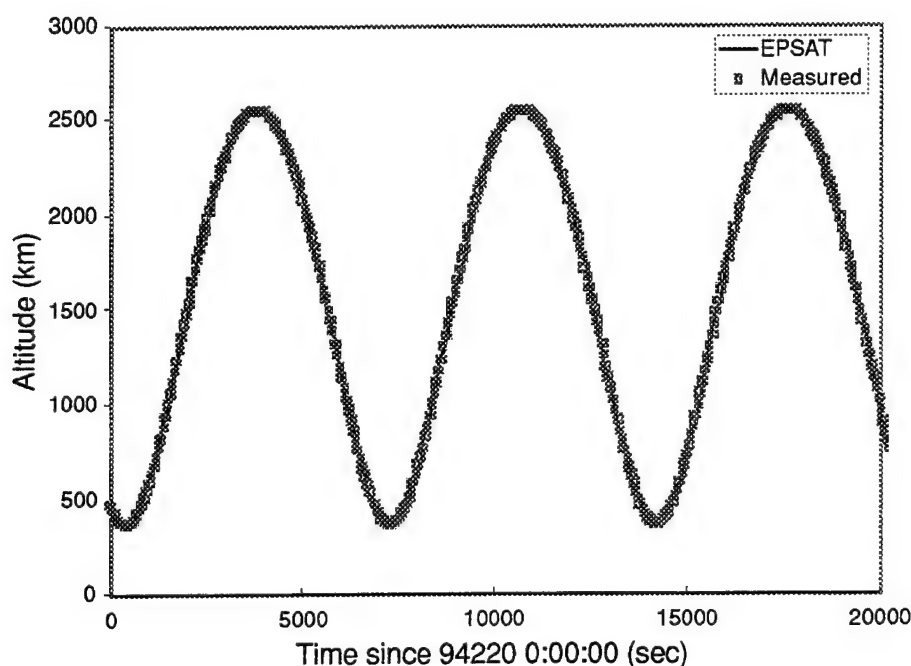Figure 23. Altitude of the APEX spacecraft on August 8, 1994.

Figure 24 shows the angle between the ram direction and the solar array normal. The one degree difference between the extreme values given by EPSAT and the extreme values given by the PASP Plus software is due to several factors. APEX does not follow the sun perfectly. The angle between the sun direction and the solar array normal at the

38

time of the first peak in the ram sun angle is 0.4 degrees. The precession of the orbit is not completely followed correctly by the ORB orbit generator. This accounts for up to 0.5 degrees. There may be other contributions also. The level of agreement does indicate that the orbit model is not following the APEX orbit perfectly.

Figure 24. Attitude of the APEX spacecraft on August 8, 1994.

Figure 25 shows the plasma density as determined from measurements by the Langmuir probe and the plasma density as computed by EPSAT using the IRI-86 model and the ORB orbit generator. Above 1000 km, EPSAT assumes that the plasma density drops in the manner suggested by Al'pert. One of the input parameters to the IRI model is the sunspot number, R12. The EPSAT default sunspot number for this day is 62. The actual sunspot number for this time is 27. The peaks in the plasma density as modeled by IRI are narrower for the lower sunspot number. For both values of the sunspot number, the measured plasma density is lower than the model by a factor of about three. It should be noted that in August, the APEX orbit was such that the low altitudes, high densities occurred while the spacecraft was at the higher latitudes where the IRI model is less accurate.

39

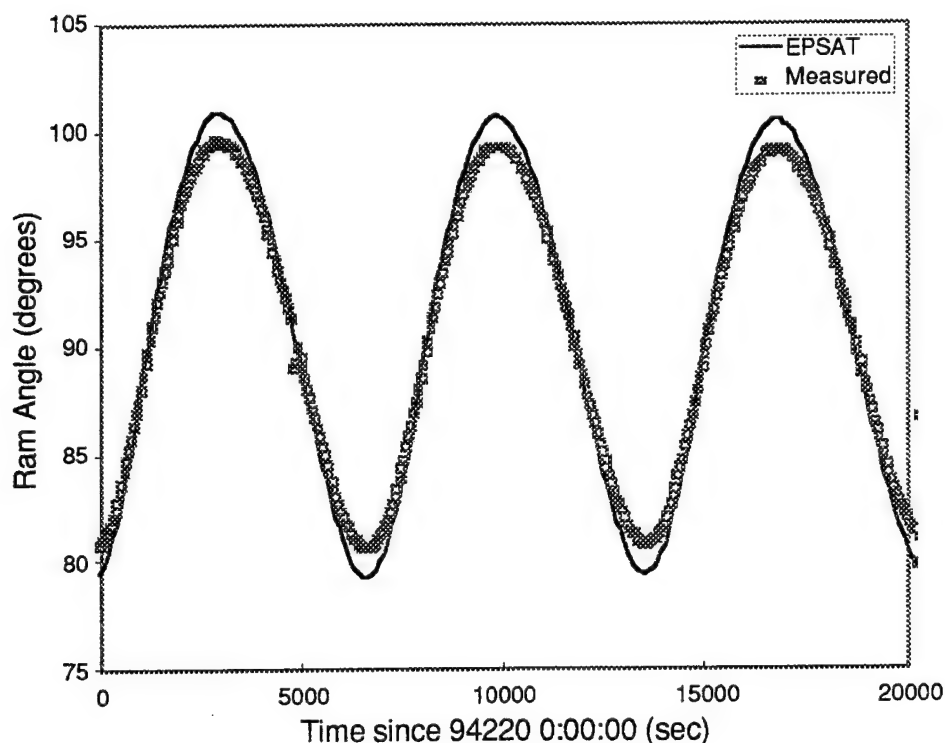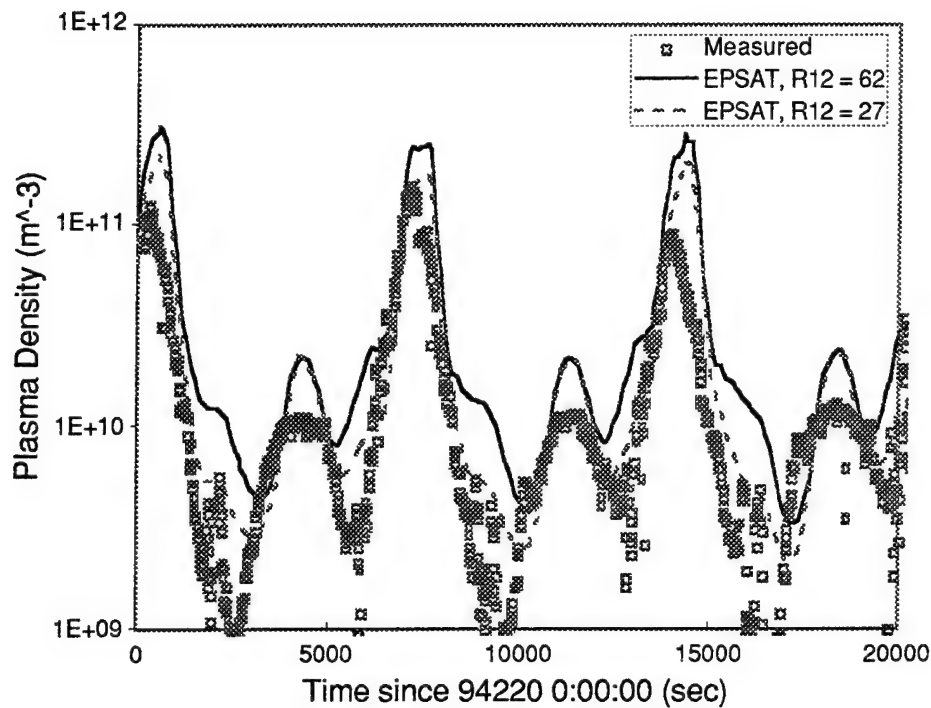Figure 25. Plasma density at the APEX spacecraft on August 8, 1994.

Figure 26 shows the plasma temperature as determined from measurements by the Langmuir probe and the plasma temperature as computed by EPSAT using the IRI-86 model and the ORB orbit generator. The plasma temperature as modeled by IRI does not vary significantly with sunspot number for this case. The model temperature is about 50% below the measured values. From the two plasma measurements, we get that the difference between the model plasma thermal current and the plasma thermal current determined from the measurements is a factor of about 2.5, with the model value higher. The difference between the model debye length and the debye length determined from the measurements is a factor of about 1.4, with the measured value higher.

40
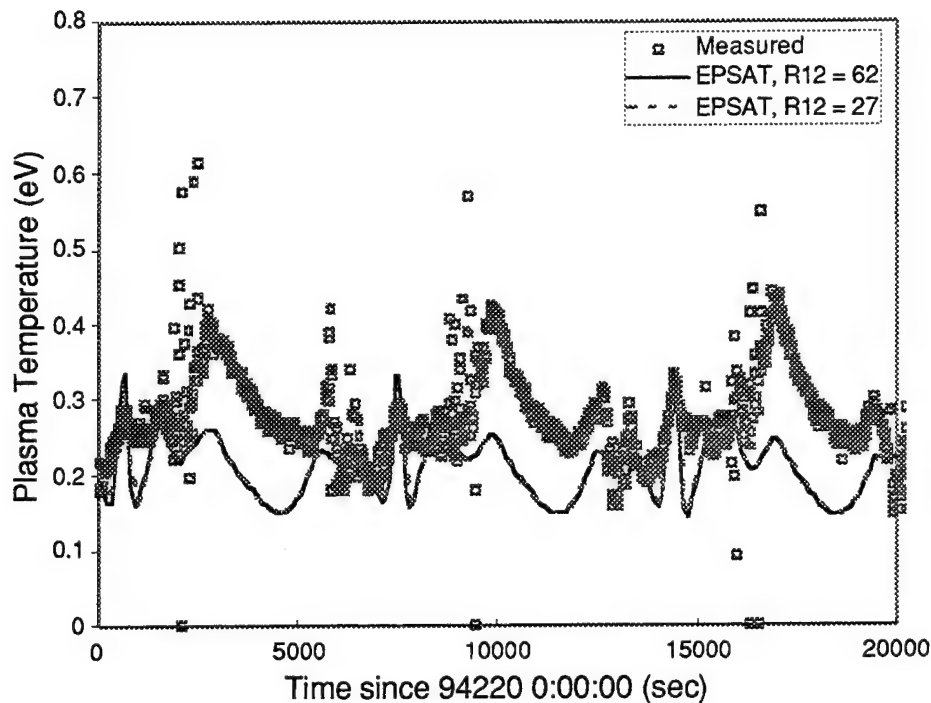
Figure 26. Plasma temperature at the APEX spacecraft on August 8, 1994.

Figure 27 shows the APEX floating potential as determined from measurements by the Langmuir probe (SENPOT) and the APEX floating potential as computed by EPSAT using the model environments above, the model developed under this contract for solar array current collection, and the EPSAT floating potential model as described in the EPSAT documentation. (The EPSAT and EWB floating potential algorithm for this problem are the same.) The floating potential is determined by the balance between the ion current to the spacecraft body and the electron (and ion) current collected by the power solar arrays. The difference in time of the peak floating potential values is due to a difference in the time of the peak plasma density between the model and the measurements and an unknown factor. That the measured and model values are as similar as they are suggests that the solar array model developed for solar cells between 50 and 500 V can be used for some problems with solar cells from 0 to 36 V.

41
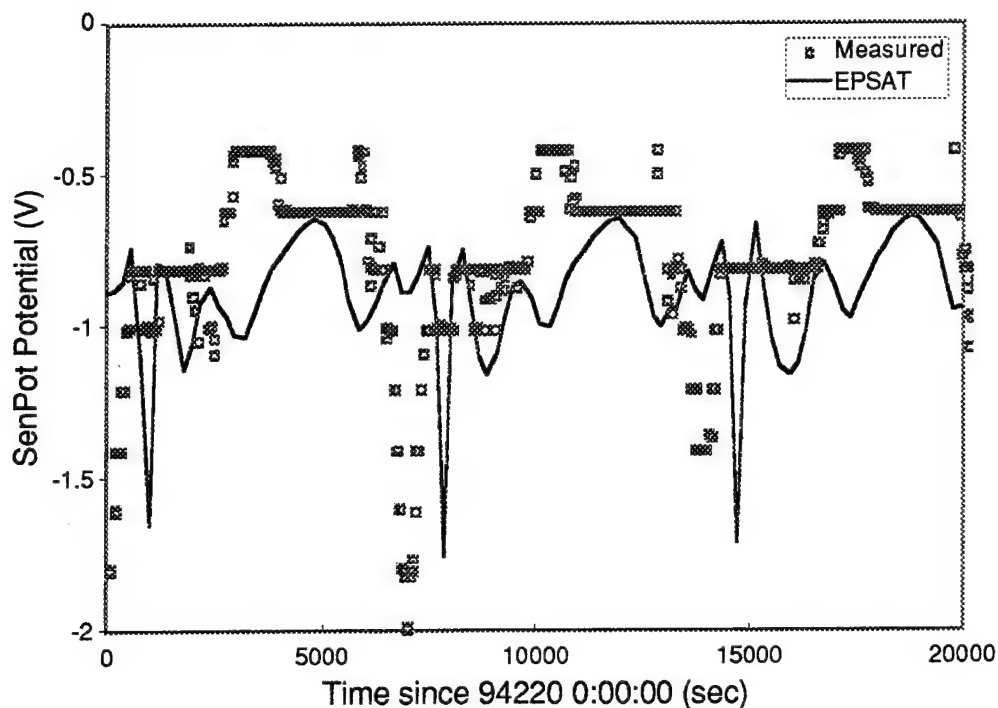
Figure 27. APEX floating potential on August 8, 1994.

We looked at the same quantities for the first five and a half hours of February 12, 1995 GMT (day 95043). We used the orbit parameters for February 9, 1995. We adjusted the mean anomaly by 10 degrees in order to track the altitude correctly. We do not have a good enough understanding of the ORB orbit generator in order to know why this is necessary and if it is appropriate. Figures 28 through 32 are the various quantities computed. There is a difference of 3 degrees between the calculated and measured peak sun-ram angles. This is most likely due to imperfections in tracking the orbit. The model and measured densities agree better than they do for the August date. In early February, the high plasma density portion of the orbit is in the mid-latitudes where the IRI model is most accurate. The model floating potential varies less than the measured floating potential. In the model, the contribution of current through the Z-93 paint helps to balance the electron current collected by the solar arrays. These measurements could be used to extend the solar array model developed under this contract to solar cells at potentials of 0 to 50 V with respect to the plasma. Electrostatic barriers are known to play a role at the lower potentials.

42

Figure 28. Altitude of the APEX spacecraft on February 12, 1995.
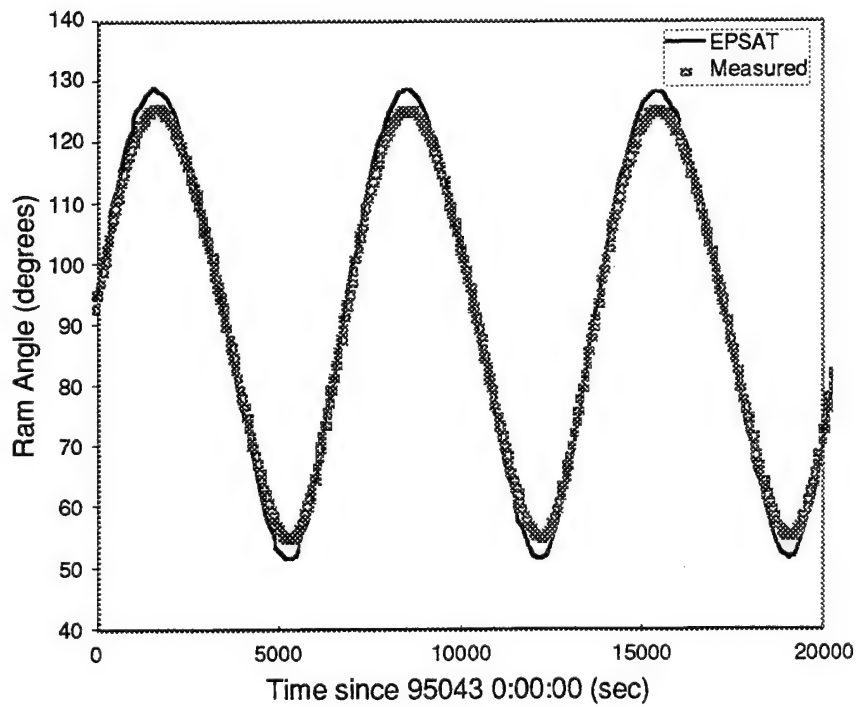
Figure 29. Attitude of the APEX spacecraft on February 12, 1995.

43
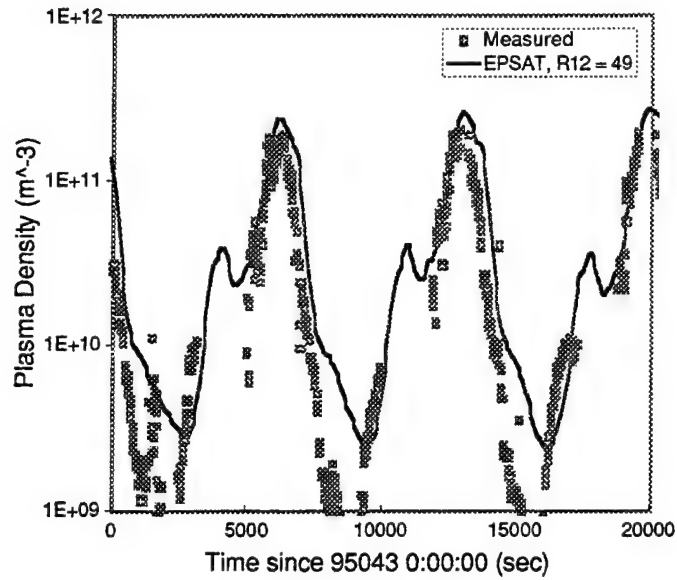
Figure 30. Plasma density at the APEX spacecraft on February 12, 1995.

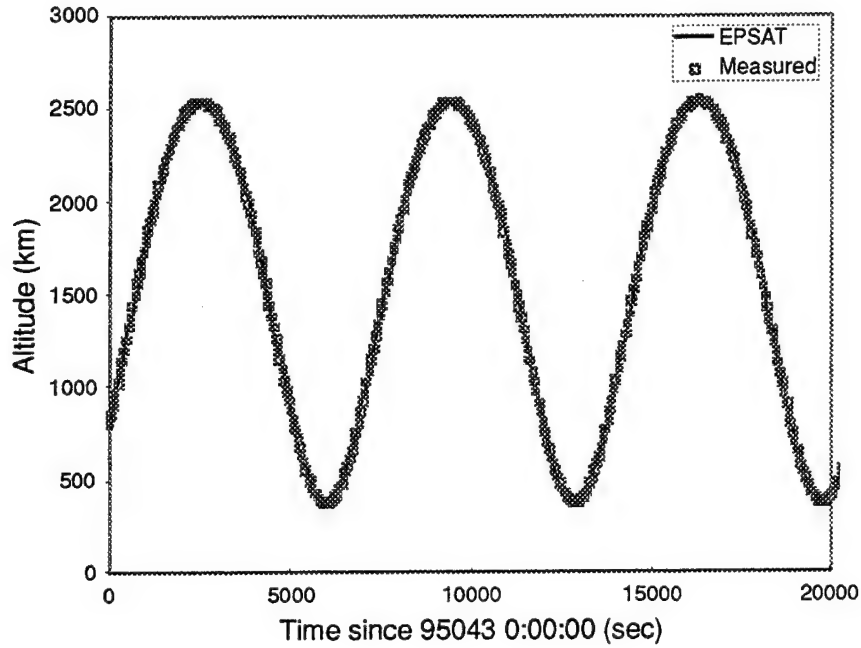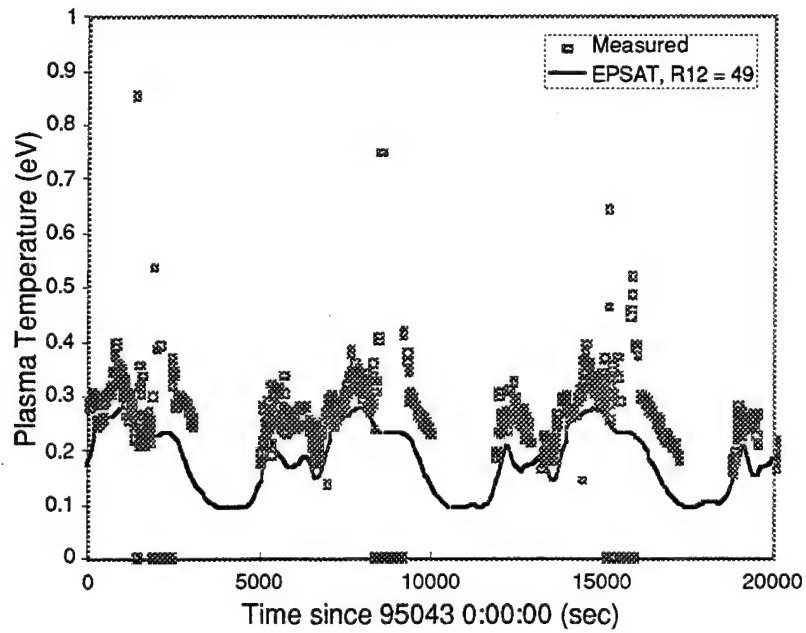
Figure 31 Plasma temperature at the APEX spacecraft on February 12, 1995.

44
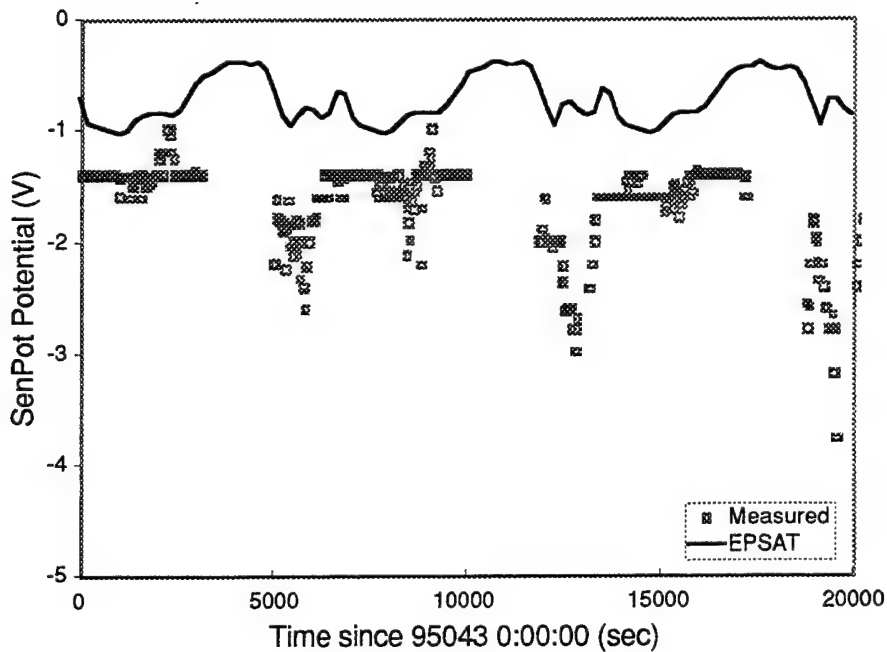
Figure 32. APEX floating potential on February 12, 1995.

4.1 Accuracy of PASP Plus Langmuir Probe

Densities of the order of 10^9 in sunlight cannot be measured properly as the photoelectrons dominate. Densities greater than 3×10^{11} also present problems and are unavailable.

We examined the density measurements on a sample day. The ratio of density measurements made 1 second apart varied from 0.108 to 6.07 with 93% between 0.8 and 1.25. The ratio of density measurements made 29 seconds apart varied from 0.074 to 8.9 with 91% between 0.8 and 1.25. The ratio of temperature measurements made 1 second apart varied from 0.297 to 3.132 with 99% between 0.8 and 1.25. The ratio of temperature measurements made 29 seconds apart varied from 0.33 to 2.45 with 96% between 0.8 and 1.25.

The ratio of the sizes of the spacecraft body and the probe is such that a few volts on the probe is enough to shift the spacecraft ground potential. Figure 33 shows the probe potential with respect to plasma ground as a function of the probe bias. It is linear up to

about 4 V with respect to plasma ground. This figure was made for midnight at the start of day 220 in 1994. The plasma density is about 10^{11} m^{-3} and the electron temperature is 0.1 eV. Figure 34 compares the current collected by the probe as a function of the applied bias with the current as a function of the probe potential with respect to the plasma. As long as the zero potential offset is included in the interpretation, voltage sweeps under 4 V with respect to the plasma should give reasonable results.
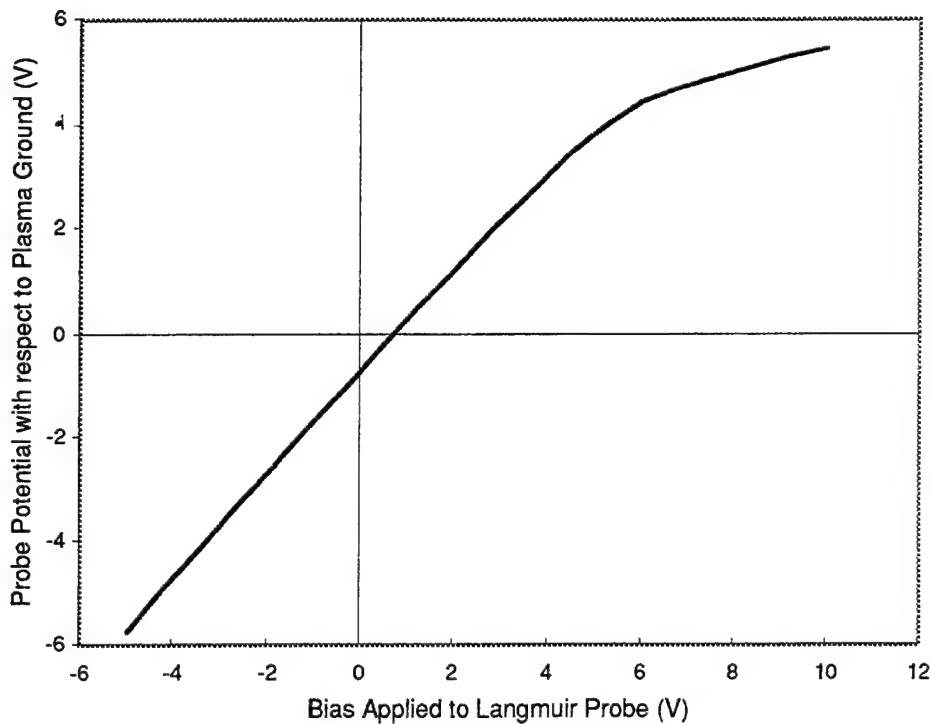
Figure 33. Probe potential with respect to plasma ground as a function of the probe bias. Figure is for the conditions at midnight at the start of day 220 in 1994. The plasma density is about 10^{11} m^{-3} and the electron temperature is 0.1 eV.

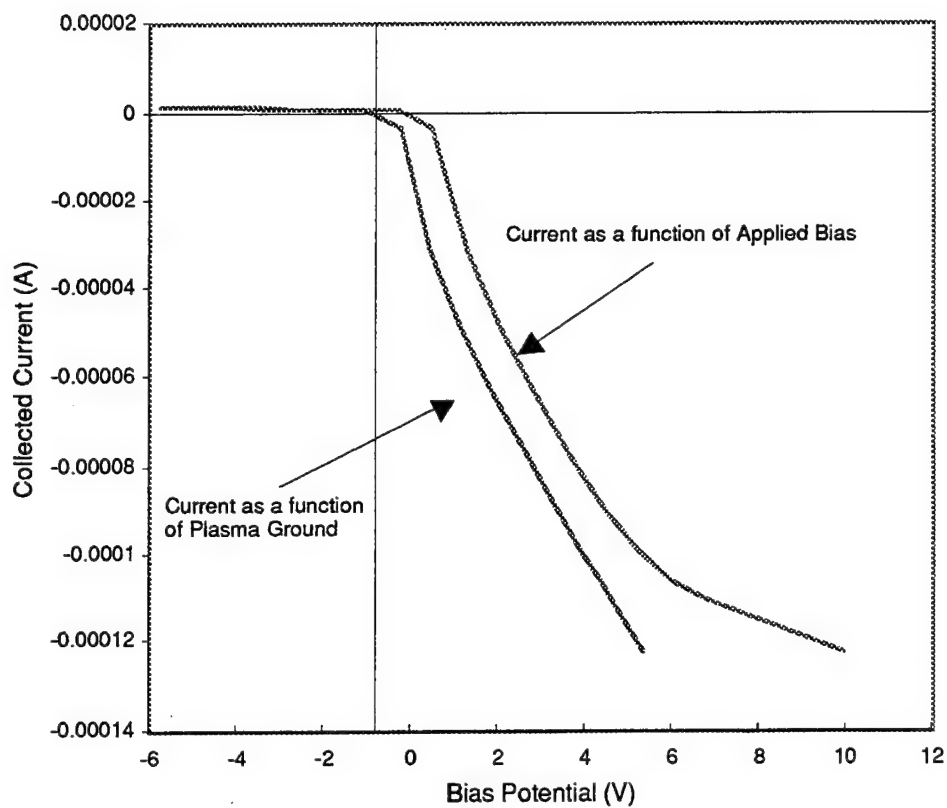Figure 34. Collected current as a function of the probe bias. Figure is for the conditions at midnight at the start of day 220 in 1994. The plasma density is about 10^{11} m^{-3} and the electron temperature is 0.1 eV. ·

5. CURRENT COLLECTION AS A FUNCTION OF BIAS AND PLASMA DENSITY

We examined the measured collected current as a function of the applied bias, plasma density, and temperature for the first seven months of PASP Plus data collection. We focused on measurements made in the ram and with the emitter off. We expect that the wake measurements depend on the attitude of APEX. Generally, when the emitter is on, the APEX floating potential is positive and the algorithm for the determination of the plasma density and temperature does not work.

Wake measurements and emitter on measurements should be examined at some time in the future.

Leakage current is measured as part of a 30 second sequence of measurements. During each 30 second sequence there are two Langmuir probe sweeps (one up and one down) with the applied bias at zero, and then 23 measurements of the leakage current with the applied bias at a constant. In order to obtain a single current collected, plasma density, and plasma temperature for each 30 second sequence, the following procedure was used. The current collected is the twenty-second current measurement. The plasma density is the plasma density measurement that follows the current measurement sequence. The plasma temperature is the one made at the same time as the density measurement. Current measurements for which the plasma parameters are unavailable were ignored. Alternative schemes were tried.

In order to plot the leakage current, we averaged the data obtained over the nine months. For each 30 second sequence, a collecting area was calculated.

$$\text{Collecting Area}\left(m^{-2}\right) = \frac{\text{Leakage Current (A)}}{2.68 \times 10^{-14} \text{ Density}\left(m^{-3}\right)\sqrt{\text{Temperature (eV)}}} \tag{10}$$

The measurements were sorted into bins by plasma density, plasma temperature, and applied bias. The plasma density bins are each a half decade per bin and are labeled by the density at the geometric center of the bin. Only measurements from 1.78×10^9 m^{-3} to 5.62×10^{11} m^{-3} were included. Lower density measurements are excluded because photoemission may play a role. Higher density measurements are excluded because the

48

density measurement is unavailable. The probe is unable to properly measure the high current. The plasma temperature bins are 0.1 eV in width and are labeled by the temperature at the center of the bin. Almost all of the measurements are between 0.05 eV and 0.35 eV. There are 23 logarithmetically spaced applied bias bins labeled by the bias at the center of the bin. The bins are the following: 49.4, 54.6, 60.3, 66.7, 73.7, 81.5, 90.0, 99.5, 110, 122, 134, 148, 164, 181, 200, 221, 245, 270, 299, 330, 365, 403, 446, and 493 V.

For each plasma density, plasma temperature, and applied bias bin, the average collecting area for the seven month period was computed. As the plasma conditions and applied bias are correlated with the time on orbit, attitude, and location within the orbit, unknown and unaccounted for systematic factors may influence these measurements.

Plots of the collecting area as a function of applied bias, plasma density, and plasma temperature appear in Figures 35-42.

Several features of interest are clear on inspection of the figures.

Overall, the collecting area rises about two orders of magnitude as the applied bias rises one order of magnitude. This is typical of leakage current when snapover plays a role in the current collection process. Arrays #1 and #2, the conventional interconnect design, do not rise as quickly, particularly at the high bias end. This may be because the collected current is high enough that the APEX floating potential goes negative in order to collect enough ions to balance the electron current collected by the biased test array. The APEX floating potential and current collection characteristics are discussed in Chapter 7.

As expected, the current collection characteristic of array #5, APSA, is different from all of the other arrays. Array #5 is discussed in Chapter 11.

In general, the collected current is several times the array area. Table 1 gives the array and panel areas for the various test solar arrays.

Table 1. Solar-Cell Areas and Array Panel Areas for the PASP Plus Planar Arrays.

Array	Array Area (m^2)	Panel Area (m^2)
# 1	0.016	0.129
# 2	0.048	0.129
# 3	0.026	0.078
# 4	0.032	0.129
# 5	0.015	0.059
# 6	0.019	0.129
#8	0.0064	0.029
# 11	0.013	0.029

There is a minimum collecting area for each plasma density that is the same for all of the arrays. The smallest measured PASP Plus leakage current value is 0.2 μA. Collecting areas near and below this value should be ignored. Table 2 relates the minimum leakage current to collecting area.

Table 2. Collecting Area in m^2 at Minimum Leakage Current

| Plasma Density (m^{-3}) | Plasma Temperature (eV) | | |
| | 0.1 | 0.2 | 0.3 |
	Collecting Area (m^2)		
3×10^9	0.0075	0.0053	0.0043
1×10^{10}	0.0024	0.0017	0.0014
3×10^{10}	0.0007	0.0005	0.0004
1×10^{11}	0.0002	0.0002	0.0001
3×10^{11}	0.0001	0.0001	0.0000

The collecting area does not depend strongly on the plasma density and temperature. The collecting area is larger for lower densities (longer debye lengths). The dependence on density is stronger for lower densities.

There is a large amount of scatter in the graphs. When the several measurements in the same bin are compared, variations of a factor of ten are common. Chapter 9 will address this issue.

Figure 35. PASP Plus Array #1 collecting area as a function of cell bias.

Figure 36. PASP Plus Array #2 collecting area as a function of cell bias.

Figure 37. PASP Plus Array #3 collecting area as a function of cell bias.

Figure 38. PASP Plus Array #4 collecting area as a function of cell bias.

PASP Plus Array #5, Ram, Emitter Off, Day 94215 to 95120

Temperature (All)eV   Angle (All)

Figure 39. PASP Plus Array #5 collecting area as a function of cell bias.

PASP Plus Array #6, Ram, Emitter Off, Day 94215 to 95120

Temperature (All)eV   Angle (All)

Figure 40. PASP Plus Array #6 collecting area as a function of cell bias.

54

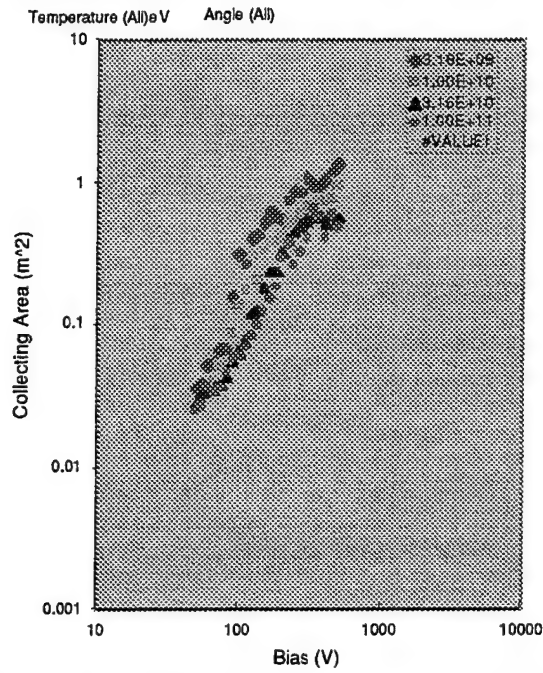PASP Plus Array #8, Ram, Emitter Off, Day 94215 to 95120

Figure 41. PASP Plus Array #8 collecting area as a function of cell bias.

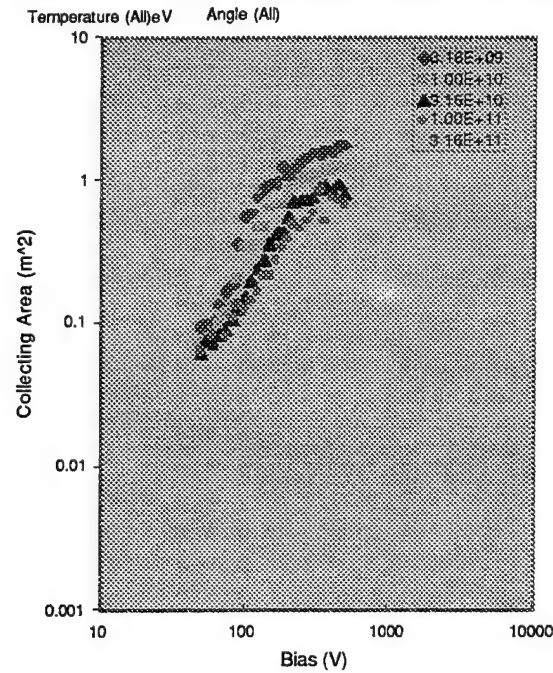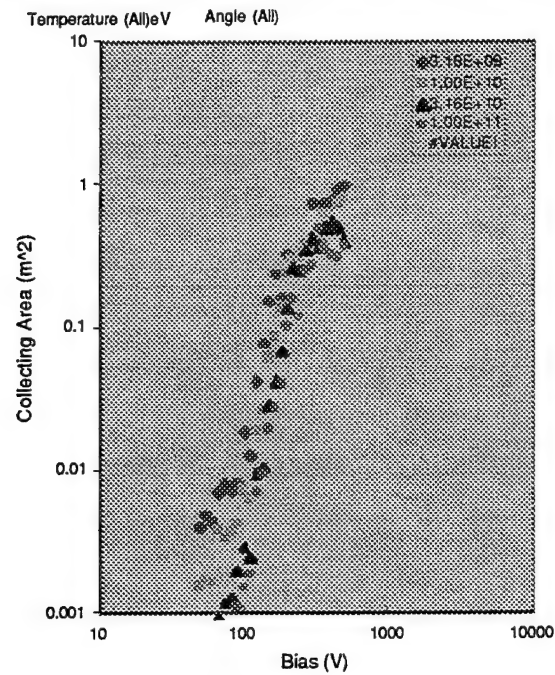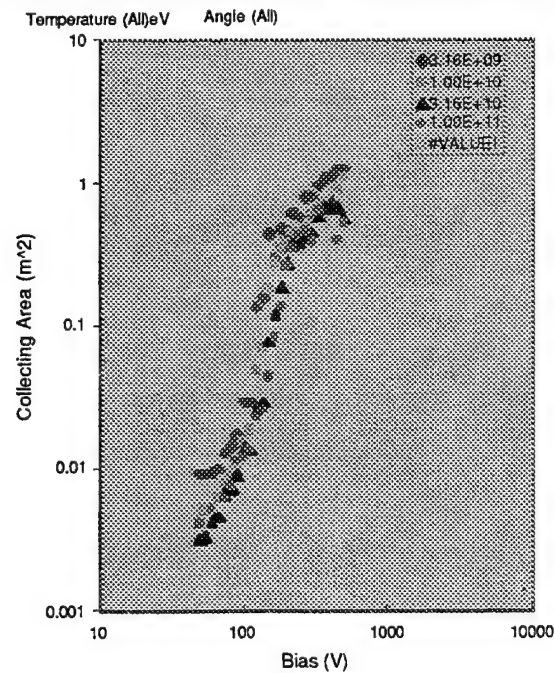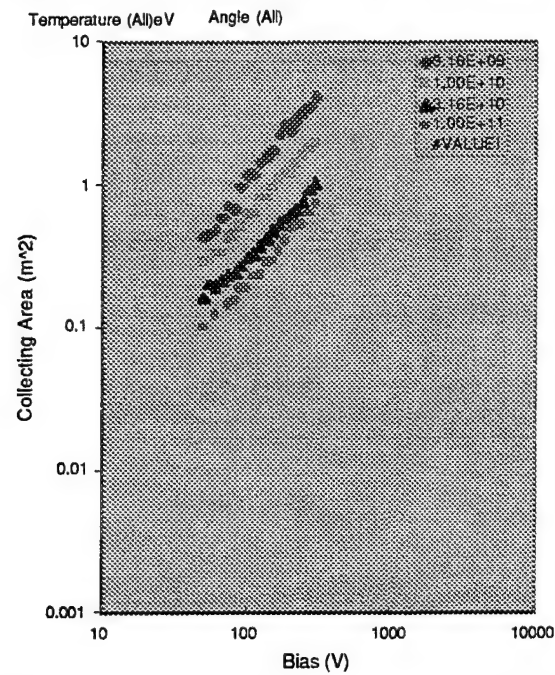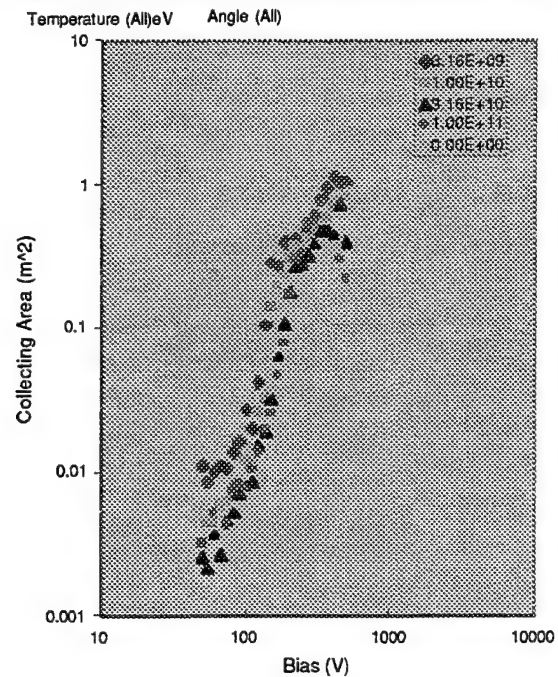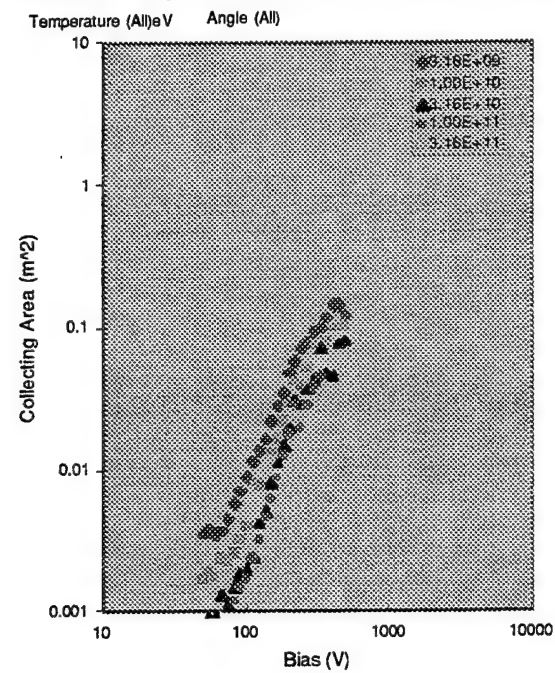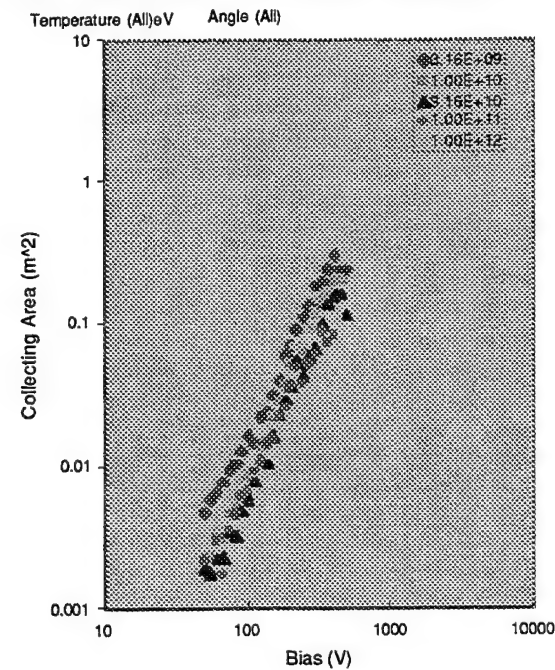PASP Plus Array #11, Ram, Emitter Off, Day 94215 to 95120

Figure 42. PASP Plus Array #11 collecting area as a function of cell bias.

6. VARIATION WITHIN A MEASUREMENT

Each leakage current measurement consists of 23 measurements taken approximately one per second. In general, the 23 measurements vary.

APEX moves fast enough that its plasma environment can vary during the 30 second sequence of a single measurement. This variation is accounted for by averaging the plasma properties before and after the sequence of leakage current measurements. Throughout the orbit, the density varies from low to high as often as from high to low. However, we are only examining ram measurements. This introduces an unintended bias in one direction or the other. The following example illustrates how the bias is introduced. Most of the measurements were taken within 20 minutes of perigee. Sometimes the solar arrays are in the wake during the first 15 minutes of data taking. During the 40 minute period of data taking, the density goes from high to low more than from low to high. The reverse happens when the wake period is at the end of the data taking period. This variation with epoch has not been systematically controlled. A similar bias was introduced by the early practice of making measurements on the arrays consecutively. As a result, measurements on a given array at a given applied bias were made predominately at two or three well-separated points in the orbit. Fortunately, the variation in collecting area due to changes in the environment is generally under a few percent.

Differential charging causes a systematic variation in leakage current. Differential charging can occur through the thickness of the test solar cells, through the thickness of the Z-93 paint, and through any annodization or other layer on the surface of the APEX spacecraft. Since APEX is advertised to be completely covered with conducting surfaces (mostly thermal blankets with the conducting side out), this last effect is ignored here. Figure 43 a illustrates the edge of a solar cell covered by a coverglass and supported by an insulating backing immediately after a bias is applied to the cell. Before the plasma has a chance to respond, the solar cell coverglass and the insulating backing are at the same potential as the solar cell. The electrons in the plasma are attracted to the positive potential cover glass. They deposit their charge on the surface of the cover glass until the surface of the cover glass has a negative potential of a couple of times the plasma temperature. Figure 43 b shows the equilibrium situation. This process is differential charging.
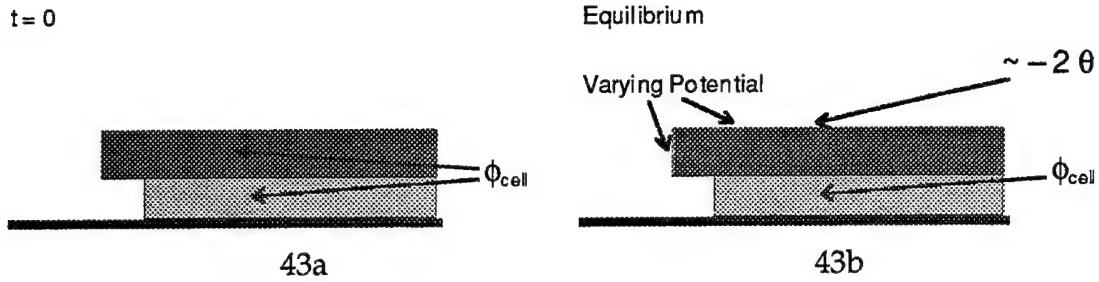
Figure 43. Differential charging across solar cell cover glass.

The incident electrons create secondary electrons. Some remain at their creation location developing a differential potential. Some travel across the surface toward the higher potential. Some of these are ultimately collected by the solar cell. These show up as an enhanced leakage current until the equilibrium situation is reached. Those electrons collected as leakage current do not reduce the potential on the cover glass surface.

The time scale over which differential charging takes place depends on the incoming current, j_{th}, the dielectric constant, κ, and the thickness of the cover glass, Δ, as well as the initial and final surface potentials.

$$\tau = \frac{(\phi_{cell} + 2\theta)\,\kappa\,\varepsilon_0}{\Delta\,(j_{th} - j_{collected})} \tag{11}$$

In order to obtain an estimate of the time scale, we ignore the temperature and collected current terms. For glasses, the dielectric constant is three or higher. Arrays 4 and 6 have 3.5 mil thick coverglass. Figure 44 shows the time to decay from 100 V as a function of the density. At $10^{10}\ \text{m}^{-3}$, the time to decay from 100 V is one-third of a second. Since the leakage current does not contribute to reducing the surface current, the actual time to decay is longer.
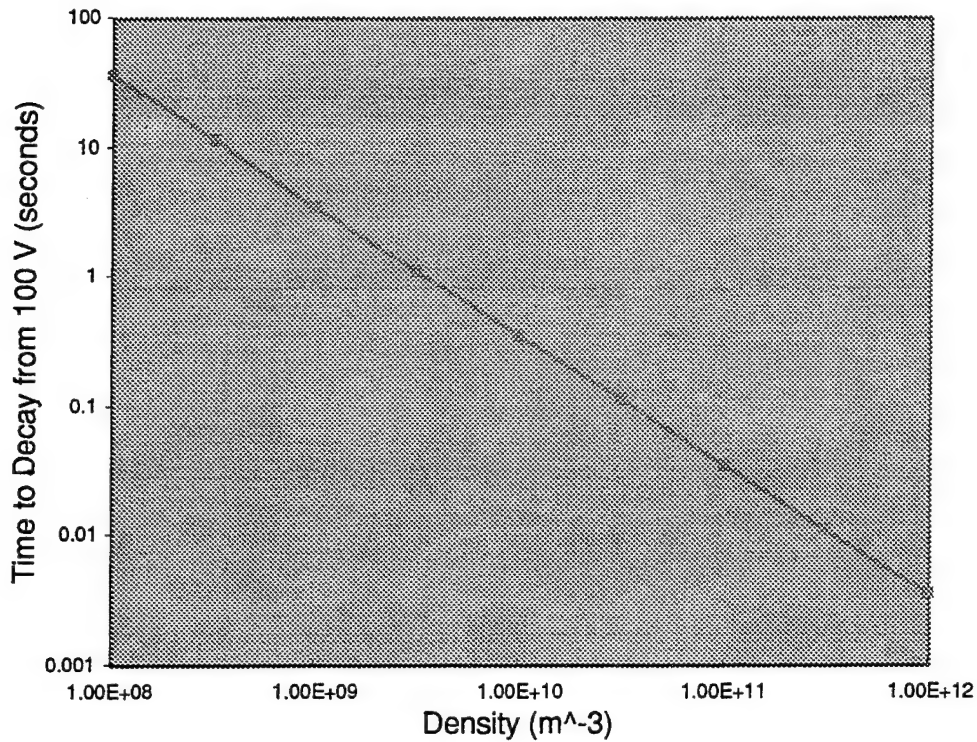
Figure 44. Time to decay from 100 V for array 4 cover glass.

Several people have noticed that sometimes the leakage current appears to decay over a time period of seconds. The array 4 portion of the data set described in Chapter 5 was examined for systematic variations. In order to examine the relative variation, we normalized the current measurements.

$$\text{Ratio}_i^j = \frac{I_i^j}{\displaystyle\sum_{n=2\text{ to }22} I_n^j} \tag{12}$$

The i index refers to the 23 consecutive current measurements. The j index refers to the 30 second measurement sequence. Figure 45 shows ratio averaged over all j values for each density as a function of i.

Average Value of Ratio at each Density
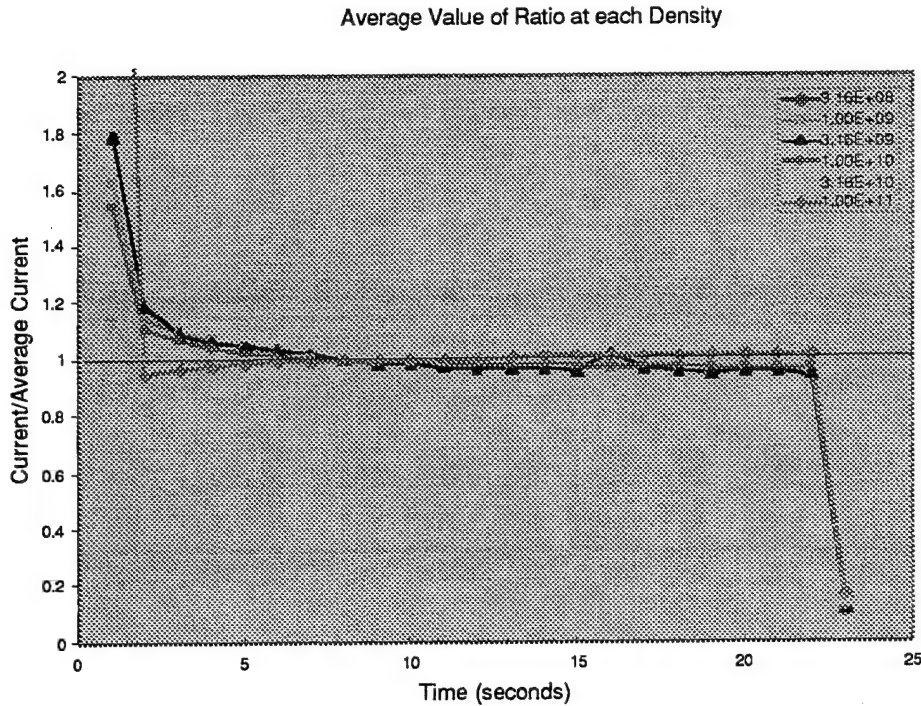
Figure 45. Average time variation of array 4 leakage current for various plasma densities.

The 23rd measurement is systematically approximately one-fifth the average. The reason for this is unknown.

The high value at 1 second of the 10^{11} line is due to one anomalous measurement.

Figure 46 shows the fifth maximum ratio for each density value as a function of i. The fifth maximum is used rather than the maximum as the maximum is dominated by anomalous measurements. This figure illustrates how high above the average the current measurements are. In general, the higher density measurements vary less from the average.
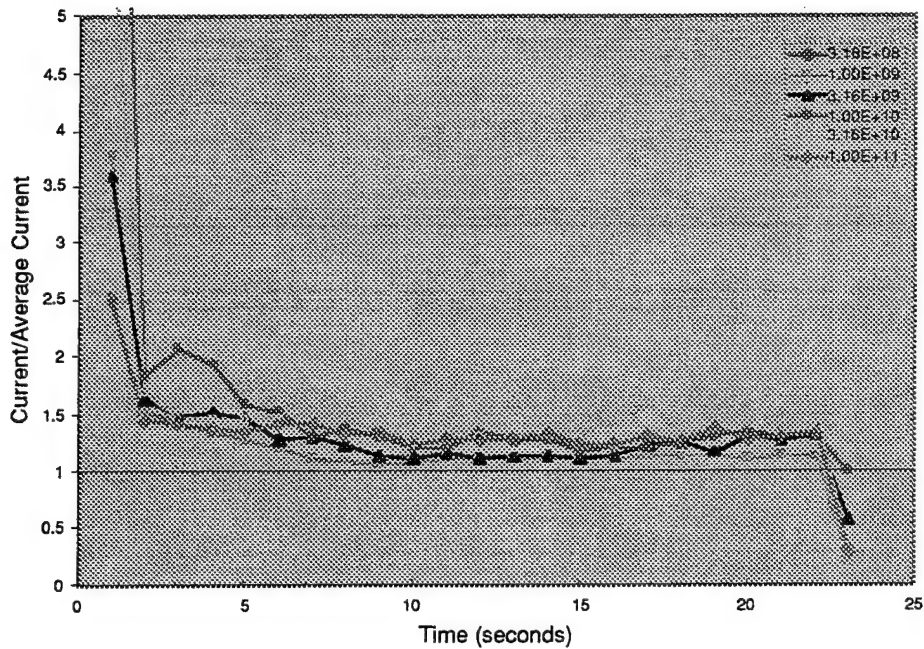
Figure 46. Maximal time variation of array 4 leakage current for various plasma densities.

Figures 44 through 46 are examinations of the entire data set at once and show little about how the current measured during a specific 30 second sequence behaves. Figures 47 and 48 show the time variation for ten specific sequences each. The sequences chosen are the ten at the specified density for which $ratio_2^j$ is largest.

60
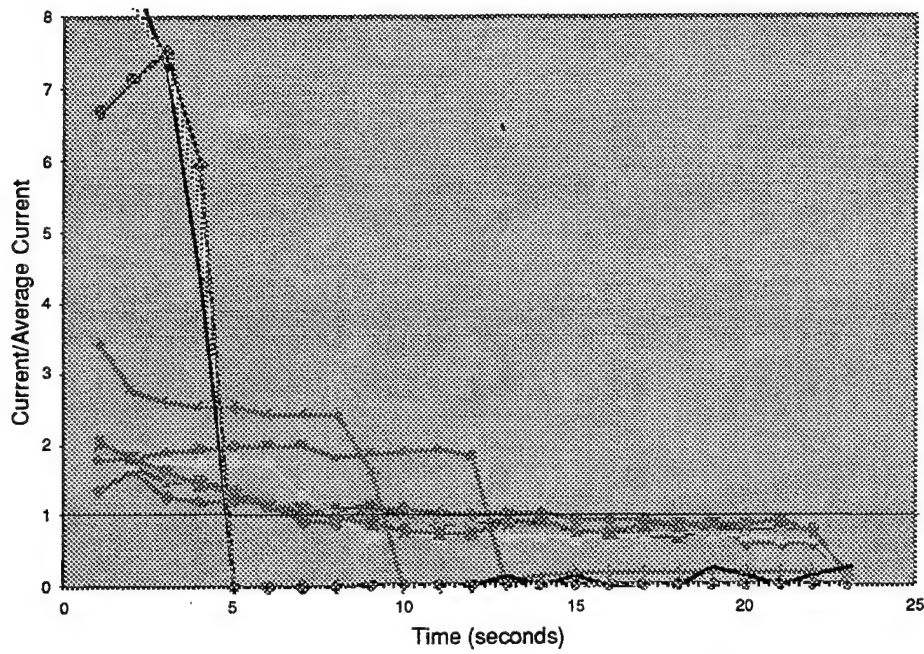
Figure 47. Time variation of array 4 leakage current at 10^{10} m^{-3} for the ten sequences with the highest value of ratio at 2 seconds.

Value of Ratio for 10^11 Plasma Density
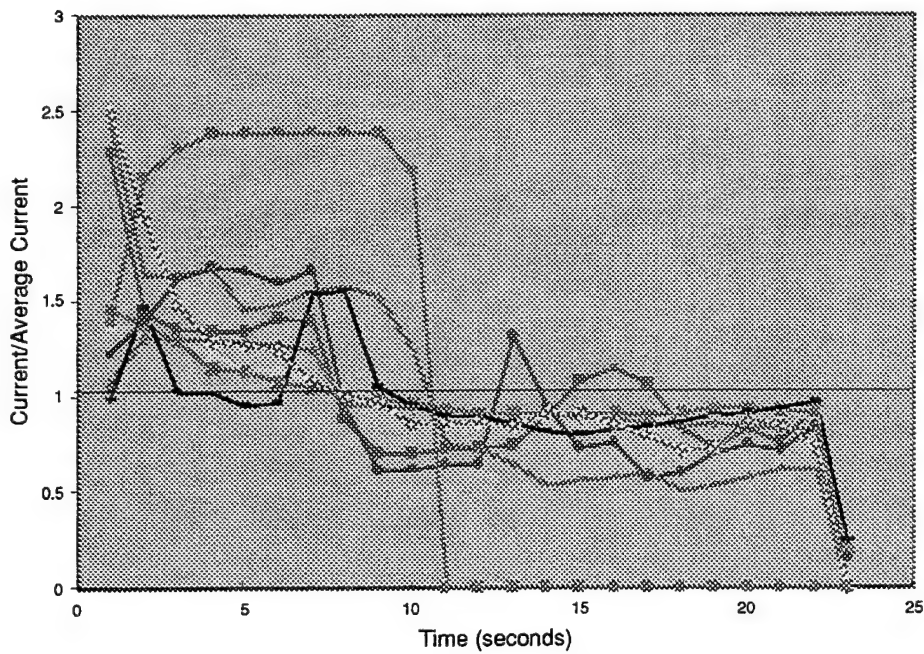
Figure 48. Time variation of array 4 leakage current at 10^{11} m^{-3} for the ten sequences with the highest value of ratio at 2 seconds.

61

The variation in current seen in figures 47 and 48 has several sources. Sometimes the current is steady for a period and then suddenly drops. This could indicate that the measurement process is not working properly, that something has happened in the environment, or that fully developed snapover has suddenly disappeared. In some cases there is a single point that appears out of line with the rest of the measurements. This would suggest that the specific measurement is invalid.

At both densities, there is a decrease in current on a time scale on the order of 30 seconds. This does not occur in the average or maximum plots. This effect must occur only some of the time. One explanation would be that in these particular cases, the plasma density is decreasing during the measurement period. However, for the ten cases at the higher density, only six of them are during a period of decreasing plasma density.

At 10^{10} m^{-3}, there is a decrease in current on a time scale of a few seconds. This is consistent with differential charging across the cover glass.

7. APEX CURRENT COLLECTION CHARACTERISTICS AND FLOATING POTENTIAL

Previously we investigated the ion collection capability of APEX using the NASCAP/LEO computer code (SSS-DPR-94-14662). The current collection characteristics can be approximated by those of a sphere with a 0.45 m radius.

The capacitance and conductivity of the Z-93 paint on the backs of the solar array panels and on the faces of the test panels were not included in the previous assessment of the APEX current collection. We are presently proceeding under the assumption that these effects are small.

The ion current to a sphere varies as a function of the sphere velocity and the ion composition of the plasma. These effects are included in calculations done by the EPSAT computer code. For the APEX orbit, these effects are small.

Figure 49 shows the ion current collected by a negatively biased 0.45 m radius sphere with the velocity of APEX on Day 220 of 1994 at 00:16:40 GMT and a strictly oxygen plasma. The current is normalized by the electron plasma thermal current to give an equivalent electron collecting area. This figure can be directly compared with those in Chapter 5.

APEX, EPSAT Calculation
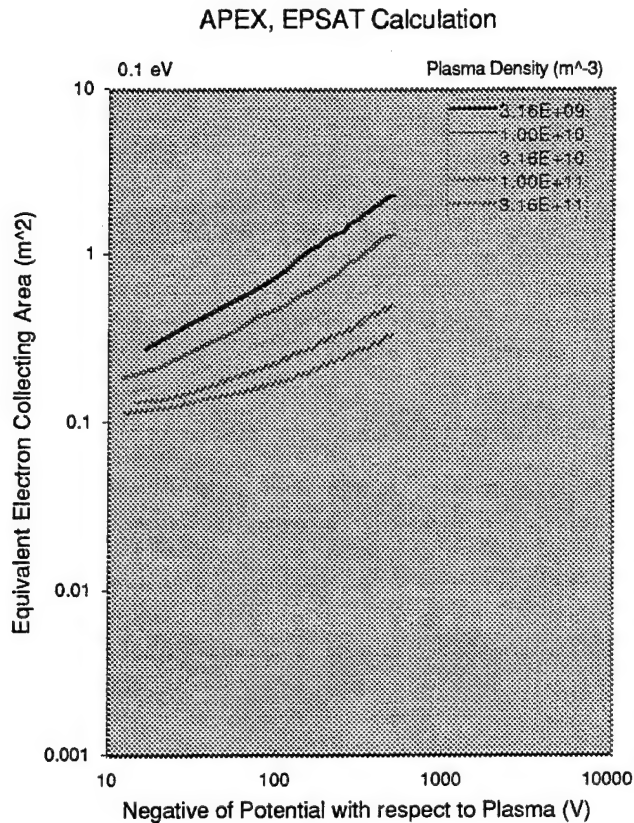
Figure 49. Equivalent electron collecting area as a function of APEX potential with respect to the plasma.

At lower densities, the spacecraft potential has a larger range and therefore a larger collection area.

A comparison of Figure 49 with the figures in Chapter 5 suggests that APEX is often at a large negative potential with respect to the plasma. For many of the arrays, the collecting area at 300 V is near 1 square meter. To get an equivalent ion current requires a couple of hundred volts negative even for the lower densities. The ESAs do not measure this much negative charging.

Other sources of current that may contribute to the current balance are conductance through the Z-93 paint, secondary electrons due to ion impact on the APEX body, and photoelectrons from the APEX body. Also, more current is collected from a hydrogen plasma than an oxygen plasma.

64

8.   COMPARISON OF MEASUREMENTS WITH CALCULATIONS

Using the EPSAT model of parasitic current collection described in Chapter 12, we did a series of computations of the collecting area as a function of bias and plasma density for the biased PASP Plus arrays. We did the calculations for a time during which the solar arrays were in the ram and the velocity was 7879 m s^{-1}. The plasma was taken to be all oxygen, and the plasma temperature used was 0.208 eV. The first cross over was taken to be 40 V for all the arrays. The arrays were described by the constants given in Table 3. The results of the calculations are shown in Figures 50 through 57.

Table 3. Parameters Used to Model PASP Plus Solar Arrays

array number	1	2	3	4	6	8	11	power arrays
cell (mil)	8	8	8	3.5	3.5	7	7	8
gap (mil)	60	60	32	40	40	40	40	32
coverglass (mil)	7	7	5	6	6	9	9	5
adhesive (mil)	1	1	0	5	5	5	5	0
overhang (mil)	1	1	3.5	2	2	0	0	4
generated potential	0.6	0.6	0.6	1	1	1	1	0.36
1st crossover	40	40	40	40	40	40	40	40
power model	off	off	off	off	off	off	off	sun-dependent
number of cells	20	60	4	5	4	4	8	99
number of series	1	1	1	4	3	1	1	4
gap w/o inter	0.214	0.641	0.32	0.263	0.191	0.1065	0.330	8.75
gap with inter	0.72	2.16	0	0.0528	0.0396	0.0135	0.0696	0.572
edge with metal	0.227	0.681	0	0.0264	0.0264	0	0	0
edge w/o metal	0.363	1.09	0.64	0.157	0.164	0.4	0.48	0

PASP Plus Array #1, Ram, Emitter Off, EPSAT Calculation

Figure 50. Current collected by array #1 as calculated by EPSAT.

PASP Plus Array #2, Ram, Emitter Off, EPSAT Calculation

Figure 51. Current collected by array #2 as calculated by EPSAT.

66

PASP Plus Array #3, Ram, Emitter Off, EPSAT Calculation
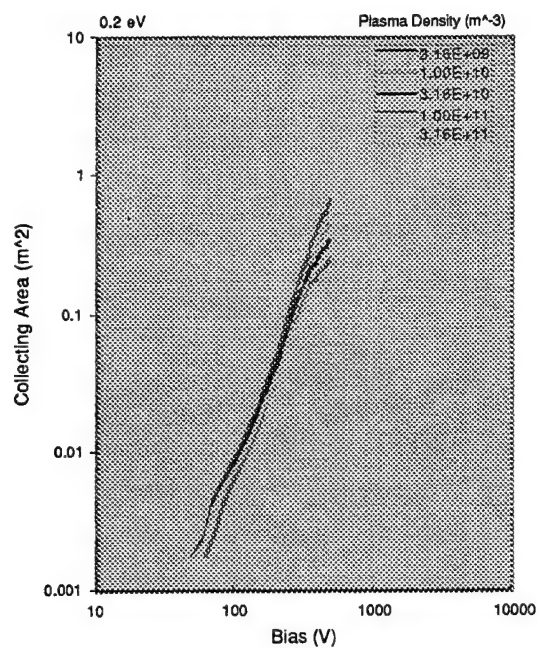
Figure 52. Current collected by array #3 as calculated by EPSAT.

PASP Plus Array #4, Ram, Emitter Off, EPSAT Calculation
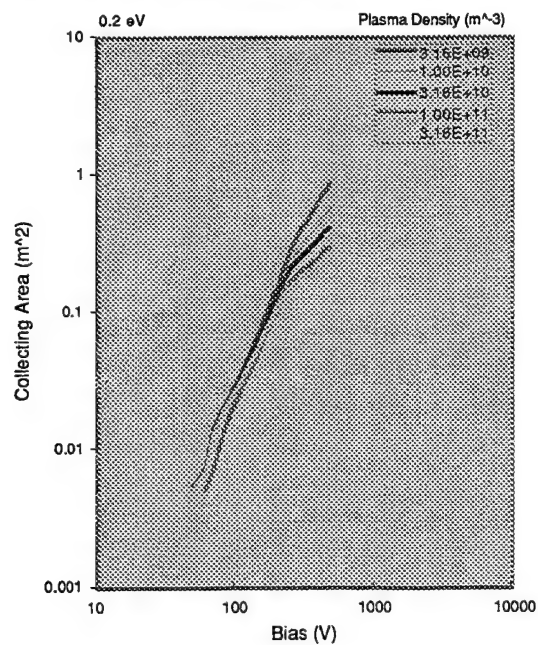
Figure 53. Current collected by array #4 as calculated by EPSAT.

PASP Plus Array #6, Ram, Emitter Off, EPSAT Calculation
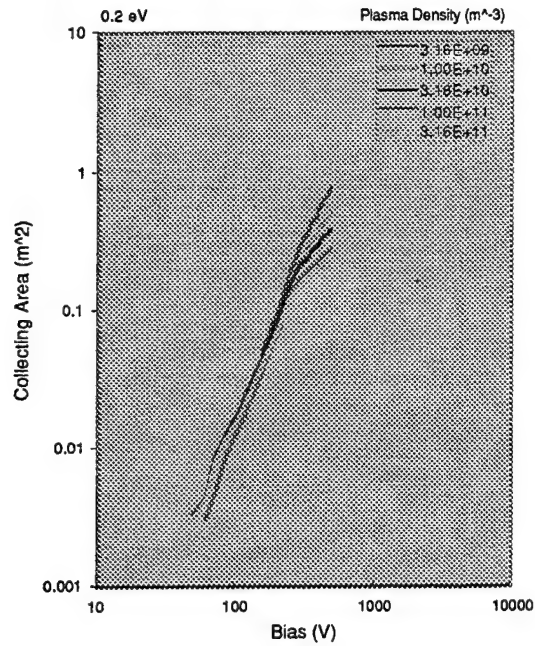
Figure 54. Current collected by array #6 as calculated by EPSAT.

PASP Plus Array #8, Ram, Emitter Off, EPSAT Calculation
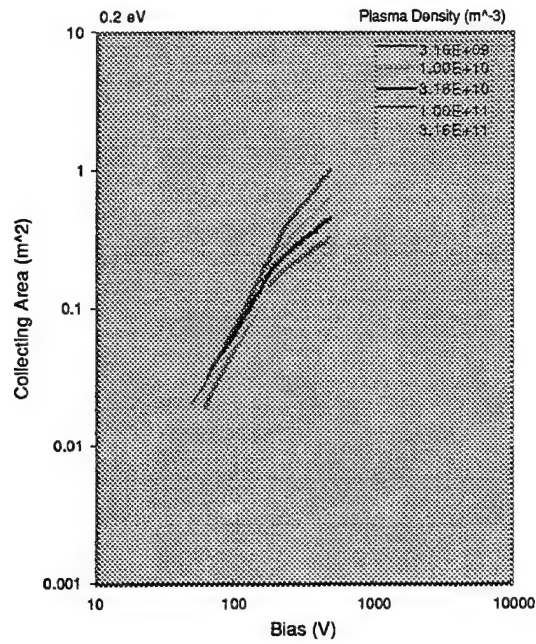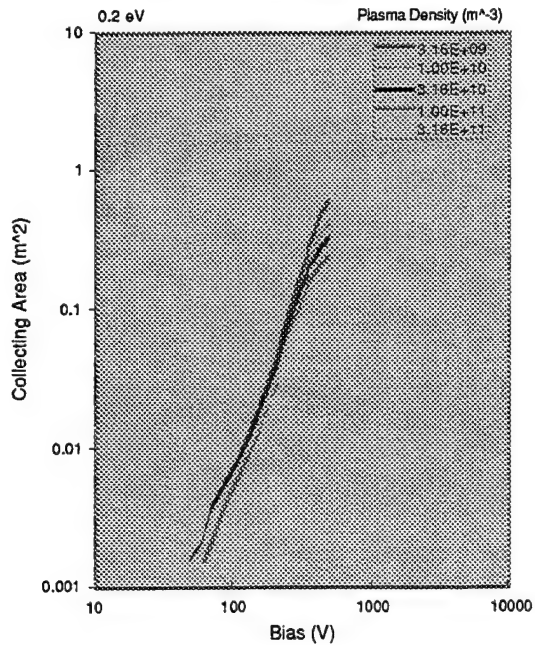

Figure 55. Current collected by array #8 as calculated by EPSAT.

68

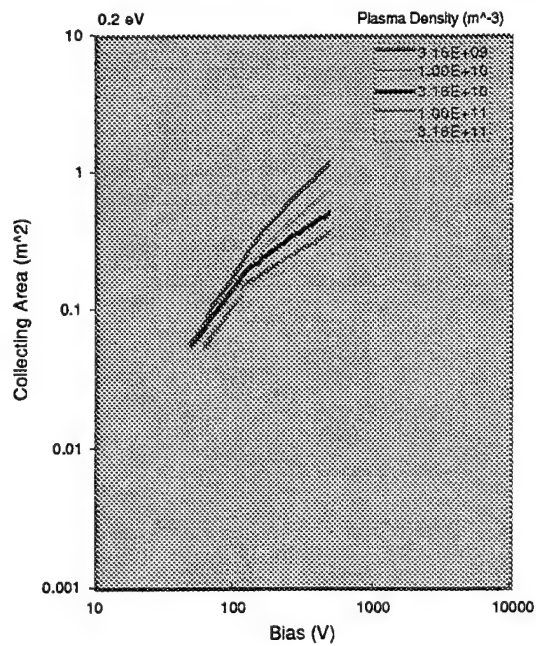PASP Plus Array #11, Ram, Emitter Off, EPSAT Calculation
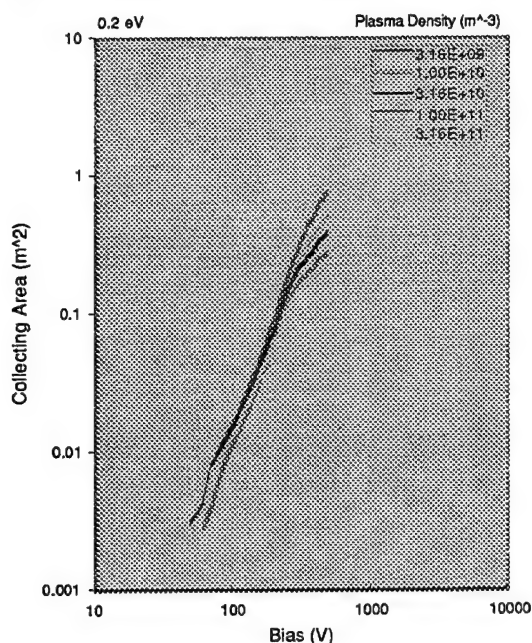
Figure 56. Current collected by array #11 as calculated by EPSAT.

A few general observations can be made about the correspondence of the calculations and the measurements shown in Chapter 5. The computed collecting area is near the measured collecting area for the low value of the first crossover chosen for the computations. The calculations reflect the trends seen in the flight data. The collecting area is many times the array area. The variation with density is small except at the higher potentials, where the APEX floating potential becomes significant. The curves are less steep when the collecting area is larger, where the APEX floating potential becomes significant. It should be noted that the APEX floating potential reaches a couple of hundred volts negative in the cases with the largest collecting areas. The ESAs did not ever measure this amount of charging due to array biasing.

Previously we did a series of calculations of the current collected by a plate the size of the array # 5 panel. The result of the calculations is shown in Figure 39. Since array # 5 is collecting current more like a resistive plate than a solar array, it is instructive to compare the current collected with the NASCAP/LEO calculation.

69
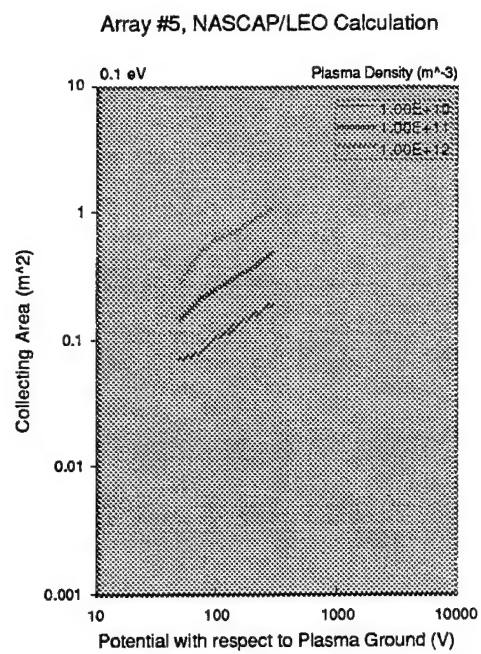
Figure 57. Current collected by array #5 as calculated by NASCAP/LEO.

9. POSSIBLE REASONS FOR SCATTER IN FLIGHT DATA

One surprising feature in the flight data is the amount of scatter. For the same bias, plasma density, and plasma temperature the collected current can vary by a factor of ten in some cases. We have used averaging to smooth the data. The reason for the variation requires investigation. In this chapter we describe several sources of variation and attempt to quantify them.

9.1 Measurement of Collected Current

The measurement of the collected current is only made with a finite precision. This measurement is then telemetered back to earth introducing another possible source of precision reduction. The applied bias is different from the actual bias and varies slightly from measurement to measurement. While no experimental apparatus is perfect, the measurement of current is routine. This experiment is a part of the primary mission of this spacecraft. For these reasons, we believe that this provides a negligible contribution to the scatter in the data.

9.2 Measurement of Plasma Density and Temperature

The ability of the Langmuir probe to accurately measure plasma density and temperature is addressed in Chapter 4. We estimate that the plasma density and temperature assigned to a specific collected current measurement are accurate to 20%.

9.3 Variation of APEX Floating Potential

Many factors can influence the APEX floating potential. Primary among them are test solar array bias and plasma density. Since the scatter is between measurements with the same bias and density, the contribution of these factors can be ignored.

Photoemission influences the floating potential of spacecraft by providing an additional source of current. If the spacecraft is negative, the photoelectrons leave, reducing the potential. At altitudes above geosynchronous, photoemission is often the dominant current and charges spacecraft slightly positive. However, photoemission only provides a significant current below plasma densities of $3 \times 10^9 \text{ m}^{-3}$. We know this because the

photoelectrons are seen by the Langmuir probe at the lower densities and because typical published values give current densities on the order of a few times 10^{-5} A/m^2.

The power solar arrays operate at different biases at different times. Generally, the arrays operate at 36 V and provide trickle charging to the battery. After leaving a long duration eclipse, the arrays are cold and the battery has been partially discharged. Under these conditions the array bias can reach 72 V. However, these conditions occur only occasionally.

At different orientations with respect to the ram, APEX collects different amounts of ion current. The NASCAP/LEO calculations of the ion current collected by APEX described in the first interim report for this contract (SSS-DPR-94-14662) suggest that the ion current variation is under 30 percent. Variation for this reason would be reduced if the flight data were sorted by ram angle.

The spacecraft velocity also influences the ion current collected. APEX velocity varies from 6000 to 8000 km s^{-1}.

The dominant ion species has an important influence on the ion current collected. As hydrogen is much lighter than oxygen, the thermal velocity of hydrogen is higher than the thermal velocity of oxygen. Hydrogen is not excluded from the wake region and has a higher thermal current. Therefore, when everything else is the same, a hydrogen plasma provides as higher ion current than an oxygen plasma. Therefore, the APEX floating potential is less negative in a hydrogen plasma.

Several of the effects that influence the APEX floating potential can be quantified using the EPSAT computer code. Figure 58 shows the collected current as a function of the applied bias to the array number 4 under the conditions at midnight on day 220 of 1994. At this time, the altitude is 659 km and the plasma is half oxygen and half hydrogen. The spacecraft velocity does not affect the collected current and the higher bias on the power arrays has a negligible effect. The variation in collected current due to ion species is a factor of approximately two at the highest biases. The associated APEX floating potential is 190 V for the hydrogen plasma and 234 for the oxygen plasma at 500 V bias. As floating potentials this high are never measured by the ESAs and the difference in collected current is significant only for the higher values of APEX floating potential, the variation seen here is probably not relevant to the flight data.
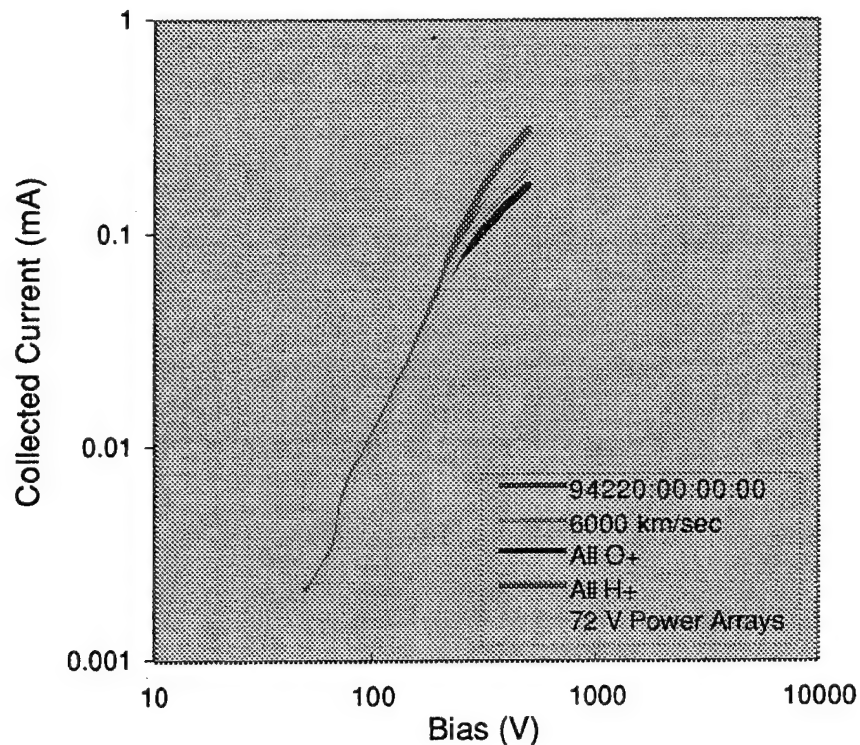
Figure 58. How various parameters affect the collected current.

9.4 Variation of Insulator Potentials

The current collected by the test solar arrays varies as the insulator potentials vary. The insulator potentials can vary from near zero to negative five times the electron temperature. Photoemission, dominant ion species, orientation with respect to the ram, and spacecraft velocity all influence the insulator potentials. At small potentials this is a major effect. A barrier to electron collection exists whenever the average surface potential on the array is negative. A barrier to collection can also exist whenever the average potential on the entire spacecraft panel is negative. By 50 V, this effect is negligible.

9.5 Variation of Surface Properties with Time on Orbit

Outgassing, ultra-violet exposure, debris and meteoroid impact and other processes can change the properties of surfaces exposed to the space environment. Changes in the secondary electron properties or the conductivity of the surfaces of the solar arrays

affect the parasitic current collection. Such changes in the PASP Plus arrays are of scientific interest. The data collected over the nine month period and shown in Chapter 5 is expected to show such changes. If the variation in surface properties over time were the cause of the scatter in the data, a single month's worth of data would have less scatter. This does not appear to be the case.

9.6   Unstable/Bistable Nature of Snapover

The current collected depends on the amount of the surface that is snapped over. As the conditions of snapped over and not snapped over are both stable, each portion of the solar array may be snapped over or not. In the laboratory, under apparently non-varying conditions, the current has been seen to jump suddenly at the same time as a visual glow assumed to be associated with snapover moves on the surface [Conversation with Dale Ferguson]. One argument against this being a significant contribution to the scatter seen in the flight data is that the current is usually stable for the 23 second period during which a measurement is made.

9.7   Variation in Other Parameters

Our understanding of the processes occurring in the PASP Plus current collection experiment is of necessity incomplete. There could be another factor that has not been taken into account yet that has a much larger role than expected. One parameter that does vary is the attitude of APEX. We do not expect the attitude to be important as all of the measurements presently being examined are for the solar arrays facing the ram direction. We have noticed several instances that have particularly high current in which the ram-sun direction angle is 87 degrees. We will study this possibility systematically.

9.8 Summary

The reason for the wide variation in the flight data remains unexplained at present. It is possible that the variation in ion species is creating an important variation in collected current due to its influence on the APEX floating potential. It is possible that there are many different widely varying currents that are physically consistent with each bias potential and plasma condition. It is most likely that another parameter that is presently not being held constant accounts for the variation.

10. CURRENT COLLECTION UNDER NEGATIVE BIAS

We examined the current collection characteristics of the test solar arrays when they were biased negatively. This work was primarily motivated by a desire to learn the surface conductivity of the Germanium on the surface of array 5 so that this conductivity could be subtracted from the apparent current collected to obtain the current collected from the surrounding plasma.

We examined the leakage current for days 291 to 294 of 1994. On these days, the arrays were biased negatively from 160 to 400 V and any arcing was examined. Here we are concerned with the leakage current measurements. We averaged all the measurements taken at a given applied bias. Figure 59 shows the collected current as a function of applied bias for all the arrays.
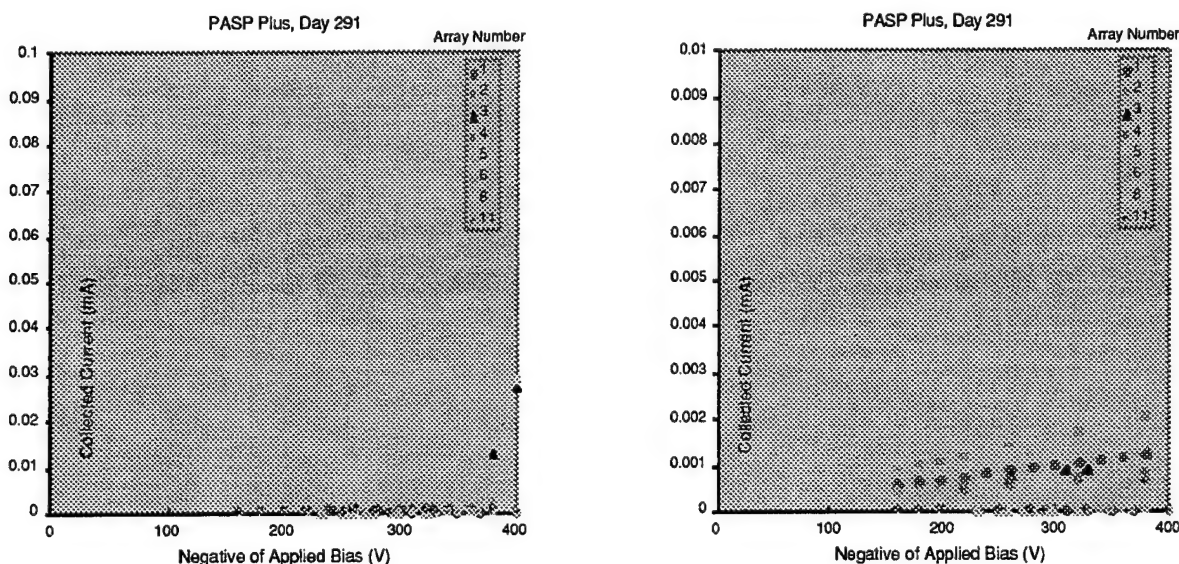
Figure 59. Collected current as a function of applied bias for negative bias. The same data is shown twice at different scales.

Most of the arrays show a predominately straight line current-voltage characteristic. Table 4 shows the slope and intercept for a least square fit line to each array, ignoring the last two points for arrays 3 and 8. Excepting array 5, the resistance varies by a factor of four from 200 to 750 MΩ. Excepting array 5, the intercept is always about 0.1 to 0.2 μA.

76

Table 4. Current Voltage Linear Characteristic

Array #	Slope (1/MΩ)	Resistance (MΩ)	Intercept (μA)	Quality of Fit
1	0.0029	350	0.13	1.00
2	0.0051	195	0.07	1.00
3	0.0021	478	0.21	0.89
4	0.0017	593	0.18	0.99
5	0.3351	3	-4.93	0.99
6	0.0013	744	0.18	0.97
8	0.0021	481	-0.21	0.96
11	0.0015	647	0.11	0.95

As many of these measurements were made in the wake or under low plasma density conditions, we can initially postulate that these measurements are of surface currents and internal resistances.

We can compare these measurements with those made on arrays similar to the APSA array at NASA/LeRC.[1] (G. B. Hillard, Plasma Chamber Testing of APSA coupons for the SAMPIE Flight Experiment, Aerospace Sciences Meeting, January 1992) For the APSA array without the carbon loaded Kapton blanket, the resistance was over 600 MΩ. For the APSA array with the carbon loaded kapton blanket, the resistance was approximately 1 MΩ. For the APSA array without the carbon loaded kapton blanket and with a Germanium coating, the resistance was approximately 150 MΩ. This last design is that flown on PASP Plus.

11. THE APSA ARRAY

Array 5 (sometimes known as array 36) shows a different collected current-applied bias relation than the rest of the arrays. This is because it is coated with a layer of Germanium, which is a semi-conductor. The measured current is enhanced due to processes. Current is conducted through the Germanium coating even in the absence of plasma. This parasitic current is linear with the applied bias with a resistance of 3 MΩ as described in Chapter 10. Current is also collected from the plasma. This current is comparable to the current collected by an array with a low first crossover potential. Figure 60 shows the effective circuit. Current is collected across the entire surface of the array.
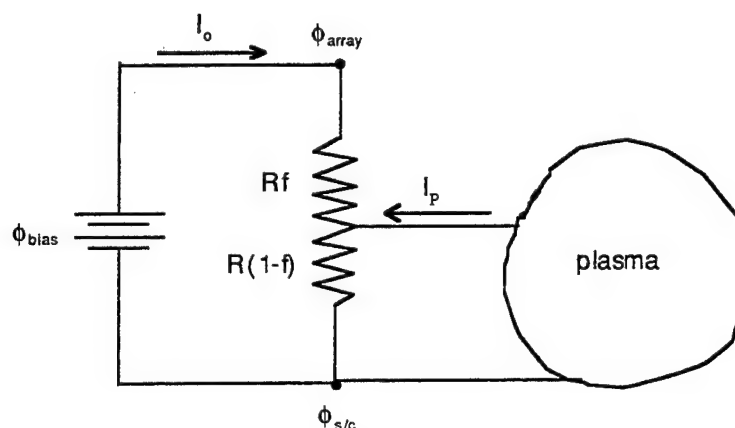
Figure 60. Effective circuit for collection of current by array 5.

The measured current I_o is given by the following:

$$I_o = f\, I_p + \frac{\phi_{bias}}{R} \tag{13}$$

The fraction f is used to account for the fact that electrons are collected by the entire surface and not just at the array potential. When we subtract the parasitic current collected from the measured current we get the collecting area curves shown in Figure 61. These can be compared with similar figures in Chapter 5.

78
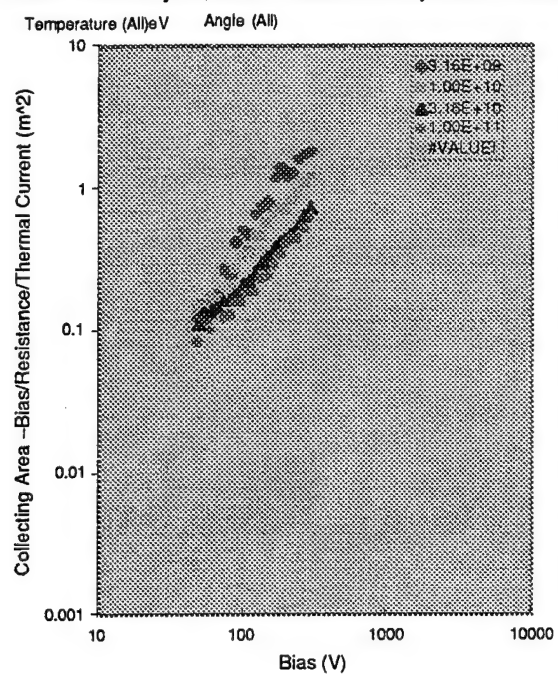
Figure 61. Collecting area as a function of bias for array #5.

12. EPSAT MODEL OF PARASITIC CURRENT COLLECTION

The EPSAT model for the current collected by a single solar cell was developed by the S-Cubed Division of Maxwell Laboratories, Inc.

A solar array model is defined by properties of an individual solar cell and by properties of the array as a whole. These properties can be set by the user on the corresponding pop-up forms accessed from the solar array definition form and are uniquely defined for each solar array. Other variables accessed on the solar array definition form include environmental parameters and table calculation parameters. These inputs are used to calculate the current-voltage curve for the solar array and are defined as follows:

12.1 Cell Properties

$\Delta\phi$ = Potential generated by a single solar cell.

V_{snap} = Snapover Potential (First Crossover Energy)

m_i = Ion Current Slope

T_{cell} = Cell Thickness

D_{gap} = Gap Width

T_{cg} = Coverglass and Adhesive Thickness

T_{adh} = Adhesive Thickness

T_o = Coverglass Overhang

Figure 62 illustrates the solar cell gap region which is modeled using the above parameters.
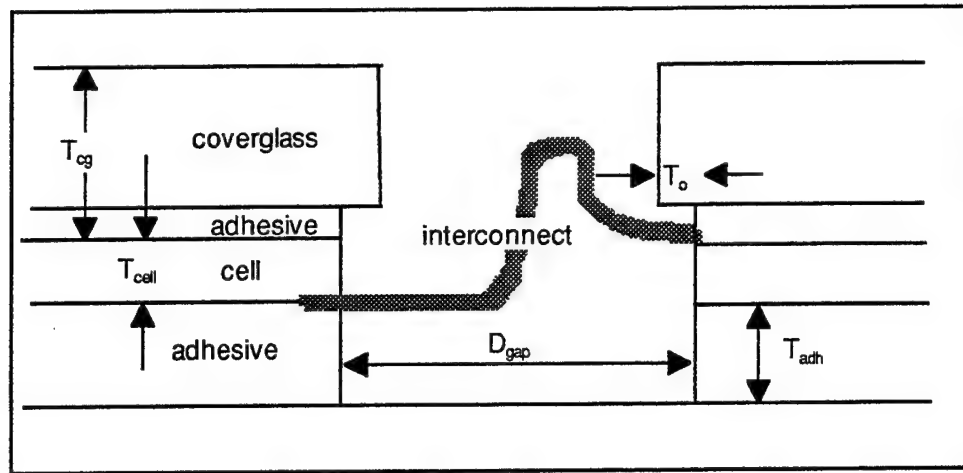
Figure 62. Solar cell gap region.

12.2   Array Properties

L_i = Total Interior Length without Interconnect

L_{ic} = Total Interconnect Length

L_e = Total Edge Length without Metal

L_m = Total Edge Length with Metal

N = Number of Cells per Series

N_s = Number of Series

V_{gen} = Generated Potential = N $\Delta\phi$

Power Model =On/Off/Sun Dependent

The array geometry is shown in Figure 63.
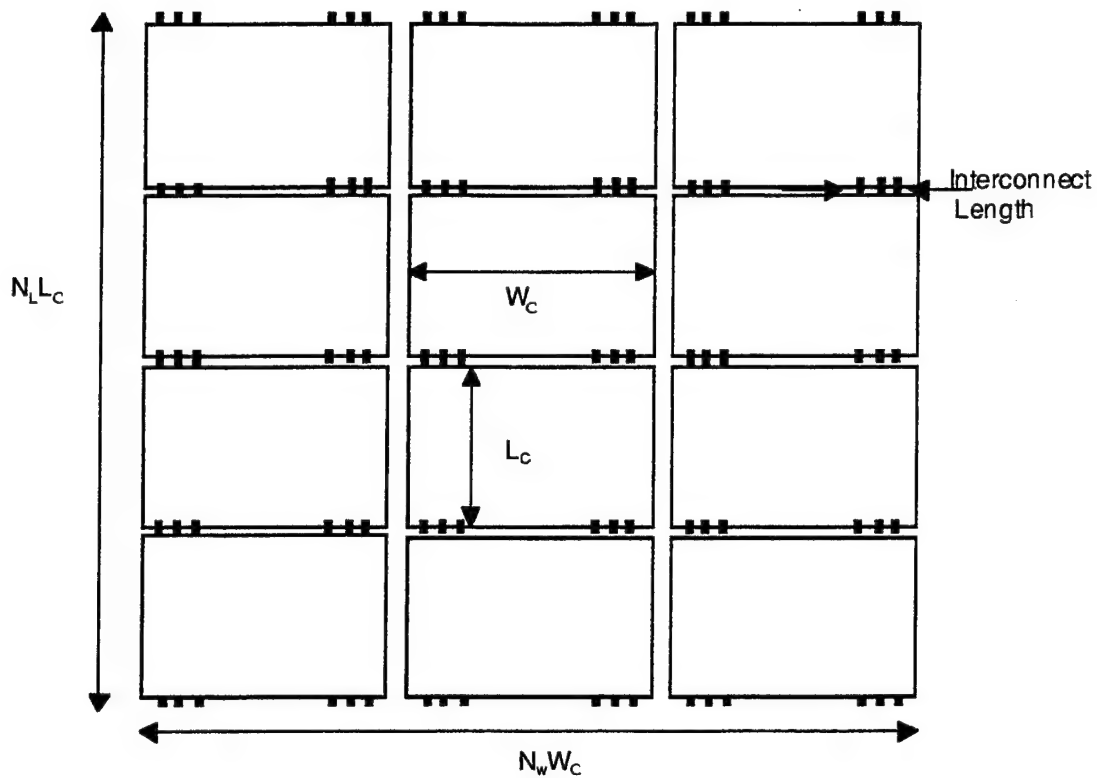
Figure 63. Solar Array with 12 cells in series.

The relationship between the cell properties and the array properties for this array is:

L_{ic} = Interconnect length*number between cells

L_m = Interconnect length*number along edges

$L_e = 2N_wW_c + 2N_lL_c - L_m$

$L_i = (N_W-1)N_LL_C + (N_L-1)N_WW_C - L_{ic}$

12.3 Environment Parameters

n_o = Plasma Density

θ = Plasma Temperature

12.4   Global Array Parameters

The Global Ground and Table Parameters section on the Solar Array Definition form contains parameters which apply to all solar arrays. These are the values of solar array ground and table calculation parameters that a solar array gets by default. To change these parameters for an individual solar array, the table calculation parameters and ground should be accessed from the Solar Array IV Curve Specification form and changed there.

The solar array ground parameter is a toggle field which takes on the value "pos" or "neg". A negative ground solar array is connected to the system at its low potential end, while a positive ground solar array has its high potential end connected to the system. These two groundings result in very different system floating potentials and represent the positive or negative grounding of the system.

The minimum and maximum potentials for the current-voltage and effective area curves define the range of potentials for which these tables are calculated. Values outside this range are calculated by linear extrapolation.

12.5   Current-Voltage Curve

A solar array is represented electrically by a current-voltage curve, i.e., a table of solar array to plasma potentials and the currents collected by the solar array at the specified potentials. The current for a specific potential is determined by interpolation. The potentials across the cells in a series are added to give the solar array generated potential. The total current collected by a series is just the sum of the currents to each cell.

The Solar Array IV Curve Specification screen for each solar array shows the current-voltage curve calculation parameters for that solar array, the angle between the solar array surface and the ram, and the electron and ion flux to the solar array surface. Also displayed is a point on the curve that the user can access by setting the potential and updating the screen to get the corresponding current. These fields can be used to plot the current-voltage curve.

83

The solar cell effective area versus cell potential curve can be viewed by choosing the "View Effective Area Curve" field. This form shows the effective area table, the parameters for calculating this table and a point into the curve, much like that on the Solar Array IV Curve Specification form, which the user can use to make a plot of the curve or look at a specific point on the curve.

The collection curve can be either fixed or calculated. If a fixed collection curve is used, the effective area curve shown on the form is used for all conditions. If a calculated collection curve is used, the following description of how the curve is calculated applies.

12.6   Current Collected

The current collected from the plasma by a solar cell is collected on the sides of the solar cell, and by the interconnects, if any. It is calculated as the product of the solar cell effective collecting area and the incident current density of the attracted species. The attracted species depends on whether the cell potential with respect to the plasma is positive or negative.

The effective area is a function of the electrical and geometric properties of the cell and environmental parameters and is calculated as described below.

12.7   Single Cell Electron Current Collection

For electrons the effective collecting area is calculated as the sum of four terms:

$$A_{coll}(\phi_c) = \frac{L_{ic} \, W_s^{ic}(\phi_c) + L_i \, W_s^i(\phi_c) + L_e \, W_s^e(\phi_c) + L_m \, W_s^{ic}(\phi_c)}{N} \qquad (14)$$

Where,

A_{coll} = Solar cell effective collecting area

W_s^{ic} = Sheath width for interconnects

84

W_s^i = Sheath width for gaps without an interconnect

W_s^e = Sheath width for edges

ϕ_c = Solar cell potential with respect to the plasma

The area is the computed from several two-dimensional segments. It is the distance along the solar cell edge times the length of the two-dimensional sheath. The technique to calculate the sheath width is described in the section "Solar Cell Sheath Width Model."

sheath width

Current from this portion of the sheath is collected.

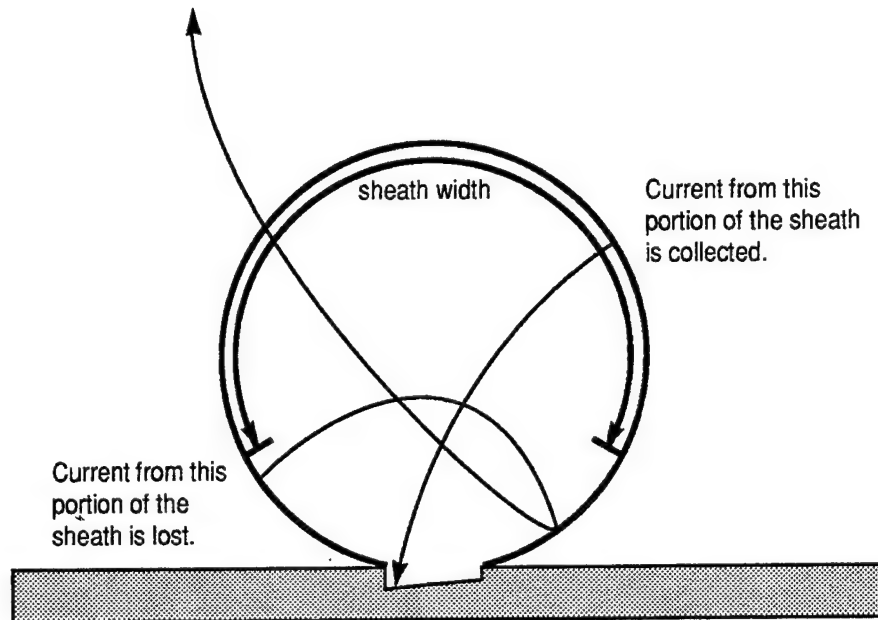Current from this portion of the sheath is lost.

Figure 64. Solar cell gap with sheath.

12.8   Single Cell Ion Current Collection

Ion collection, which occurs when the cell potential is negative with respect to the plasma, is given as a linear function of the cell potential. The effective collecting area is as follows:

$$A_{coll}(\phi_C) = m_i\,\phi_c \qquad (15)$$

85

12.9 Solar Cell Sheath Width Model

The two-dimensional electron collecting sheath width for a solar cell is modeled using the following formula:

$$S.\,W. = 1.1\,A\,(\text{geom.})\,B\,(\eta)\,\frac{\phi^{0.35}}{\max\,(0.1,\eta)^{0.65}}\exp\left(\frac{0.63}{\lambda^{0.7}} + \frac{1}{\max\,(0.1,\eta)}\left(0.44 - \frac{7}{\phi} - \frac{1.13}{\lambda^{0.7}}\right)\right) \quad (16)$$

where the function B is

$$B(\eta) = \begin{cases} 1/3 & \text{no interconnect geometry and } \eta > 0.6 \\ 1 & \text{otherwise} \end{cases}$$

$$\eta = \min(1, \text{1st crossover potential}/\text{cell potential}) = \min(1, V_{snap}/\phi_c)$$

$$\phi = \text{Cell potential}/\text{plasma temperature} = \phi_c/\theta$$

$$\lambda = \text{Debye length}/\text{cell thickness} = \sqrt{\varepsilon_o\theta/e\,n_o}/T_{cell}$$

This formula should not be applied to scaled potential values greater than 500/0.05.

12.10 Solar Array Current

To get the total current collected by the solar array, we sum the currents to all the solar cells as follows:

$$I_{sa}\,(\phi_a) = N_s^{on}\sum_{n=1}^{N}A_{coll}\,(\phi_a + n\,\Delta\phi)\,j_{th}^a\,(\theta_{ram},\,\phi_a + n\,\Delta\phi) + N_s^{off}\,N\,A_{coll}\,(\phi_a)\,j_{th}^a\,(\theta_{ram},\,\phi_a) \quad (17)$$

Where,

N_s^{on} = Number of series of solar cells that are on

N_s^{off} = Number of series of solar cells that are off

j_{th}^a = Current density of attracted species

86

ϕ_a = Array Potential

θ_{ram} = Angle between the solar array face and the ram

The incident current density of the attracted species, j_{th}^a, is calculated as described below:

$$
\begin{aligned}
j_{th}^a(\theta_{ram}, \phi) &= j_{th}^i \, \chi(\theta_{ram}) && \text{for } \phi < 0 \\
&= j_{th}^e && \text{for } \phi > 0, \theta_{ram} \leq 90° \\
&= j_{th}^e \, \chi(\theta_{ram}) && \text{for } \phi > 0, \theta_{ram} > 90°
\end{aligned}
\tag{18}
$$

j_{th}^i = One-sided random ion thermal current

j_{th}^e = One-sided random electron thermal current

The angle, θ_{ram}, changes with present orientation.

The function $\chi(\theta)$ is used to smoothly interpolate between the ram-dominated ion current on ram facing surfaces and the thermal-dominated ion current on wake facing surfaces. It is given by:

$$
\chi(\theta_{ram}) = e^{-s^2 \cos^2 \theta_{ram}} + \sqrt{\pi} \, s \cos \theta_{ram} \left[1 \pm \operatorname{erf}(s \cos \theta_{ram}) \right]
\tag{19}
$$

where the "+" sign applies in the ram and the "-" sign in the wake[2]. The parameter s is given by:

$$
s = \frac{e \, n_o \, v_{ram}}{\sqrt{4\pi} \, j_{th}^i}
\tag{20}
$$

where

v_{ram} = Magnitude of v.

The number of series on is determined by the power model chosen on the array properties screen. If the power model is "sun-dependent", then the number of series on is dependent on whether the system is in the sun (all series on) or in eclipse (no series on). If the model is "off" then no series are ever on, and if the model is "on" then all series are always on.

13. ELECTRON BEAM—SHUTTLE ENVIRONMENT INTERACTIONS

13.1 Ion Spectrum

We have compared the spectrum computed using the technique described in Chapter 14 with SPREE measurements for a period during which the FPEG beam was perpendicular to the Earth's magnetic field. This is the event described in Hardy et al[3].

Using the ambient environment and magnetic field of Day 216 at 20:06:40, the path of the electron beam centroid looks as shown in Figure 65. The beam is color-coded by ionization rate. In actually the beam spreads so much that it is only during the first turn that significant localized ionization takes place. The following calculations only follow the beam for the first turn.
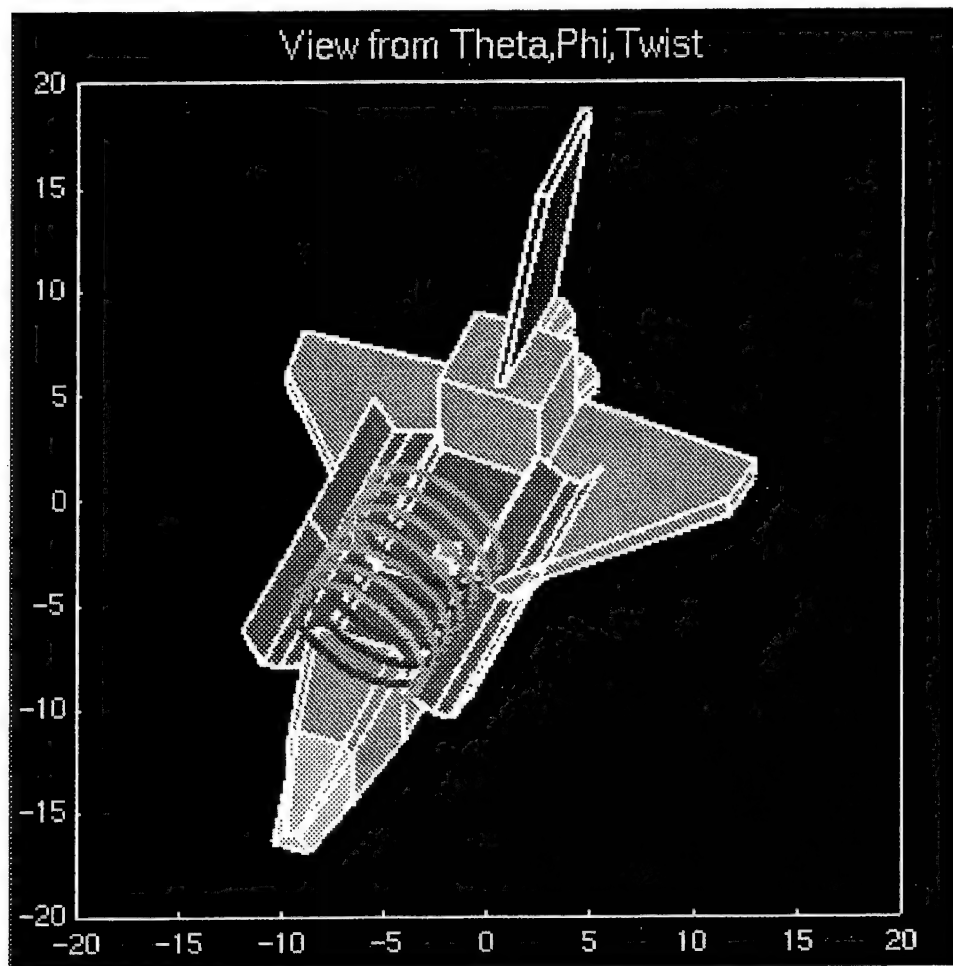
Figure 65. FPEG electron beam and shuttle on day 216 at 20:06:40.

Figures 66 and 67 show the differential ion flux seen by SPREE in the lowest channel as a function of look direction. The top half of the plot is out of the bay. The bottom half of the plot is through the bay and therefore would not be seen. The center of the plot is toward the nose and the sides are toward the tail. SPREE sees ions whenever it is looking at the beam.
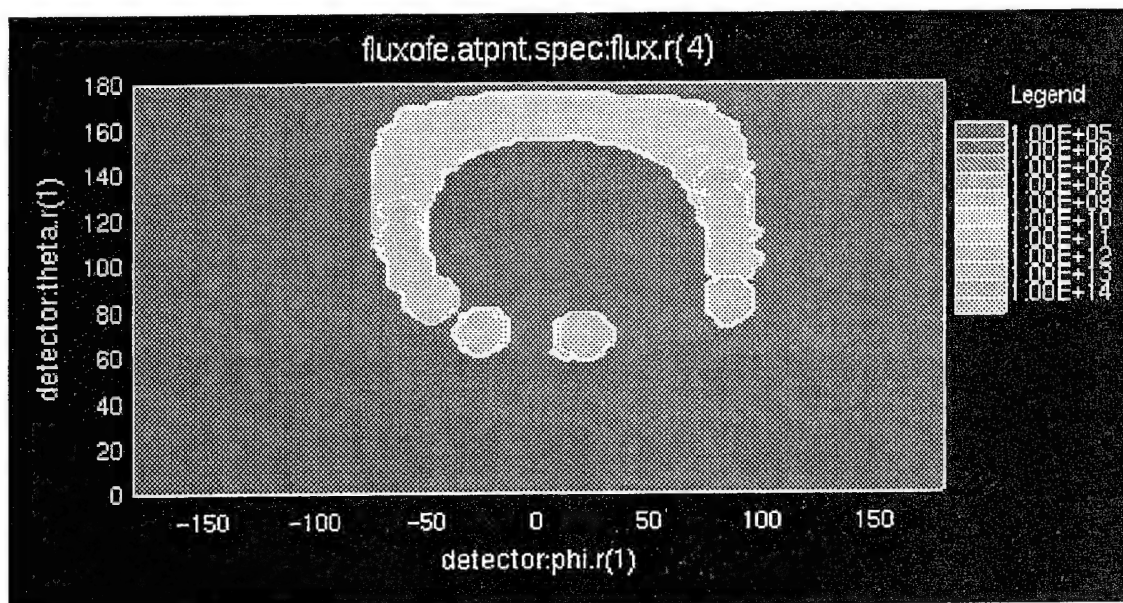
Figure 66. Differential ion flux as seen by SPREE, ambient neutral environment.
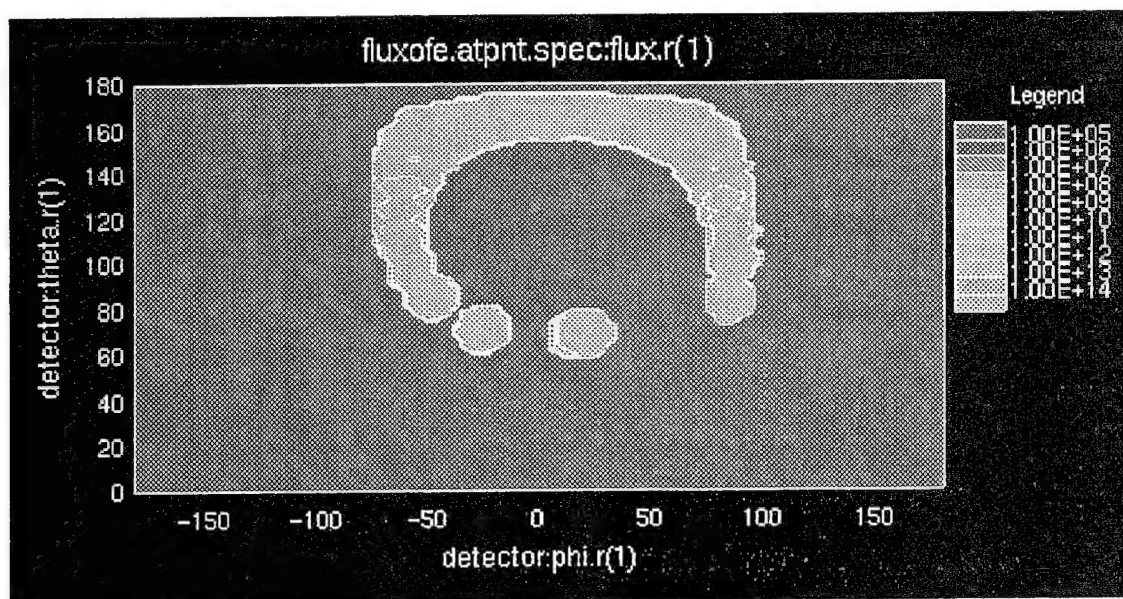
Figure 67. Differential ion flux as seen by SPREE, ambient neutral environment and the L1L thruster.

The kinetic energy of the ions is due to two factors. The ions have energy because they were created in a region of high plasma density. They also have energy due to acceleration into the sheath of SPREE if the shuttle is negative with respect to the

91

plasma. This second effect is not at present accounted for in the calculation of the spectrum.

Figure 68 shows the ion and electron number flux to SPREE for day 216 of 1992 from 20:06 to 20:21. Whenever the beam is on, electron flux is observed in all the zones. At an azimuth of 0 degrees the beam is toward and just ahead of SPREE. Few ions are seen at 0 degrees. At 180 degrees, SPREE is facing the beam source. Ion are seen in all zones at 180 degrees. At 90 degrees, when SPREE is facing forward, ions are seen mostly in zone 8, which faces the beam.
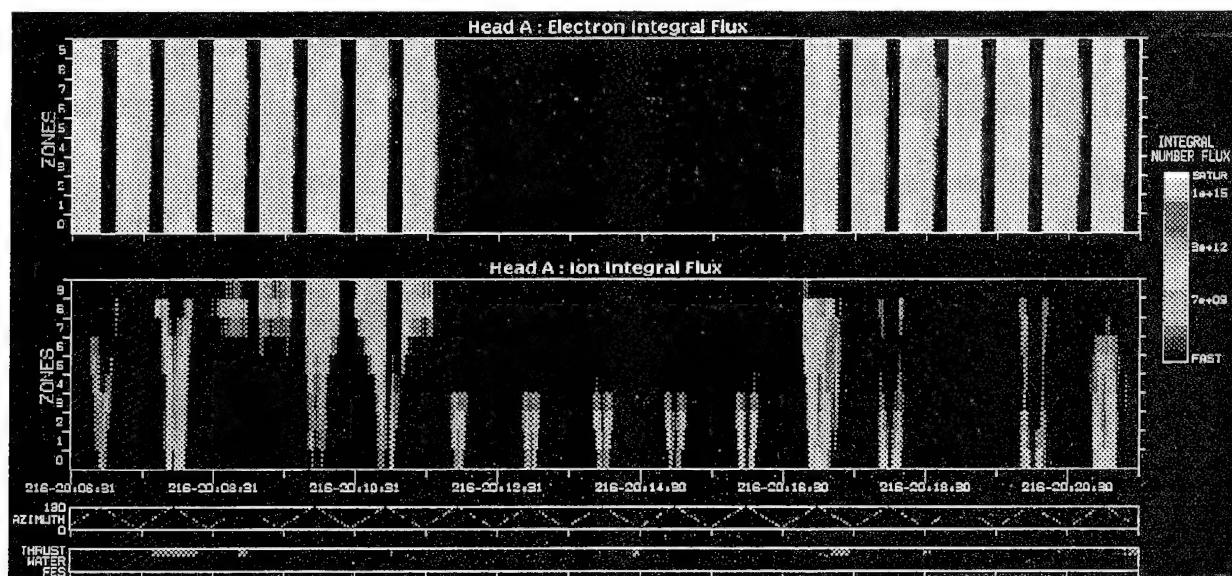
Figure 68. Electron and ion flux to SPREE for day 216 of 1992 from 20:06 to 20:21.

Figure 69 shows a typical spectrum to SPREE during the period shown in Figure 68. There are ions with energies up to 23 eV This may indicate that the orbiter is negative about 15 V with respect to the plasma.

92
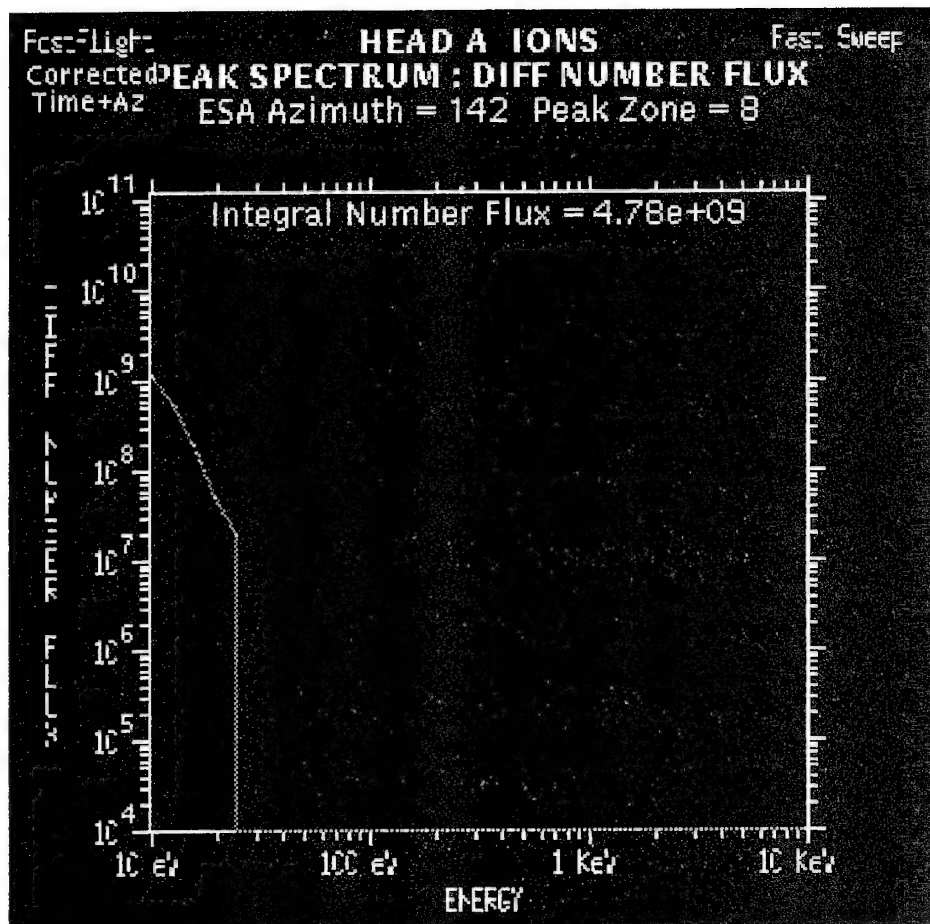
Figure 69. Typical spectrum to SPREE during the period shown in Figure 68.

13.2 Beam Spreading

One of the questions raised when calculating the ion spectrum due to the interaction of the electrons with the neutral environment is what is the beam diameter. The beam starts small and spreads. There are two conditions that determine the diameter at which the beam stops spreading due to electrostatic forces: (1) Beam spreading stop when the beam density reaches ambient and (2) Beam spreading stops when enough ions are formed to counter the beam electron charge.

At what diameter does the beam density reach ambient?

The charge density due to beam electrons is

93

$$\rho_{beam} = \frac{I}{v_{beam}\pi R^2} \tag{21}$$

The beam does not spread if

$$\rho_{beam} < en_{ambient} \tag{22}$$

$$\frac{I}{v_{beam}\pi R^2} < en_{ambient}$$

$$R > \sqrt{\frac{I}{\pi v_{beam}en_{ambient}}} = \sqrt{\frac{I}{\pi 5.93 \times 10^5 \sqrt{E}\, en_{ambient}}}$$

Substituting in typical values

$$R > \sqrt{\frac{0.1}{\pi 5.93 \times 10^5 \sqrt{10^3}\; 1.6 \times 10^{-19} 10^{11}}} = 0.33 \text{ m} \tag{23}$$

At what diameter does the ion charge density equal the electron charge density?

What is the charge density of the created ions?

The volume creation rate is

$$\frac{\text{ions}}{\text{sec m}^3} = \frac{\sigma}{\pi R^2}\frac{I}{e}n_o \tag{24}$$

The ion charge density is

$$\rho_{iz} = \frac{\sigma}{\pi R^2}I\, n_o \frac{R}{v_{ion}} \tag{25}$$

If we assume that the contribution of the created electrons is negligible, the charge density due to beam electrons is

$$\rho_{beam} = \frac{I}{v_{beam}\pi R^2} \tag{26}$$

The beam does not spread if

$$\rho_{beam} < \rho_{iz} \tag{27}$$

$$\frac{I}{v_{beam}\pi R^2} < \frac{\sigma}{\pi R^2} I\, n_0 \frac{R}{v_{ion}}$$

$$\frac{1}{v_{beam}} < \sigma\, n_0 \frac{R}{v_{ion}}$$

$$\frac{1}{5.93 \times 10^5 \sqrt{E_{beam}}} < \sigma\, n_0 \frac{R}{1.38 \times 10^4 \sqrt{\dfrac{E_{ion}}{amu}}}$$

$$R > \frac{1}{\sigma\, n_0} 2.33 \times 10^{-2} \sqrt{\frac{E_{ion}}{amu \times E_{beam}}}$$

Substituting typical values

$$R > \frac{1}{10^{-20}\, 10^{14}} 2.33 \times 10^{-2} \sqrt{\frac{0.025}{16 \times 10^3}} = 29 \text{ m.} \tag{28}$$

If the neutral density is higher (as it often is), this radius would be smaller.

Since the first effect gives a smaller radius, After a radius of 0.33 m the beam is quasi-neutral and the spreading slows.

14. ELECTRON BEAM IONIZATION MODEL AS IMPLEMENTED IN EPSAT

14.1   Electron Beam

The electron beam screen is used to set the beam parameters and view the beam path.

The beam source (electron gun) location, initial direction, and kinetic energy are specified in body centered coordinates.

The electron beam trajectory is calculated by computing the motion in the direction of the magnetic field and perpendicular to the magnetic field separately. Each trajectory segment is a "helix delta" long in radians. The trajectory is tracked either the "helix length" along the magnetic field or 1000 times the "helix delta," whichever is shorter. Each segment of the trajectory is checked to see if it intersects a surface. If it does, "ihit" is set to zero and the number of the segment is displayed. If "ihit" is one, the segment number is not meaningful.

The beam ionization view color codes the beam trajectory by the ionization rate of the specified species. (See Electron Beam Ionization.)

14.2   Electron Beam Ionization

The electron beam ionization screen describes the current to a detector due to electron beam ionization.

The neutral species to be included in the calculation are specified by adding and deleting species using the Add Species and Delete Species execute fields. The selected species are shown.

The Beam Ionization View shows the object and the electron beam, with the beam color-coded to indicate the ionization rate of the specified species along the trajectory.

The beam source (electron gun) location and kinetic energy are specified in body centered coordinates. The beam current and diameter assuming no divergence are specified.

The detector position, orientation, acceptance angle, and energy bins are specified. The energy bins are specified by giving the minimum and maximum energy measured, the number of bins, and their spacing. The species energy is the energy at which the differential number flux is computed.

The density and flux of ions at the detector is computed from the beam trajectory and the assumption that the ionized neutrals expand in a radial barometric field. Only those trajectory points within the acceptance angle are included in the flux.

$$\text{Density} = \sum_{\text{trajectory points}} \frac{\dot{n}_i \theta_i}{4 \pi r^2 \sqrt{\dfrac{e \theta_o}{m} + \dfrac{2 e \Delta \phi_i}{m}}} \tag{29}$$

$$\Delta \phi_i = \theta_o \ln(n_i / n_o)$$

$$\text{Flux}(E) = \sum_{\text{trajectory points with} E = \theta_o + \Delta \phi_i} \frac{\dot{n}_i \theta_i}{4 \pi r^2}$$

where $\dot{n}$ is the ionization rate, θ_i is the arc distance associated with the trajectory point, r is the distance from the trajectory point to the detector, θ_o and n_o are the background plasma temperature and density, and n_i is the density in the beam.

The ionization rates are given by the energy dependent cross-section of nitrogen. The density at the detector for each species is shown. The differential number flux to the detector for each species is shown.

The specified species are used to color code the Beam Ionization View and to determine the displayed total density.

15. EPSAT WAKE STUDIES SCREEN

The EPSAT Wake Studies screen uses the neutral approximation to compute the densities and current densities of the neutral and plasma species in front of or behind a disk. The input parameters are the disk parameters, the spacecraft velocity, the ambient neutral and plasma environment, the point of interest, the look direction, and the incident energy.

The disk is described by its normal, its radius, and the location of its center. The normal of either the ram facing side or the wake facing side can be given.

By default the spacecraft velocity is given by the EPSAT orbit generator.

The ambient neutral and plasma environments are shown on the Neutral Density at a Point and Plasma Density at a Point screens. The density of each neutral and ion species and the neutral and ion temperatures are used.

The point of interest can be specified either by specifying an origin and a distance from that origin in spherical coordinates or directly in Cartesian coordinates.

The look direction can be specified either in terms of the spherical coordinate angles or in Cartesian coordinates. This parameter is only used for the current density computation.

The incident energy is given in electron volts. This parameter is only used for the current density computation. If the energy is negative, the current density is zero.

15.1 Densities

On the ram facing side of the disk, the densities are the ambient densities. The point of interest is on the ram facing side if the dot product of the normal of the wake facing side of the disk with the vector from the center of the disk to the point of interest is negative.

On the wake facing side of the disk, the density for each species is the integral

$$\rho(r) = \rho_a(\pi T)^{-3/2} \int d\Omega \, dE \sqrt{E} \, g(r,\theta,\phi) \exp\left(-\left(\frac{E + E_{ram} + 2\sqrt{E\,E_{ram}}\cos\theta}{T}\right)\right) \quad (30)$$

The ambient density of the species is ρ_a. The ion temperature is T. The vector **r** is the vector from the center of the disk to the point of interest. The energy E is the incident particle energy. The energy E_{ram} is given by:

$$E_{ram} = \frac{1}{2} m_s v_{ram}^2 \quad (31)$$

where m_s is the mass of the species and v_{ram} is the spacecraft velocity. The integral is done over the polar coordinates θ and ϕ, representing the negative of the incoming particle's velocity direction, where the origin for the integral is at the point of interest and θ is measured from the negative spacecraft velocity direction. The function g is zero if the direction given by θ and ϕ is blocked by the disk and unity otherwise.

The integral is solved differently for the case where the disk is normal to the spacecraft velocity and where it is not. A different technique is also used for the case in which the point of interest is directly behind the disk and where it is to the side.

15.2 Solution Technique for Normal Orientation and Point Directly Behind Disk

The outermost integral over the azimuthal angle, ϕ, is performed taking zero as the direction to the nearest disk edge point. To get a concentration of points near the nearest edge point, we define $\psi = \phi^{1/2}$. The minimum value of $\cos\theta$ can be shown to be

$$u_{min}(\phi) = -\left[1 + (x/z)^2\right]^{1/2} \quad (32)$$

$$x/r = -\cos\phi + \left[\cos^2\phi + (R/r)^2 - 1\right]^{1/2}$$

(The maximum value of $\cos\theta$ is 1, for particles overtaking the spacecraft from behind.) The energy variable is transformed by $t = e^{-E/E_0}$, where E_0 is an enerutational convenience. It is taken to be

$$E_0 = \left(\frac{m}{2e}\right) \frac{\left(V + 5\sqrt{\frac{2eT}{m}}\right)^2}{\ln(n_t)} \tag{33}$$

where n_t is the number of integration points used for the t-variable (i.e., energy). (Note: E_0 should be set to at least the ion temperature, T.)

After appropriate manipulation, the density at a point in the wake of the disk is given by

$$\frac{\rho}{\rho_a} = \pi^{-3/2} \frac{E_0}{\sqrt{T\,E_{ram}}} e^{-E_{ram}/T} \int_0^{\sqrt{\pi}} \psi\, d\psi \int_0^1 dt\, K(\psi, t) \tag{34}$$

$$K(\psi, t) = t^{\left(\frac{E_0}{T} - 1\right)} \left\{ e^{-\gamma(t)\,u_{min}(\psi)} - e^{-\gamma(t)\,u_{max}(\psi)} \right\}$$

$$\gamma(t) = \sqrt{\frac{-4\,E_0\,E_{ram}\ln t}{T^2}}$$

Note that, to avoid overflows, all the exponents (including the one in the prefactor) should be grouped together, so that the only exponentiations are the two in the inner loop.

EPSAT performs the integrals numerically.

15.3 Solution Technique for Normal Orientation and Point Not Directly Behind Disk

The integral is over those trajectories blocked by the disk, and the result subtracted from unity. The outer integral is over the angle between the look direction and the vector toward the ram, which takes the range

$$\frac{1}{\sqrt{1 + \left(\frac{R+r}{z}\right)^2}} < u = \cos\theta < \frac{1}{\sqrt{1 + \left(\frac{r-R}{z}\right)^2}} \tag{35}$$

To concentrate points toward the ram direction, the integration variable is changed to $w = \sqrt{1-u}$. The integral over azimuthal angles contributes a factor

$$\Delta\phi(u) = 2\arccos\left\{\frac{\left[\left(r^2 - R^2 - z^2\right)u^2 + z^2\right]}{\left[2rzu\left(1-u^2\right)^{1/2}\right]}\right\}. \tag{36}$$

The final result is:

$$1 - \frac{\rho}{\rho_0} = \left[\frac{E_0}{\pi T}\right]^{3/2} e^{\frac{-E_{ram}}{T}} \int_{\sqrt{1-u_{max}}}^{\sqrt{1-u_{min}}} w\,dw\,\Delta\phi\left(1-w^2\right) \int_0^1 dt\,K'\left(1-w^2, t\right) \tag{37}$$

$$K'(u,t) = t^{\left(\frac{E_0}{T}-1\right)} e^{\gamma(t)u} (-\ln t)^{1/2}$$

$$\gamma(t) = \sqrt{\frac{-4E_0 E_{ram}\ln t}{T^2}}$$

15.4   Solution Technique for Other Orientations

If the normal to the disk is not parallel to the velocity, the problem is solved similarly, although the geometry is more complex.

First, the disk and the field point are projected onto a plane normal to the velocity (Z), so that the disk edge is an ellipse with its major axis in the X direction.

$$x^2 + \alpha y^2 = R^2 \tag{38}$$

The point (x, y) on the ellipse nearest the field point projection (x_0, y_0) (for the first quadrant) satisfies

$$x(\alpha-1) - \alpha x_0 + xy_0\sqrt{\frac{\alpha}{R^2 - x^2}} = 0 \tag{39}$$

101

When (x_0, y_0) lies inside the ellipse, the outer angular integral is over the angle, ϕ, from the field point to the wake edge, given by:

$$\phi = \arctan\left[\frac{y-y_0}{x-x_0}\right] \pm \psi^2 \qquad (40)$$

where the integration variable, ψ, concentrates near the presumed integrand peak at (x, y). There are two values of u_{min} (the cosine of the angle between the direction from the field point to the disk edge and the negative velocity direction) for each ψ, obtained by calculating the disk edge point $(x_0 + d\cos\phi, y_0 + d\sin\phi, z_1)$. The values are determined by first solving the ellipse equation d, then the circle equation for z_1. Then,

$$u_{min} = \frac{z_0 - z_1}{\sqrt{d^2 + (z_0 - z_1)^2}}, \qquad (41)$$

where the sign of z_1 is opposite the sign of $y_0 + d\sin\phi$. The energy integral then proceeds as for the velocity-aligned case, except that the normalization must take account of the asymmetry in the ϕ integral.

When (x_0, y_0) lies outside the ellipse, the integral is over the region from which ions are excluded and the normalized result subtracted from unity. The outer angular integral is over the variable u (the cosine of the angle between the ram direction and the direction from the field point to a point on the disk), which goes from the angle corresponding to the near point of the disk to the diametrically opposite point. For each u, there are two values of ϕ that satisfy both the disk edge equation and the defining equation for u:

$$(x_0 + d\cos\phi)^2 + \alpha(y_0 + d\sin\phi)^2 = R^2$$
$$(x_0 + d\cos\phi)^2 + (y_0 + d\sin\phi)^2 + z^2 = R^2$$
$$z(y_0 + d\sin\phi) \leq 0 \qquad (42)$$
$$u = \frac{z - z_0}{\sqrt{d^2 + (z - z_0)^2}}$$

The difference between the two ϕ values corresponds to the $\Delta\phi(u)$ that appears in the velocity-aligned case.

15.5   Current Densities

The differential ram ion current density to a detector in the presence of a disk is zero if the detector is looking at the disk. Otherwise, it is given by the following formula:

$$j(E,\Omega) = \frac{e \, n}{\pi} \frac{E}{\theta^2} \sqrt{\frac{e \, \theta}{2 \, \pi \, m}} \exp\left(-\frac{m}{2 \, e \, \theta}(v_i + v_s)^2\right). \qquad (43)$$

The quantity v_i is the velocity of the incident ions (ions at energy E incident in the look direction). The quantity v_s is the velocity of the detector and the disk (negative the ram velocity).

103

LIST OF REFERENCES

1. G. B. Hillard, "Plasma Chamber Testing of APSA coupons for the SAMPIE Flight Experiment", AIAA Paper, AIAA-93-0568.

2. G. A. Bird, "The Free-Molecule Flow Field of a Moving Body in the Upper Atmosphere" in *Rarefied Gas Dynamics*, Ed. L. Talbot, by Academic Press Inc., page 245, 1961.

3. D. A. Hardy, M. R. Oberhardt, W. J. Burke, D. D. Thomson, J. W. Raitt, and L. C. Gentile, "Observations of Electron Beam Propagation Perpendicular to the Earth's Magnetic Field during the TSS 1 Mission", JGR, accepted for publication.